Title:

Unearthing Neandertal population history using nuclear and mitochondrial DNA from cave sediments

One Sentence Summary:

Genome-wide analysis of human DNA from sediments reveals episodes of population replacements and expansions in Neandertal history.

Authors:

Benjamin Vernot[1], Elena I. Zavala[1], Asier Gómez-Olivencia[11][12][8], Zenobia Jacobs[6][7], Viviane Slon[1,16,17], Fabrizio Mafessoni[1], Frédéric Romagné[1], Alice Pearson[1], Martin Petr[1], Nohemi Sala[13][8], Adrián Pablos[13][8], Arantza Aranburu[11][12] , José María Bermúdez de Castro[13], Eudald Carbonell[14][15], Bo Li[6][7], Maciej T. Krajcarz[2], Andrey I. Krivoshapkin[3][4], Kseniya A. Kolobova[3], Maxim B. Kozlikin[3], Michael V. Shunkov[3], Anatoly P. Derevianko[3], Bence Viola[10], Steffi Grote[1], Elena Essel[1], David López Herráez[1], Sarah Nagel[1], Birgit Nickel[1], Julia Richter[1], Anna Schmidt[1], Benjamin Peter[1], Janet Kelso[1], Richard G. Roberts[6][7], Juan-Luis Arsuaga[8][9], Matthias Meyer[1]

Affiliations:

1 - Department of Evolutionary Genetics, Max-Planck-Institute for Evolutionary Anthropology, Leipzig, Germany
2 - Institute of Geological Sciences, Polish Academy of Sciences, Warszawa, Poland
3 - Institute of Archaeology and Ethnography, Russian Academy of Sciences, Novosibirsk, Russia
4 - Novosibirsk State University, Novosibirsk, Russia
5 - Altai State University, Barnaul, Russia
6 - Centre for Archaeological Science, School of Earth, Atmospheric and Life Sciences, University of Wollongong, Australia
7 - Australian Research Council (ARC) Centre of Excellence for Australian Biodiversity and Heritage, University of Wollongong, Australia
8 - Centro Mixto UCM-ISCIII de Evolución y Comportamiento Humanos, Madrid, Spain
9 - Departamento de Paleontología, Facultad Ciencias Geológicas, Universidad Complutense de Madrid, Spain
10 - Department of Anthropology, University of Toronto, Canada

11 - Departamento de Geología, Facultad de Ciencia y Tecnología, Universidad del País Vasco-Euskal Herriko Unibertsitatea (UPV/EHU). Barrio Sarriena s/n, 48940 Leioa, Spain
12 - Sociedad de Ciencias Aranzadi, Zorroagagaina 11, 20014 Donostia-San Sebastián, Spain
13 - Centro Nacional de Investigación sobre la Evolución Humana (CENIEH), Paseo de la Sierra de Atapuerca, 3, 09002 Burgos, Spain
14 - Institut Català de Paleoecologia Humana i Evolució Social (IPHES), Zona Educacional 4, Campus Sescelades, Edifici W3, Universitat Rovira i Virgili, Tarragona, Spain
15 - Àrea de Prehistòria, Universitat Rovira i Virgili, Avinguda de Catalunya 35, 43002, Tarragona, Spain
16 - Department of Anatomy and Anthropology and Department of Human Molecular Genetics and Biochemistry, Sackler Faculty of Medicine, Tel Aviv University, 6997801 Tel Aviv, Israel
17 - The Dan David Center for Human Evolution and Biohistory Research, Tel Aviv University, 6997801 Tel Aviv, Israel

Abstract:

Bones and teeth are important sources of Pleistocene hominin DNA, but are rarely recovered at archaeological sites. Mitochondrial DNA has been retrieved from cave sediments, but provides limited value for studying population relationships. We therefore developed methods for the enrichment and analysis of nuclear DNA from sediments, and applied them to cave deposits in western Europe and southern Siberia dated to between approximately 200,000 and 50,000 years ago. We detect a population replacement in northern Spain approximately 100,000 years ago, accompanied by a turnover of mitochondrial DNA. We also identify two radiation events in Neandertal history during the early part of the Late Pleistocene. Our work lays the ground for studying the population history of ancient hominins from trace amounts of nuclear DNA in sediments.

Main text:

Introduction

The analysis of ancient DNA from Pleistocene hominins has greatly enhanced our understanding of the evolutionary history of archaic humans, and their interactions with early modern humans. To date, complete or partial nuclear genome sequences have been recovered from the skeletal

remains of 23 archaic hominin individuals: 18 Neandertals from 14 sites across Eurasia (mostly in Europe), four Denisovans, and the offspring of a Neandertal mother and a Denisovan father (*Denisova 11*) (*1*) recovered from Denisova Cave in the Altai Mountains of southern Siberia. Although numerous Paleolithic sites have been excavated, relatively few have yielded skeletal remains of hominins, which are often concentrated in one or a few strata. Attempts to reconstruct the genetic history of archaic hominins are therefore constrained by an uneven temporal and spatial sampling, limited largely by the availability of specimens.

In 2017, it was found that hominin mitochondrial DNA (mtDNA) can be recovered from Pleistocene sediments (*2*), indicating that it may be possible to overcome the dependency on the scarce fossil record in the quest for hominin DNA. However, mtDNA only carries information about the maternal lineage and does not always reflect the complete population history (e.g., (*3*)). Nuclear DNA contains far more information, but its retrieval from sediments presents substantial challenges: it is present in fewer copies than mtDNA, and many loci are not informative for population genetic analyses. Additionally, the vast majority of mammalian DNA in sediments is non-hominin, which may be difficult to distinguish from hominin DNA due to sequence homology at many loci. These characteristics, as well as the dominance of microbial DNA (*2*), hamper attempts to retrieve nuclear sequences in sufficient number and quality for population genetic analyses by simple shotgun sequencing. To overcome these challenges, we set out to retrieve hominin nuclear genomic sequences from sediments by targeting, via hybridization capture, regions in the nuclear genome with high mammalian sequence diversity, and used these sequences to explore the history of Neandertal populations in western Europe and southern Siberia.

Archaeological sites

We focused our analyses on sediments from three Paleolithic sites. Denisova Cave (*4*) and Chagyrskaya Cave (*5*), both located in the Altai Mountains (Fig. 1A), were included for their known mtDNA preservation in sediment (*2*), and to enable comparisons to three high-coverage nuclear genomes generated previously for bones from these sites: *Denisova 5* (the *Altai Neandertal* toe bone, dated to 90.9–130.0 thousand years (ka)) (*6*, *7*), *Denisova 3* (a Denisovan finger bone, 51.6–76.2 ka) (*6*, *8*) and *Chagyrskaya 8* (a Neandertal finger bone, 49.0–92 ka) (*5*,

9). All age ranges include the 95% confidence interval (CI) of the dating method(s). Whereas Denisova Cave has evidence for at least 250 millennia of archaic human occupation (*4*), the Neandertal-bearing deposits at Chagyrskaya Cave (Layers 5 and 6; Figs. 1B, S1) accumulated in less than 10 millennia (*5*).

The third site, Galería de las Estatuas ('Estatuas'), is part of the Atapuerca archaeo-paleontological complex in northern Spain (Figs. 1C, S2). Almost 500 stone artifacts with clear Mousterian affinities, combined with single-grain optical dating of the associated sediments, indicate Neandertal occupation from at least 113 ± 8 to 70 ± 5 ka ago (total uncertainty at 1σ; (*10*, *11*)), yet only a single Neandertal foot phalanx has been recovered (*12*) (Fig. S3). Initial screening of the Estatuas sediments indicated the presence of ancient mammalian mtDNA, including that of hominins ((*13*), Figs. S4-6, Tables S10-11). Analysis of sediment DNA may therefore be the only viable approach for reconstructing the population genetics of the occupants of this site during a time period not currently well represented in the genetic record of European Neandertals.

For Denisova Cave, we retrieved nuclear DNA from three existing sediment samples with hominin mtDNA preservation, from Layers 11.4 and 15 in East Chamber and Layer 14.3 in Main Chamber (*2*, *4*). At Chagyrskaya Cave and Estatuas, we extensively sampled across the Paleolithic layers, collecting 76 samples from two pits at Estatuas and 73 samples from Chagyrskaya Cave (Figs. 1B, 1C, S4-5 ; (*13*)), and targeted both mitochondrial and nuclear hominin DNA.

Retrieval of hominin mtDNA

We enriched hominin mtDNA from Chagyrskaya Cave and Estatuas samples using protocols for automated DNA extraction (*14*), library preparation (*15*) and hybridization capture (*2*). To maximize the number of libraries containing sufficient amounts of hominin DNA for analysis, multiple subsamples were taken from some of the Estatuas samples, and several libraries produced from some subsamples, for a total of 369 libraries. After assigning sequences to mammalian families using MEGAN (*16*) we found that 74% of samples (n=54) from Chagyrskaya and 56% (n=43) from Estatuas yielded at least one library containing hominin mtDNA fragments with significantly elevated frequencies of cytosine (C) to thymine (T) substitutions at their 5' and 3' ends, compatible with the presence of deaminated ancient DNA

(Table S10, (*13*)). Of the 223 libraries containing ancient hominin mtDNA, 182 (82%) yielded sufficient fragments to allow their assignment to a hominin group based on 'diagnostic' positions in the mtDNA genome that are derived in one hominin group (modern humans, Neandertals, Denisovans or the Sima de los Huesos hominins) and ancestral in the others (*3*, *13*). All such assignments were to Neandertal mtDNA, consistent with archaeological evidence for the presence of Neandertals in all layers – with exception of the upper portions of Layer 7 in Chagyrskaya Cave, which is archaeologically sterile and dated to >300 ka. The detection of Neandertal mtDNA near the top of Layer 7 may be due to it being a former living floor and/or a consequence of post-depositional mixing with sediments from the overlying Subunit 6c, resulting in Subunit 6d (*5*, *13*).

Fourteen samples produced libraries with high coverage of the Neandertal mtDNA genome (>17-fold) and point estimates of present-day human contamination lower than 10% (*13*). Four of these (from Chagyrskaya Subunit 6c, Estatuas pit II/Layer 2, and Estatuas pit I/Layers 3 and 4) appeared to contain a single mitochondrial sequence on the basis of the consistency of nucleotides observed at each position ((*13*), Fig. S7, Table S3). These were used for generating near-complete consensus sequences and building a phylogenetic tree with BEAST2 (*17*), along with previously published hominin mtDNA sequences derived from skeletal remains or from present-day humans, and a sequence reconstructed from the Layer 14.3 sediment sample from Main Chamber in Denisova Cave (*2*) (Figs. 2A, S8; Table S4; (*13*)).

Most strikingly, we find that the consensus mtDNA genome from Estatuas pit I/Layer 4 is most similar to the mtDNA of the ~120 ka Neandertal from Hohlenstein-Stadel (*HST*), Germany, which falls basal to all other known Neandertal mitochondrial genomes (*18*, *19*). The Estatuas pit I/Layer 4 sediments (dated to 112 ± 7 ka) are broadly contemporaneous with *HST*. The mtDNA genomes from Estatuas pit II/Layer 2 (79 ± 5 ka) and pit I/Layer 3 (107 ± 8 ka) group with mtDNA from the 60–70 ka *Mezmaiskaya 1* individual from the northern Caucasus (*7*, *20*), whereas the sequence for Chagyrskaya Subunit 6c groups with the mtDNA from *Chagyrskaya 8* (*9*). We note that ages estimated from the branch lengths of the sediment mtDNA sequences in the tree, such as 136 ka (95% CI: 75–200 ka) for the Estatuas pit I/Layer 4 sample, match previously published ages for the respective sites and layers ((*13*); Table S5).

To further investigate mitochondrial diversity in the sediments from Chagyrskaya Cave and Estatuas, we developed a method to probabilistically place libraries with as few as 250

ancient fragments in the known Neandertal mtDNA diversity ((*13*); Figs S9-12). This method allowed phylogenetic assignments of mtDNA from 38 libraries from Chagyrskaya Cave and 59 from Estatuas, spanning most layers sampled in each cave (Fig. 2B). We find that Estatuas pit I/Layers 4 and 5 contain both *HST*-like and non-*HST*-like Neandertal mtDNA, often in the same subsample, with the latter largely grouping with *Mezmaiskaya 1* and *Scladina I-4a*, a ~130 ka Neandertal from western Europe (*19*, *21*). *HST*-like mtDNA then disappears from the upper layers of Estatuas, leaving mtDNA predominantly related to the *Mezmaiskaya 1*-like consensus sequences from those layers (Fig. 2B). Simulated mixing of DNA from the upper layers and pit I/Layer 4 does not generate the observation of *Mezmaiskaya 1* and *Scladina I-4a* -like DNA in pit I/Layer 4, indicating true heterogeneity of mtDNA in the lower layers, consistent with the previously observed integrity of the Estatuas stratigraphy (*11*, *13*). In Chagyrskaya Cave we, find remarkable homogeneity: all samples from Layers 5 to 7 grouping with the Subunit 6c consensus sequence, *Chagyrskaya 8* or *Okladnikov 2* (also from the Altai region) (*22*, *23*), with occasional support for *Denisova 11*-like sequences.

Nuclear DNA enrichment method

To extend the study of hominin DNA from sediments to the nuclear genome, we designed a probe-set targeting 1.6 million informative single nucleotide polymorphisms (SNPs) in the nuclear genome, and enriched for DNA fragments overlapping these sites via hybridization capture (*2*, *13*). We employed several techniques to both reduce and measure the extent of mis-mapping of non-hominin faunal DNA, and evaluated these measures using simulated ancient brown bear (*Ursus arctos*) DNA, with fragment sizes and deamination profiles taken from an ancient DNA library (*13*). We found that faunal mis-alignment is drastically reduced in regions of high mammalian diversity (e.g., Figs. 3A versus 3B), by at least 48-fold where the human genome differs by 8 or more base pairs from at least one non-primate genome (in a 52 bp region centered on a target SNP; Fig. 3C). We therefore restricted our design to SNPs in these regions. We additionally assign each DNA fragment to the NCBI taxonomy using the metagenomics software Kraken (*24*), and restricted our analyses to fragments classified as primate (*13*). This metagenomic filtering step dramatically enriches for hominin DNA, reducing the alignment of simulated ancient bear DNA to the human reference genome by a factor of 140, versus 1.8-fold for Neandertal DNA (*13*). However, these approaches may not eliminate all faunal mis-

alignment, particularly if the DNA originates from a species that is not well represented in the NCBI taxonomy. Therefore, we included in our probe design 98,887 'hominin diagnostic' sites, which are fixed-derived in hominins, chimpanzees and bonobos (Fig. 3D). At these sites, ancestral alleles in the captured fragments are strongly indicative of the presence of non-hominin mammalian DNA (0.2% ancestral in Neandertal compared to 95.6% in *U. arctos* DNA; Fig. 3E, (*13*)), and can be used to estimate faunal mis-alignment proportions.

Nuclear DNA recovery and sexing

We first applied these methods to previously prepared libraries from three Denisova Cave sediments: two with Neandertal and one with Denisovan mtDNA (*2*). All showed significant levels of C-to-T substitutions in DNA fragments overlapping our targeted SNPs, consistent with the presence of ancient nuclear DNA ((*13*); Fig. S14; Table S13). One sample showed evidence of moderate (~15%) non-hominin faunal mis-alignment before metagenomic filtering, but filtering reduced this to <1% (Table S13). After filtering, 1764, 27,923 and 162,508 DNA fragments (459, 8698 and 42,103 with evidence of deamination) were retained from the three samples, representing up to ~0.1x coverage of our targeted sites.

Having confirmed the presence of ancient hominin nuclear DNA, we next asked whether we could assign each sample to a hominin group. By examining deaminated DNA fragments at sites where the high-coverage Denisovan and *Altai Neandertal* genomes are homozygous and differ from each other, we find that in the two samples containing Neandertal mtDNA, approximately 90% of DNA fragments carry the Neandertal derived state, versus 2% carrying the Denisovan derived state (Fig. 4A, top left, red points). In contrast, the nuclear DNA in the sample containing Denisovan mtDNA carries the Denisovan derived allele in 65% of cases, but no Neandertal derived alleles (Fig. 4A, top left, blue point). These results are consistent with those obtained from low-coverage Neandertal and Denisovan genomes from skeletal remains ((*1*, *13*, *19*, *25–27*); Fig. 4A, bottom right, red and blue points), suggesting that the nuclear DNA in the three sediment samples is either of Neandertal or Denisovan origin, but not both.

We next captured nuclear DNA from Chagyrskaya Cave and Estatuas sediment samples: 29 samples yielded at least one library with significant evidence for deamination and <5% faunal mis-alignment ((*13*); Tables S12-13); four libraries showed evidence for >5% faunal mis-alignment and were excluded from further analyses, highlighting the importance of per-library

mis-alignment estimates ((*13*); Table S14). In total, we retrieved nuclear DNA from Chagyrskaya Cave Subunits 6a–d and 7 (the latter likely intrusive from Subunits 6c and 6d; (*13*)), and Estatuas pit II/Layer 2 and pit I/Layers 2–5. Recovery of hominin DNA was lower than for the Denisova Cave samples, with our best libraries yielding 134,497 fragments (33,594 with evidence of deamination) at target sites for Chagyrskaya Cave and 47,667 for Estatuas (16,678 deaminated). In a plot of Neandertal versus Denisovan alleles, these samples clearly contain Neandertal nuclear DNA, and cluster together closely with Neandertal skeletal samples (Fig. 4A, top right and bottom left). Equivalent plots considering sites that differ among the *Altai Neandertal*, *Vindija 33.19* or *Chagyrskaya 8* genomes lack the resolution to resolve their relationship to these Neandertal genomes, given the small amounts of data per sample at these SNPs (Figs. S15-16, (*13*)).

For skeletal specimens, the relative proportions of X and autosomal DNA have been used to determine sex (*3*). We applied this approach to sediment subsamples with <10% present-day human contamination and deaminated DNA fragments covering at least 5,000 sites, and find that all such Denisova Cave and Estatuas samples show X/autosome proportions consistent with hominin DNA originating primarily from a single sex (three male and three female; Figs. 4B, S17). In contrast, the majority of samples from Chagyrskaya Cave fall between the expected male and female proportions, suggesting that they contain DNA from multiple individuals of different sexes (Fig. 4B). All four libraries for which we identified a single mtDNA sequence have X/autosome proportions consistent with the DNA originating from a single sex, suggesting that they may contain DNA from individual Neandertals (Fig. 4B, black-labeled sediment points), although we cannot exclude the presence of identical mtDNA from multiple individuals of the same sex.

Nuclear phylogenetic analysis

To place each sample on the larger archaic phylogeny despite limited data, we developed a maximum likelihood framework which, for a sample *X*, co-estimates the point at which *X* branched from the archaic hominin tree — defined by the three Neandertal and one Denisovan high-coverage genomes (e.g., Neandertal phylogeny in Fig. 4C) — along with the proportion of fragments deriving from non-hominin faunal mis-alignment and present-day human contamination. This method makes use of the fact that all sites which are polymorphic in archaic

hominins are informative for their population histories. For example, at a site which is heterozygous in one archaic genome but homozygous ancestral in the others, the probability of observing a derived allele in a sample *X* [p(*X* = der)] varies based on the point at which *X* diverged from the overall tree (Fig. 4C, black points and bar plot). These probabilities are obtained from coalescent simulations for which effective population sizes and split times are inferred from the respective high-coverage genomes (*13*). Mis-alignment and contamination proportions are estimated independently for deaminated and non-deaminated fragments, allowing all fragments to be used in the analysis (*13*). Although some sediment samples may represent single individuals, this method operates on allele frequency expectations, making it equally applicable to samples representing single or multiple individuals from a population. When applied to previously published low-coverage genomes from skeletal samples, our method infers population split times and contamination proportions consistent with previous estimates (*13*). In a power analysis, we estimate accurate population split times in down-sampled low-coverage Neandertal genomes (*25*) with up to 70% present-day human contamination (mean absolute error 10–16 ka with 500 Neandertal DNA fragments; 4–7 ka with 4000 fragments; Figs. S18-22; (*13*)), and accurately infer present-day human contamination proportions of up to 90% (Fig. S20; (*13*)).

Applying this method to sediment libraries from Denisova and Chagyrskaya Caves, we find results consistent with previously published ancient DNA from skeletal elements. Specifically, we find that the two Neandertal samples from Denisova Cave fall on the lineage leading to the *Altai Neandertal* individual (Fig. 4D, De-E11.4 and De-M14.3, Table S14). This result is consistent with the first of these samples originating from the same layer in East Chamber (Layer 11.4) as the *Altai Neandertal*, and the second sample from a contemporaneous layer (Layer 14.3) in Main Chamber (deposited approximately 105–120 and 97–112 ka ago, respectively) (*4*). The Denisovan sample from Layer 15 in East Chamber (dated to ~200 ka) (*4*) falls on the Denisovan lineage, consistent with its mtDNA ((*2*); Fig. S23). The sediment samples from all layers at Chagyrskaya Cave fall on the *Chagyrskaya 8* lineage (Fig. 4D, Ch-3058a and Ch-3007a; Fig. S24), consistent with a short-lived occupation of the site by Neandertals associated with a distinctive Middle Paleolithic toolkit (*5*).

For Estatuas, where less nuclear DNA was recovered from the sediment samples and no previous genetic data exist from skeletal remains, we estimated population split times for individual subsamples with at least 500 Neandertal DNA fragments and less than 70% present-

day human contamination. We also merged samples to obtain per-layer estimates, with 5000–36,000 fragments per layer (Fig. 5A). Samples from pit II/Layer 2, pit I/Layer 2 and pit I/Layer 3 (*10*) diverge from the Neandertal tree approximately 100–115 ka (Fig. 5A; block bootstrap 95% CIs: 102–114, 99–122 and 102–112 ka, respectively), similar to the split times of *Vindija 33.19*, *Chagyrskaya 8* and *Mezmaiskaya 1* from each other (~104 ka; Fig. 5B,C). The time of deposition of pit I/Layer 3 (107 ± 8 ka; (*10*, *13*)) is indistinguishable form this date of divergence, suggesting that the Neandertals from pit I/Layer 3 were closely related to the ancestors of *Vindija 33.19* and *Chagyrskaya 8*. We are unable to determine whether the aforementioned layers represent a repeated occupation of the cave by the same Neandertal population, but the split times and the mtDNA data (Fig. 2B) are consistent with this hypothesis.

In contrast, sediments from pit I/Layer 4 carrying the *HST*-like mtDNA diverge from the Neandertal tree approximately 122–135 ka ago (Fig. 5A, block bootstrap 95% CI). This divergence time is similar to that of the *HST* Neandertal itself, as well as of the *Scladina* and *Altai* Neandertals (Fig. 5B, C). The latter two carry the more common non-*HST*-like Neandertal mtDNA type (Fig. 5B), consistent with mitochondrial diversity in the ancestral Neandertal population, which is also observed in pit I/Layer 4 (Fig. 2B). GE-I-B33f, the only sample of the common Neandertal mtDNA type from pit I/Layer 4 that yielded nuclear DNA, was collected from near the boundary with Layer 3 and produced a divergence time similar to those of the Layer 3 samples, albeit with a large CI (83–139 ka) due to the small data set (867 ancient hominin DNA fragments). Taken together, these observations suggest that a population replacement occurred at Estatuas towards the end of the time of deposition of Layer 4, which was accompanied by a loss of mtDNA diversity. Similar results were obtained when using only deaminated fragments (Fig. S25), highlighting the robustness of the method to the effects of present-day human contamination.

Discussion

The apparent clustering of branching times suggests two distinct radiations of Neandertal populations: *Mezmaiskaya 1*, *Vindija 33.19*, *Chagyrskaya 8* and Estatuas pit II/Layer 2 and pit I/Layers 2 and 3 diverged from each other approximately 100–115 ka, whereas the *Altai*, *HST*, *Scladina* and Estatuas pit I/Layer 4 Neandertals, and the lineage leading to *Vindija 33.19* and

Chagyrskaya 8, diverged from each other ~135 ka ago (Fig. 5C). These radiation events therefore occurred during the early part of the Late Pleistocene and may be associated with changes in climate and environmental conditions during the last interglacial. In addition, it has been noted that the typical Neandertal morphology evolved in several stages (*28*, *29*), with the last stage, the "classic" Neandertals, appearing around 100,000 years ago. Despite the uncertainty in dating these events, it seems plausible that the latter transition could be linked to the younger population radiation we detected. However, to detect if such factors played a key role in the population dynamics of Neandertals and other Pleistocene hominins (*30*, *31*) would require time-series data from additional sites and more precise estimates of the timing of these genetic events of interest. The methods presented here open the possibility to obtain such data independently of the fossil record, limited only by biochemical constraints on long-term DNA preservation.

Our results also show that the recovery of hominin DNA from sediment may not be limited to population samples, as DNA that putatively derived from individual Neandertals (i.e., sediment samples with a single mtDNA sequence and sex) was identified in sediment samples from all three study sites. This observation suggests that it may be possible, in the future, to also assess heterogeneity in the genetic composition of past populations based on the analysis of sediment DNA. In light of the substantial variation in the quantity of hominin DNA observed among sediment samples taken in close proximity (and within single samples), and considering the low abundance of hominin DNA compared to non-hominin faunal DNA, it seems unlikely that the analysis of hominin DNA from Pleistocene sediments is significantly impacted—if at all—by leaching of DNA through archaeological layers. However, the presence of Neandertal DNA in Layer 7 of Chagyrskaya Cave highlights the need to evaluate evidence for post-depositional mixing of sediments when assigning DNA sequences from sediment to specific layers, as is common practice when interpreting finds of artifacts, skeletal remains and other archaeological materials. Finally, our work also highlights the value of high-coverage archaic human genomes, even if generated only in small numbers, as scaffolding for defining the past genetic landscape on to which less complete genome-wide sequence data from sediments and bones can be mapped.

Materials and Methods

Sediment samples were taken from the exposed sections of Chagyrskaya Cave and Galería de las Estatuas, and sub-samples with a weight between 21 and 128 mg used for DNA extraction (*14*) and single-stranded DNA library preparation (*15*). All libraries were enriched for hominin mtDNA using hybridization capture (*32*), and a sub-set for mammalian mtDNA (*33*) to evaluate the preservation of ancient faunal DNA. Based on the content of ancient hominin mtDNA, and aiming to recover hominin nuclear DNA from all relevant layers, libraries from this study and a previous study on DNA preservation in the sediments of Denisova Cave (*2*) were selected for hybridization capture using probes targeting phylogenetically informative positions in the nuclear genome. Mitochondrial sequences were identified on the biological family level using a previously established analysis pipeline (*2*), which includes an evaluation of the presence of deamination patterns typical for ancient DNA and assignments of the Hominidae component to specific hominid groups. Further assignments to specific branches of the hominin mtDNA tree were performed using a method based on the software kallisto (*13*, *34*). Hominin nuclear DNA sequences were identified and phylogenetic analyses performed as summarized in Fig. S26 and described in full detail in (*13*), together with details on sample collection, sample preparation, data processing and the computational and phylogenetic analyses performed (*13*). Software and scripts written were in Python (*35*) and R (*36*), and plots were created with ggplot2 (*37*), cowplot (*38*), RColorBrewer (*39*) and ggmap (*40*), and are publicly available as described in (*13*).

361

References and Notes

1. V. Slon, F. Mafessoni, B. Vernot, C. de Filippo, S. Grote, B. Viola, M. Hajdinjak, S. Peyrégne, S. Nagel, S. Brown, K. Douka, T. Higham, M. B. Kozlikin, M. V. Shunkov, A. P. Derevianko, J. Kelso, M. Meyer, K. Prüfer, S. Pääbo, The genome of the offspring of a Neanderthal mother and a Denisovan father. *Nature*, 1 (2018).

2. V. Slon, C. Hopfe, C. L. Weiß, F. Mafessoni, M. de la Rasilla, C. Lalueza-Fox, A. Rosas, M. Soressi, M. V. Knul, R. Miller, J. R. Stewart, A. P. Derevianko, Z. Jacobs, B. Li, R. G. Roberts, M. V. Shunkov, H. de Lumley, C. Perrenoud, I. Gušić, Ž. Kućan, P. Rudan, A. Aximu-Petri, E. Essel, S. Nagel, B. Nickel, A. Schmidt, K. Prüfer, J. Kelso, H. A. Burbano, S. Pääbo, M. Meyer, Neandertal and Denisovan DNA from Pleistocene sediments. *Science*, eaam9695 (2017).

3. M. Meyer, J.-L. Arsuaga, C. de Filippo, S. Nagel, A. Aximu-Petri, B. Nickel, I. Martínez, A. Gracia, J. M. Bermúdez de Castro, E. Carbonell, B. Viola, J. Kelso, K. Prüfer, S. Pääbo, Nuclear DNA sequences from the Middle Pleistocene Sima de los Huesos hominins. *Nature*. **531**, 504–507 (2016).

4. Z. Jacobs, B. Li, M. V. Shunkov, M. B. Kozlikin, N. S. Bolikhovskaya, A. K. Agadjanian, V. A. Uliyanov, S. K. Vasiliev, K. O'Gorman, A. P. Derevianko, R. G. Roberts, Timing of archaic hominin occupation of Denisova Cave in southern Siberia. *Nature*. **565**, 594–599 (2019).

5. K. A. Kolobova, R. G. Roberts, V. P. Chabai, Z. Jacobs, M. T. Krajcarz, A. V. Shalagina, A. I. Krivoshapkin, B. Li, T. Uthmeier, S. V. Markin, M. W. Morley, K. O'Gorman, N. A. Rudaya, S. Talamo, B. Viola, A. P. Derevianko, Archaeological evidence for two separate dispersals of Neanderthals into southern Siberia. *Proc. Natl. Acad. Sci.* **117**, 2879–2885 (2020).

6. K. Douka, V. Slon, Z. Jacobs, C. B. Ramsey, M. V. Shunkov, A. P. Derevianko, F. Mafessoni, M. B. Kozlikin, B. Li, R. Grün, D. Comeskey, T. Devièse, S. Brown, B. Viola, L. Kinsley, M. Buckley, M. Meyer, R. G. Roberts, S. Pääbo, J. Kelso, T. Higham, Age estimates for hominin fossils and the onset of the Upper Palaeolithic at Denisova Cave. *Nature*. **565**, 640–644 (2019).

7. K. Prüfer, F. Racimo, N. Patterson, F. Jay, S. Sankararaman, S. Sawyer, A. Heinze, G. Renaud, P. H. Sudmant, C. de Filippo, H. Li, S. Mallick, M. Dannemann, Q. Fu, M. Kircher, M. Kuhlwilm, M. Lachmann, M. Meyer, M. Ongyerth, M. Siebauer, C. Theunert, A. Tandon, P. Moorjani, J. Pickrell, J. C. Mullikin, S. H. Vohr, R. E. Green, I. Hellmann, P. L. F. Johnson, H. Blanche, H. Cann, J. O. Kitzman, J. Shendure, E. E. Eichler, E. S. Lein, T. E. Bakken, L. V. Golovanova, V. B. Doronichev, M. V. Shunkov, A. P. Derevianko, B. Viola, M. Slatkin, D. Reich, J. Kelso, S. Pääbo, The complete genome sequence of a Neanderthal from the Altai Mountains. *Nature*. **505**, 43–49 (2014).

8. M. Meyer, M. Kircher, M.-T. Gansauge, H. Li, F. Racimo, S. Mallick, J. G. Schraiber, F. Jay, K. Prüfer, C. de Filippo, P. H. Sudmant, C. Alkan, Q. Fu, R. Do, N. Rohland, A. Tandon, M. Siebauer, R. E. Green, K. Bryc, A. W. Briggs, U. Stenzel, J. Dabney, J. Shendure, J. Kitzman, M. F. Hammer, M. V. Shunkov, A. P. Derevianko, N. Patterson, A. M. Andrés, E. E. Eichler, M. Slatkin, D. Reich, J. Kelso, S. Pääbo, A High-Coverage Genome Sequence from an Archaic Denisovan Individual. *Science*. **338**, 222–226 (2012).

9. F. Mafessoni, S. Grote, C. de Filippo, V. Slon, K. A. Kolobova, B. Viola, S. V. Markin, M. Chintalapati, S. Peyrégne, L. Skov, P. Skoglund, A. I. Krivoshapkin, A. P. Derevianko, M. Meyer, J. Kelso, B. Peter, K. Prüfer, S. Pääbo, A high-coverage Neandertal genome from Chagyrskaya Cave. *Proc. Natl. Acad. Sci.* **117**, 15132–15136 (2020).

10. M. Demuro, L. J. Arnold, A. Aranburu, A. Gómez-Olivencia, J.-L. Arsuaga, Single-grain OSL dating of the Middle Palaeolithic site of Galería de las Estatuas, Atapuerca (Burgos, Spain). *Quat. Geochronol.* **49**, 254–261 (2019).

11. J. L. Arsuaga, A. Gómez-Olivencia, N. Sala, V. Martínez-Pillado, A. Pablos, A. Bonmatí, A. Pantoja-Pérez, J. Lira-Garrido, A. Alcázar de Velasco, A. I. Ortega, G. Cuenca-Bescós, N. García, A. Aranburu, B. Ruiz-Zapata, M. J. Gil-García, X. P. Rodríguez-Álvarez, A. Ollé, M. Mosquera, Evidence of paleoecological changes and Mousterian occupations at the Galería de las Estatuas site, Sierra de Atapuerca, northern Iberian plateau, Spain. *Quat. Res.* **88**, 345–367 (2017).

12. A. Pablos, A. Gómez-Olivencia, J. L. Arsuaga, A Neandertal foot phalanx from the Galería de las Estatuas site (Sierra de Atapuerca, Spain). *Am. J. Phys. Anthropol.* **168**, 222–228 (2019).

13. Materials and methods are available as supplementary materials.

14. N. Rohland, I. Glocke, A. Aximu-Petri, M. Meyer, Extraction of highly degraded DNA from ancient bones, teeth and sediments for high-throughput sequencing. *Nat. Protoc.* **13**, 2447–2461 (2018).

15. M.-T. Gansauge, A. Aximu-Petri, S. Nagel, M. Meyer, Manual and automated preparation of single-stranded DNA libraries for the sequencing of DNA from ancient biological remains and other sources of highly degraded DNA. *Nat. Protoc.* **15**, 2279–2300 (2020).

16. D. H. Huson, S. Beier, I. Flade, A. Górska, M. El-Hadidi, S. Mitra, H.-J. Ruscheweyh, R. Tappu, MEGAN Community Edition - Interactive Exploration and Analysis of Large-Scale Microbiome Sequencing Data. *PLOS Comput. Biol.* **12**, e1004957 (2016).

17. R. Bouckaert, J. Heled, D. Kühnert, T. Vaughan, C.-H. Wu, D. Xie, M. A. Suchard, A. Rambaut, A. J. Drummond, BEAST 2: A Software Platform for Bayesian Evolutionary Analysis. *PLOS Comput. Biol.* **10**, e1003537 (2014).

18. C. Posth, C. Wißing, K. Kitagawa, L. Pagani, L. van Holstein, F. Racimo, K. Wehrberger, N. J. Conard, C. J. Kind, H. Bocherens, J. Krause, Deeply divergent archaic mitochondrial genome provides lower time boundary for African gene flow into Neanderthals. *Nat. Commun.* **8**, 1–9 (2017).

19. S. Peyrégne, V. Slon, F. Mafessoni, C. de Filippo, M. Hajdinjak, S. Nagel, B. Nickel, E. Essel, A. L. Cabec, K. Wehrberger, N. J. Conard, C. J. Kind, C. Posth, J. Krause, G. Abrams, D. Bonjean, K. D. Modica, M. Toussaint, J. Kelso, M. Meyer, S. Pääbo, K. Prüfer, Nuclear DNA from two early Neandertals reveals 80,000 years of genetic continuity in Europe. *Sci. Adv.* **5**, eaaw5873 (2019).

20. A. R. Skinner, B. A. B. Blackwell, S. Martin, A. Ortega, J. I. B. Blickstein, L. V. Golovanova, V. B. Doronichev, ESR dating at Mezmaiskaya Cave, Russia. *Appl. Radiat. Isot.* **62**, 219–224 (2005).

21. M. Toussaint, D. Bonjean, *The Scladina I-4A Juvenile Neandertal, Andenne, Belgium: Palaeoanthropology and Context* (Université de Liège, 2014).

22. P. Skoglund, B. H. Northoff, M. V. Shunkov, A. P. Derevianko, S. Pääbo, J. Krause, M. Jakobsson, Separating endogenous ancient DNA from modern day contamination in a Siberian Neandertal. *Proc. Natl. Acad. Sci.* **111**, 2229–2234 (2014).

23. K. A. Kolobova, A. V. Shalagina, V. P. Chabai, S. V. Markin, A. I. Krivoshapkin, The significance of bifacial technologies in Altai Middle Paleolithic. *Anthropol. Fr.* **123**, 276–288 (2019).

24. D. E. Wood, S. L. Salzberg, Kraken: ultrafast metagenomic sequence classification using exact alignments. *Genome Biol.* **15**, R46 (2014).

25. M. Hajdinjak, Q. Fu, A. Hübner, M. Petr, F. Mafessoni, S. Grote, P. Skoglund, V. Narasimham, H. Rougier, I. Crevecoeur, P. Semal, M. Soressi, S. Talamo, J.-J. Hublin, I. Gušić, Ž. Kućan, P. Rudan, L. V. Golovanova, V. B. Doronichev, C. Posth, J. Krause, P. Korlević, S. Nagel, B. Nickel, M. Slatkin, N. Patterson, D. Reich, K. Prüfer, M. Meyer, S. Pääbo, J. Kelso, Reconstructing the genetic history of late Neanderthals. *Nature*. **555**, 652–656 (2018).

26. K. Prüfer, C. de Filippo, S. Grote, F. Mafessoni, P. Korlević, M. Hajdinjak, B. Vernot, L. Skov, P. Hsieh, S. Peyrégne, D. Reher, C. Hopfe, S. Nagel, T. Maricic, Q. Fu, C. Theunert, R. Rogers, P. Skoglund, M. Chintalapati, M. Dannemann, B. J. Nelson, F. M. Key, P. Rudan, Ž. Kućan, I. Gušić, L. V. Golovanova, V. B. Doronichev, N. Patterson, D. Reich, E. E. Eichler, M. Slatkin, M. H. Schierup, A. Andrés, J. Kelso, M. Meyer, S. Pääbo, A high-coverage Neandertal genome from Vindija Cave in Croatia. *Science*, eaao1887 (2017).

27. S. Sawyer, G. Renaud, B. Viola, J.-J. Hublin, M.-T. Gansauge, M. V. Shunkov, A. P. Derevianko, K. Prüfer, J. Kelso, S. Pääbo, Nuclear and mitochondrial DNA sequences from two Denisovan individuals. *Proc. Natl. Acad. Sci.* **112**, 15696–15700 (2015).

28. D. Dean, J.-J. Hublin, R. Holloway, R. Ziegler, On the phylogenetic position of the pre-Neandertal specimen from Reilingen, Germany. *J. Hum. Evol.* **34**, 485–508 (1998).

29. J. L. Arsuaga, I. Martínez, L. J. Arnold, A. Aranburu, A. Gracia-Téllez, W. D. Sharp, R. M. Quam, C. Falguères, A. Pantoja-Pérez, J. Bischoff, E. Poza-Rey, J. M. Parés, J. M. Carretero, M. Demuro, C. Lorenzo, N. Sala, M. Martinón-Torres, N. García, A. Alcázar de Velasco, G. Cuenca-Bescós, A. Gómez-Olivencia, D. Moreno, A. Pablos, C.-C. Shen, L. Rodríguez, A. I. Ortega, R. García, A. Bonmatí, J. M. Bermúdez de Castro, E. Carbonell, Neandertal roots: Cranial and chronological evidence from Sima de los Huesos. *Science*. **344**, 1358–1363 (2014).

30. R. Potts, Evolution and Environmental Change in Early Human Prehistory. *Annu. Rev. Anthropol.* **41**, 151–167 (2012).

31. J.-J. Hublin, in *Neandertals and Modern Humans in Western Asia*, T. Akazawa, K. Aoki, O. Bar-Yosef, Eds. (Springer US, Boston, MA, 1998; https://doi.org/10.1007/0-306-47153-1_18), pp. 295–310.

32. Q. Fu, M. Meyer, X. Gao, U. Stenzel, H. A. Burbano, J. Kelso, S. Pääbo, DNA analysis of an early modern human from Tianyuan Cave, China. *Proc. Natl. Acad. Sci.* **110**, 2223–2227 (2013).

33. V. Slon, I. Glocke, R. Barkai, A. Gopher, I. Hershkovitz, M. Meyer, Mammalian mitochondrial capture, a tool for rapid screening of DNA preservation in faunal and undiagnostic remains, and its application to Middle Pleistocene specimens from Qesem Cave (Israel). *Quat. Int.* **398**, 210–218 (2016).

34. N. L. Bray, H. Pimentel, P. Melsted, L. Pachter, Near-optimal probabilistic RNA-seq quantification. *Nat. Biotechnol.* **34**, 525–527 (2016).

35. G. Van Rossum, F. L. Drake Jr, *Python tutorial* (Centrum voor Wiskunde en Informatica Amsterdam, The Netherlands, 1995).

36. R Core Team, *R: A Language and Environment for Statistical Computing* (R Foundation for Statistical Computing, Vienna, Austria, 2019; https://www.R-project.org/).

37. H. Wickham, *ggplot2: Elegant Graphics for Data Analysis* (Springer-Verlag New York, 2016; https://ggplot2.tidyverse.org).

38. C. O. Wilke, *cowplot: Streamlined Plot Theme and Plot Annotations for "ggplot2"* (2019; https://CRAN.R-project.org/package=cowplot).

39. E. Neuwirth, *RColorBrewer: ColorBrewer Palettes* (2014; https://CRAN.R-project.org/package=RColorBrewer).

40. D. Kahle, H. Wickham, ggmap: Spatial Visualization with ggplot2. *R J.* **5**, 144–161 (2013).

41. B. Vernot, *bvernot/branch_estim: v0.1-beta* (Zenodo, 2021; https://zenodo.org/record/4534664).

42. B. Vernot, *bvernot/make_sed_capture_targets: v0.1-beta* (Zenodo, 2021; https://zenodo.org/record/4534734).

43. F. Romagne, *mpieva/nuclear_sediment_pipeline: metagen_utils v1.21* (Zenodo, 2021; https://zenodo.org/record/4468181).

44. J. Visagie, *mpieva/biohazard-tools: Biohazard Tools v0.2* (Zenodo, 2021; https://zenodo.org/record/4616582).

45. K. Prüfer, Alignments of modern and archaic human genomes with primate outgroup genomes in tab-separated-values format (2021), (available at https://dx.doi.org/10.17617/3.5h).

46. J.-L. Arsuaga, I. Martínez, A. Gracia, J.-M. Carretero, E. Carbonell, Three new human skulls from the Sima de los Huesos Middle Pleistocene site in Sierra de Atapuerca, Spain. *Nature*. **362**, 534–537 (1993).

47. J. M. Bermúdez de Castro, J. L. Arsuaga, E. Carbonell, A. Rosas, I. Martínez, M. Mosquera, A hominid from the lower Pleistocene of Atapuerca, Spain: possible ancestor to Neandertals and modern humans. *Science*. **276**, 1392–1395 (1997).

48. J.-L. Arsuaga, I. Martínez, C. Lorenzo, A. Gracia, A. Muñoz, O. Alonso, J. Gallego, The human cranial remains from Gran Dolina Lower Pleistocene site (Sierra de Atapuerca, Spain). *J. Hum. Evol.* **37**, 431–457 (1999).

49. E. Carbonell, J. M. Bermúdez de Castro, J. M. Parés, A. Pérez-González, G. Cuenca-Bescós, A. Ollé, M. Mosquera, R. Huguet, J. van der Made, A. Rosas, R. Sala, J. Vallverdú, N. García, D. E. Granger, M. Martinón-Torres, X. P. Rodríguez, G. M. Stock, J. M. Vergès, E. Allué, F. Burjachs, I. Cáceres, A. Canals, A. Benito, C. Díez, M. Lozano, A. Mateos, M. Navazo, J. Rodríguez, J. Rosell, J. L. Arsuaga, The first hominin of Europe. *Nature*. **452**, 465–469 (2008).

50. J. L. Arsuaga, J.-M. Carretero, C. Lorenzo, A. Gómez-Olivencia, A. Pablos, L. Rodríguez, R. García-González, A. Bonmatí, R. M. Quam, A. Pantoja-Pérez, I. Martínez, A. Aranburu, A. Gracia-Téllez, E. Poza-Rey, N. Sala, N. García, A. A. de Velasco, G. Cuenca-Bescós, J. M. Bermúdez de Castro, E. Carbonell, Postcranial morphology of the middle Pleistocene humans from Sima de los Huesos, Spain. *Proc. Natl. Acad. Sci.* **112**, 11524–11529 (2015).

51. M. Mosquera, A. Ollé, A. Pérez-González, X. P. Rodríguez, M. Vaquero, J. M. Vergès, E. Carbonell, Valle de las Orquídeas: un yacimiento al aire libre del Pleistoceno Superior en la Sierra de Atapuerca (Burgos). *Trab. Prehist.* **64**, 143–155 (2007).

52. M. Navazo, R. Alonso-Alcalde, A. Benito-Calvo, J. C. Díez, A. Pérez-González, E. Carbonell, Hundidero: mis 4 open air neanderthal occupations in Sierra de Atapuerca. *Archaeol. Ethnol. Anthropol. Eurasia*. **39**, 29–41 (2011).

53. L. J. Arnold, M. Demuro, M. Navazo, A. Benito-Calvo, A. Pérez-González, OSL dating of the Middle Palaeolithic Hotel California site, Sierra de Atapuerca, north-central Spain. *Boreas*. **42**, 285–305 (2013).

54. M. Navazo, E. Carbonell, Neanderthal settlement patterns during MIS 4–3 in Sierra de Atapuerca (Burgos, Spain). *Quat. Int.* **331**, 267–277 (2014).

55. A. Aranburu, V. Martínez-Pillado, F. García, J. L. Arsuaga, A. Alcázar de Velasco, A. Bonmatí, N. García, A. Gracia, A. Gómez, J. Lira, C. Lorenzo, I. Martínez, A. I. Ortega, A. Pablos, A. Pantoja, R. M. Quam, N. Sala, (Avances de la Geomorfología en España 2010-2012. XII Reunión Nacional de Geomorfología, 397-400, 2012, 2012; https://geomorfologia.es/publicaciones-socios/avances-de-la-geomorfolog%C3%ADa-en-espa%C3%B1a-2010-2012).

56. V. Martínez-Pillado, A. Aranburu, J. L. Arsuaga, B. Ruiz-Zapata, M. J. Gil-García, H. Stoll, I. Yusta, E. Iriarte, J. M. Carretero, R. L. Edwards, H. Cheng, Upper Pleistocene and Holocene palaeoenvironmental records in Cueva Mayor karst (Atapuerca, Spain) from

different proxies: speleothem crystal fabrics, palynology and archaeology. *Int. J. Speleol.* **43** (2014), doi:http://dx.doi.org/10.5038/1827-806X.43.1.1.

57. C. B. Ramsey, Probability and Dating. *Radiocarbon*. **40**, 461–474 (1997).

58. C. Ramsey, Bayesian Analysis of Radiocarbon Dates. *Radiocarbon*. **51**, 337–360 (2009).

59. P. J. Reimer, W. E. N. Austin, E. Bard, A. Bayliss, P. G. Blackwell, C. B. Ramsey, M. Butzin, H. Cheng, R. L. Edwards, M. Friedrich, P. M. Grootes, T. P. Guilderson, I. Hajdas, T. J. Heaton, A. G. Hogg, K. A. Hughen, B. Kromer, S. W. Manning, R. Muscheler, J. G. Palmer, C. Pearson, J. van der Plicht, R. W. Reimer, D. A. Richards, E. M. Scott, J. R. Southon, C. S. M. Turney, L. Wacker, F. Adolphi, U. Büntgen, M. Capano, S. M. Fahrni, A. Fogtmann-Schulz, R. Friedrich, P. Köhler, S. Kudsk, F. Miyake, J. Olsen, F. Reinig, M. Sakamoto, A. Sookdeo, S. Talamo, The IntCal20 Northern Hemisphere Radiocarbon Age Calibration Curve (0–55 cal kBP). *Radiocarbon*. **62**, 725–757 (2020).

60. H. Cheng, R. Lawrence Edwards, C.-C. Shen, V. J. Polyak, Y. Asmerom, J. Woodhead, J. Hellstrom, Y. Wang, X. Kong, C. Spötl, X. Wang, E. Calvin Alexander, Improvements in ^{230}Th dating, ^{230}Th and ^{234}U half-life values, and U–Th isotopic measurements by multi-collector inductively coupled plasma mass spectrometry. *Earth Planet. Sci. Lett.* **371–372**, 82–91 (2013).

61. A. H. Jaffey, K. F. Flynn, L. E. Glendenin, W. C. Bentley, A. M. Essling, Precision Measurement of Half-Lives and Specific Activities of ^{235}U and ^{238}U. *Phys. Rev. C*. **4**, 1889–1906 (1971).

62. J. M. Parés, A. I. Ortega, A. Benito-Calvo, A. Aranburu, J. L. Arsuaga, J. M. Bermúdez de Castro, E. Carbonell, 19. Paleomagnetic constraints on the Atapuerca karst development (N Spain) (2016), doi:10.1130/2016.2516(22).

63. A. W. Briggs, U. Stenzel, P. L. F. Johnson, R. E. Green, J. Kelso, K. Prüfer, M. Meyer, J. Krause, M. T. Ronan, M. Lachmann, S. Pääbo, Patterns of damage in genomic DNA sequences from a Neandertal. *Proc. Natl. Acad. Sci.* **104**, 14616–14621 (2007).

64. M. Meyer, A. W. Briggs, T. Maricic, B. Höber, B. Höffner, J. Krause, A. Weihmann, S. Pääbo, M. Hofreiter, From micrograms to picograms: quantitative PCR reduces the material demands of high-throughput sequencing. *Nucleic Acids Res.* **36**, e5 (2008).

65. M. Kircher, S. Sawyer, M. Meyer, Double indexing overcomes inaccuracies in multiplex sequencing on the Illumina platform. *Nucleic Acids Res.* **40**, e3 (2012).

66. G. Renaud, U. Stenzel, J. Kelso, leeHom: adaptor trimming and merging for Illumina sequencing reads. *Nucleic Acids Res.* **42**, e141 (2014).

67. H. Li, R. Durbin, Fast and accurate short read alignment with Burrows–Wheeler transform. *Bioinformatics*. **25**, 1754–1760 (2009).

68. K. D. Pruitt, G. R. Brown, S. M. Hiatt, F. Thibaud-Nissen, A. Astashyn, O. Ermolaeva, C. M. Farrell, J. Hart, M. J. Landrum, K. M. McGarvey, M. R. Murphy, N. A. O'Leary, S. Pujar, B. Rajput, S. H. Rangwala, L. D. Riddick, A. Shkeda, H. Sun, P. Tamez, R. E. Tully, C. Wallin, D. Webb, J. Weber, W. Wu, M. DiCuccio, P. Kitts, D. R. Maglott, T. D. Murphy, J.

M. Ostell, RefSeq: an update on mammalian reference sequences. *Nucleic Acids Res.* **42**, D756-763 (2014).

69. S. F. Altschul, W. Gish, W. Miller, E. W. Myers, D. J. Lipman, Basic local alignment search tool. *J. Mol. Biol.* **215**, 403–410 (1990).

70. R. R. Hudson, Generating samples under a Wright–Fisher neutral model of genetic variation. *Bioinformatics*. **18**, 337–338 (2002).

71. T. Maricic, M. Whitten, S. Pääbo, Multiplexed DNA Sequence Capture of Mitochondrial Genomes Using PCR Products. *PLOS ONE*. **5**, e14004 (2010).

72. R. M. Andrews, I. Kubacka, P. F. Chinnery, R. N. Lightowlers, D. M. Turnbull, N. Howell, Reanalysis and revision of the Cambridge reference sequence for human mitochondrial DNA. *Nat. Genet.* **23**, 147–147 (1999).

73. R. E. Green, A.-S. Malaspinas, J. Krause, A. W. Briggs, P. L. F. Johnson, C. Uhler, M. Meyer, J. M. Good, T. Maricic, U. Stenzel, K. Prüfer, M. Siebauer, H. A. Burbano, M. Ronan, J. M. Rothberg, M. Egholm, P. Rudan, D. Brajković, Ž. Kućan, I. Gušić, M. Wikström, L. Laakkonen, J. Kelso, M. Slatkin, S. Pääbo, A Complete Neandertal Mitochondrial Genome Sequence Determined by High-Throughput Sequencing. *Cell*. **134**, 416–426 (2008).

74. Q. Fu, A. Mittnik, P. L. F. Johnson, K. Bos, M. Lari, R. Bollongino, C. Sun, L. Giemsch, R. Schmitz, J. Burger, A. M. Ronchitelli, F. Martini, R. G. Cremonesi, J. Svoboda, P. Bauer, D. Caramelli, S. Castellano, D. Reich, S. Pääbo, J. Krause, A Revised Timescale for Human Evolution Based on Ancient Mitochondrial Genomes. *Curr. Biol.* **23**, 553–559 (2013).

75. S. Horai, K. Hayasaka, R. Kondo, K. Tsugane, N. Takahata, Recent African origin of modern humans revealed by complete sequences of hominoid mitochondrial DNAs. *Proc. Natl. Acad. Sci.* **92**, 532–536 (1995).

76. K. Katoh, D. M. Standley, MAFFT Multiple Sequence Alignment Software Version 7: Improvements in Performance and Usability. *Mol. Biol. Evol.* **30**, 772–780 (2013).

77. R. E. Kass, A. E. Raftery, Bayes Factors. *J. Am. Stat. Assoc.* **90**, 773–795 (1995).

78. G. Baele, W. L. S. Li, A. J. Drummond, M. A. Suchard, P. Lemey, Accurate model selection of relaxed molecular clocks in bayesian phylogenetics. *Mol. Biol. Evol.* **30**, 239–243 (2013).

79. A. D. Leaché, M. K. Fujita, V. N. Minin, R. R. Bouckaert, Species delimitation using genome-wide SNP data. *Syst. Biol.* **63**, 534–542 (2014).

80. K. Tamura, M. Nei, Estimation of the number of nucleotide substitutions in the control region of mitochondrial DNA in humans and chimpanzees. *Mol. Biol. Evol.* **10**, 512–526 (1993).

81. R. E. Wood, T. F. G. Higham, T. D. Torres, N. Tisnérat-Laborde, H. Valladas, J. E. Ortiz, C. Lalueza-Fox, S. Sánchez-Moral, J. C. Cañaveras, A. Rosas, D. Santamaría, M. D. L. Rasilla, A New Date for the Neanderthals from El Sidrón Cave (Asturias, Northern Spain). *Archaeometry*. **55**, 148–158 (2013).

82. L. Schaeffer, H. Pimentel, N. Bray, P. Melsted, L. Pachter, Pseudoalignment for metagenomic read assignment. *Bioinformatics*. **33**, 2082–2088 (2017).

83. P. Sagulenko, V. Puller, R. A. Neher, TreeTime: Maximum-likelihood phylodynamic analysis. *Virus Evol.* **4** (2018), doi:10.1093/ve/vex042.

84. G. A. Taylor, H. Kirk, L. Coombe, S. D. Jackman, J. Chu, K. Tse, D. Cheng, E. Chuah, P. Pandoh, R. Carlsen, Y. Zhao, A. J. Mungall, R. Moore, I. Birol, M. Franke, M. A. Marra, C. Dutton, S. J. M. Jones, The Genome of the North American Brown Bear or Grizzly: Ursus arctos ssp. horribilis. *Genes*. **9** (2018), doi:10.3390/genes9120598.

85. N. A. O'Leary, M. W. Wright, J. R. Brister, S. Ciufo, D. Haddad, R. McVeigh, B. Rajput, B. Robbertse, B. Smith-White, D. Ako-Adjei, A. Astashyn, A. Badretdin, Y. Bao, O. Blinkova, V. Brover, V. Chetvernin, J. Choi, E. Cox, O. Ermolaeva, C. M. Farrell, T. Goldfarb, T. Gupta, D. Haft, E. Hatcher, W. Hlavina, V. S. Joardar, V. K. Kodali, W. Li, D. Maglott, P. Masterson, K. M. McGarvey, M. R. Murphy, K. O'Neill, S. Pujar, S. H. Rangwala, D. Rausch, L. D. Riddick, C. Schoch, A. Shkeda, S. S. Storz, H. Sun, F. Thibaud-Nissen, I. Tolstoy, R. E. Tully, A. R. Vatsan, C. Wallin, D. Webb, W. Wu, M. J. Landrum, A. Kimchi, T. Tatusova, M. DiCuccio, P. Kitts, T. D. Murphy, K. D. Pruitt, Reference sequence (RefSeq) database at NCBI: current status, taxonomic expansion, and functional annotation. *Nucleic Acids Res.* **44**, D733-745 (2016).

86. K. Prüfer, snpAD: an ancient DNA genotype caller. *Bioinformatics*. **34**, 4165–4171 (2018).

87. J. Herrero, M. Muffato, K. Beal, S. Fitzgerald, L. Gordon, M. Pignatelli, A. J. Vilella, S. M. J. Searle, R. Amode, S. Brent, W. Spooner, E. Kulesha, A. Yates, P. Flicek, Ensembl comparative genomics resources. *Database J. Biol. Databases Curation*. **2016** (2016), doi:10.1093/database/bav096.

88. G. Benson, Tandem repeats finder: a program to analyze DNA sequences. *Nucleic Acids Res.* **27**, 573–580 (1999).

89. D. Karolchik, A. S. Hinrichs, T. S. Furey, K. M. Roskin, C. W. Sugnet, D. Haussler, W. J. Kent, The UCSC Table Browser data retrieval tool. *Nucleic Acids Res.* **32**, D493–D496 (2004).

90. W. J. Kent, C. W. Sugnet, T. S. Furey, K. M. Roskin, T. H. Pringle, A. M. Zahler, D. Haussler, The human genome browser at UCSC. *Genome Res.* **12**, 996–1006 (2002).

91. Q. Fu, C. Posth, M. Hajdinjak, M. Petr, S. Mallick, D. Fernandes, A. Furtwängler, W. Haak, M. Meyer, A. Mittnik, B. Nickel, A. Peltzer, N. Rohland, V. Slon, S. Talamo, I. Lazaridis, M. Lipson, I. Mathieson, S. Schiffels, P. Skoglund, A. P. Derevianko, N. Drozdov, V. Slavinsky, A. Tsybankov, R. G. Cremonesi, F. Mallegni, B. Gély, E. Vacca, M. R. G. Morales, L. G. Straus, C. Neugebauer-Maresch, M. Teschler-Nicola, S. Constantin, O. T. Moldovan, S. Benazzi, M. Peresani, D. Coppola, M. Lari, S. Ricci, A. Ronchitelli, F. Valentin, C. Thevenet, K. Wehrberger, D. Grigorescu, H. Rougier, I. Crevecoeur, D. Flas, P. Semal, M. A. Mannino, C. Cupillard, H. Bocherens, N. J. Conard, K. Harvati, V. Moiseyev, D. G. Drucker, J. Svoboda, M. P. Richards, D. Caramelli, R. Pinhasi, J. Kelso, N. Patterson, J. Krause, S. Pääbo, D. Reich, The genetic history of Ice Age Europe. *Nature*. **534**, 200–205 (2016).

674 92. Q. Fu, M. Hajdinjak, O. T. Moldovan, S. Constantin, S. Mallick, P. Skoglund, N. Patterson,
675 N. Rohland, I. Lazaridis, B. Nickel, B. Viola, K. Prüfer, M. Meyer, J. Kelso, D. Reich, S.
676 Pääbo, An early modern human from Romania with a recent Neanderthal ancestor.
677 *Nature*. **524**, 216–219 (2015).

678 93. T. 1000 G. P. Consortium, An integrated map of genetic variation from 1,092 human
679 genomes. *Nature*. **491**, 56–65 (2012).

680 94. A. Smit, R. Hubley, P. Green, *RepeatMasker Open-4.0* (2013;
681 http://www.repeatmasker.org).

682 95. A. Morgulis, E. M. Gertz, A. A. Schäffer, R. Agarwala, A Fast and Symmetric DUST
683 Implementation to Mask Low-Complexity DNA Sequences. *J. Comput. Biol.* **13**, 1028–1040
684 (2006).

685 96. C. de Filippo, M. Meyer, K. Prüfer, Quantifying and reducing spurious alignments for the
686 analysis of ultra-short ancient DNA sequences. *BMC Biol.* **16**, 121 (2018).

687 97. T. Günther, C. Nettelblad, The presence and impact of reference bias on population
688 genomic studies of prehistoric human populations. *PLOS Genet.* **15**, e1008302 (2019).

689 98. C. L. Schoch, S. Ciufo, M. Domrachev, C. L. Hotton, S. Kannan, R. Khovanskaya, D.
690 Leipe, R. Mcveigh, K. O'Neill, B. Robbertse, S. Sharma, V. Soussov, J. P. Sullivan, L. Sun,
691 S. Turner, I. Karsch-Mizrachi, NCBI Taxonomy: a comprehensive update on curation,
692 resources and tools. *Database J. Biol. Databases Curation*. **2020** (2020),
693 doi:10.1093/database/baaa062.

694 99. L. Bokelmann, M. Hajdinjak, S. Peyrégne, S. Brace, E. Essel, C. de Filippo, I. Glocke, S.
695 Grote, F. Mafessoni, S. Nagel, J. Kelso, K. Prüfer, B. Vernot, I. Barnes, S. Pääbo, M.
696 Meyer, C. Stringer, A genetic analysis of the Gibraltar Neanderthals. *Proc. Natl. Acad. Sci.*
697 **116**, 15610–15615 (2019).

698 100. H. Li, R. Durbin, Inference of human population history from individual whole-genome
699 sequences. *Nature*. **475**, 493–496 (2011).

700 101. P. Skoglund, A. Götherström, M. Jakobsson, Estimation of Population Divergence Times
701 from Non-Overlapping Genomic Sequences: Examples from Dogs and Wolves. *Mol. Biol.*
702 *Evol.* **28**, 1505–1517 (2011).

703 102. B. M. Peter, "100,000 years of gene flow between Neandertals and Denisovans in the Altai
704 mountains" (Cold Spring Harbor Laboratory, 2020), p. 2020.03.13.990523, (available at
705 doi.org/10.1101/2020.03.13.990523).

706 103. F. Racimo, G. Renaud, M. Slatkin, Joint Estimation of Contamination, Error and
707 Demography for Nuclear DNA from Ancient Humans. *PLOS Genet.* **12**, e1005972 (2016).

708

Acknowledgements

We thank S. Pääbo for supporting the project and commenting on the manuscript, Moritz C. Meyer and K. O'Gorman for help with sampling, B. Schellbach and A. Weihmann for help in the lab, S. Peyregne for data assistance, L. Jáuregui for organizational support, and the whole Galería de las Estatuas, Chagyrskaya Cave and Denisova Cave excavation and research teams for providing the foundations that made this project possible. **Funding:** was provided by the Max Planck Society, the European Research Council (Grant Agreement 694707 to Svante Pääbo) and the Australian Research Council (fellowships FL130100116 to R.G.R., FT140100384 to B.L. and FT150100138 to Z.J.). The archaeological field studies were funded by the Russian Foundation for Basic Research (project 20-29-010116 for M.B.K., M.V.S. and A.P.D.), the Russian Science Foundation (projects 21-18-00089 for M.B.K., M.V.S. and A.P.D. and 19-48-04107 to A.I.K.), and the Junta de Castilla y León and Fundación Atapuerca. The geological study in Chagyrskaya Cave was supported by the National Science Center, Poland (project 2018/29/B/ST10/00906 to M.T.K.). A.G.O. and N.S were supported by Ramón y Cajal (RYC-2017-22558) and Juan de la Cierva-Incorporación (IJCI-2017-32804) fellowships, respectively. B.Vi.'s research was supported by an Insight grant of the Social Sciences and Humanities Research Council (Canada). Further support was provided by the FEDER/Ministerio de Ciencia e Innovación-Agencia Estatal de Investigación (projects PGC2018-093925-B-C31, PGC2018-093925-B-C32, and PGC2018-093925-B-C33). **Author contributions:** B.Ve. and M.M. conceived the study. A.G-O., Z.J., N.S., A.Pa., A.A., J.M.B., E.C., B.L., M.T.K., A.I.K., K.A.K., M.B.K., M.V.S., A.P.D., B.Vi., D.L.H., R.G.R., J-L.A., M.M. sampled sediments and/or provided archaeological context and interpretation of results. E.I.Z., E.E., S.N., B.N., J.R, A.S. performed aDNA extraction and sequencing. B.Ve., E.I.Z., V.S., F.M., F.R., A. Pe., M.P., S.G., B.P., J.K., M.M. analyzed data. B.Ve., E.I.Z., A.G-O., Z.J., V.S., R.G.R., J-L.A., M.M. wrote the manuscript with input from the remaining authors. C**ompeting interests:** The authors declare that they have no competing interests. **Data and materials availability:** All data needed to evaluate the conclusions in the paper are present in the paper and/or the Supplementary Materials. Sequencing data has been deposited in the ENA, reference number PRJEB42656. Software is archived at Zenodo: 10.5281/zenodo.4534664, 10.5281/zenodo.4534734,

10.5281/zenodo.4468181, 10.5281/zenodo.4616582 (*41–44*). Primate alignments available at https://dx.doi.org/10.17617/3.5h (*45*).

Figure Legends

Figure 1. A) Geographic locations of all skeletal (black) and sediment (red) samples with >0.0001x coverage. Each bar represents one sample; height is the age of the sample. B) Stratigraphic profile of the sampled section at Chagyrskaya Cave. Sediment samples were collected in 10 vertical columns and numbered from bottom to top. Colored circles denote individual sample locations. C) Cross-section of Galería de las Estatuas showing the locations of the two test pits, GE-I and GE-II, and detailed stratigraphic columns showing the lithostratigraphic units (LUs) and ages obtained.

Figure 2. A) Mitochondrial phylogeny, including five haplotypes inferred from sediment samples (red labels). Five mtDNA groupings are labeled (colored dots and vertical bars). B) Probabilistic phylogenetic placement of mtDNA from 97 sediment sub-samples from 63 sediment samples, Chagyrskaya Cave (left) and Galería de las Estatuas (right). Samples divided by white lines. Sub-samples from which mtDNA haplotypes were inferred are denoted with red boxes.

Figure 3. A) Multiple sequence alignment (MSA) of 15 mammalian species, two Neandertals and one Denisovan. This region has low sequence diversity between hominins and non-primate mammals. B) High-diversity MSA. C) Faunal mis-alignment (purple) in the human genome as a function of mammalian diversity (the minimum base-pair divergence between *Homo sapiens* and nine non-primate mammalian sequences), – compared to the alignment of DNA fragments from the *Mezmaiskaya 1* Neandertal (orange; *Mez1*); y-axis is relative coverage compared to the first bin. D) Ascertainment of hominin-diagnostic alleles; ancestral alleles are indicative of faunal-misalignment. E) Proportion of ancestral alleles at hominin-diagnostic sites, in *Mezmaiskaya 1* and simulated *Ursus arctos* ancient DNA.

Figure 4. A) Neandertal versus Denisovan alleles place sediment (top row and bottom left) and skeletal (bottom right) samples into broad population groups. All samples shown in grey in all plots. CI are 95% binomial confidence intervals. B) X-autosome proportions for skeletal and sediment samples. CI are 95% binomial confidence intervals. Male and Female CI bands (grey) denote male and female skeletal samples with narrowest CI, respectively. Evidence of single

(black) or multiple (orange) mtDNA haplotypes taken from Table S3. All samples labeled in Figure S17. C) Modeling p(*X*=1), the probability that a sediment sample *X* carries a derived allele at an example SNP in the genome, where *Vindija* is heterozygous (0/1) and *Chagyrskaya* and *Altai* are homozygous ancestral (0/0). p(*X*=1) depends on the time at which sample *X* diverges from the Neandertal phylogeny (black dots are hypothetical split times; inset shows p(*X*=1) for each split time). D) Likelihood surfaces (lines) and maximum likelihood estimates of branching times for four sediment samples (black dots).

Figure 5. A) Population split estimates for sediments across four layers of Galería de las Estatuas (black dot is maximum likelihood estimate; thick lines are 95% block bootstrap CI; CI clipped at 160 ka for GE-II-B108a and GE-I-A4g), plotted on Neandertal population tree, with *Vindija 33.19* (v), *Chagyrskaya 8* (c) and the *Altai Neandertal* (a). For each layer, sub-samples were merged to produce per-layer estimates (grey blocks, "merge"). For pit I/Layer 4, only samples with *HST*-like mtDNA (green squares) were merged. Bottom row shows estimated number of Neandertal SNPs used in the branch-time analysis (grey) and modern human contamination estimates (blue). B) Same, for three skeletal samples. For *Mezmaiskaya 1*, a 1x coverage genome was down-sampled to ~60k informative reads. C) Clustered split times in the Neandertal phylogeny suggest successive radiations of Neandertal populations approximately 105 and 135 thousand years ago.

List of Supplementary Materials:

Materials and Methods
Figures S1 – S26
Tables S1 – S14
References 46-103

A

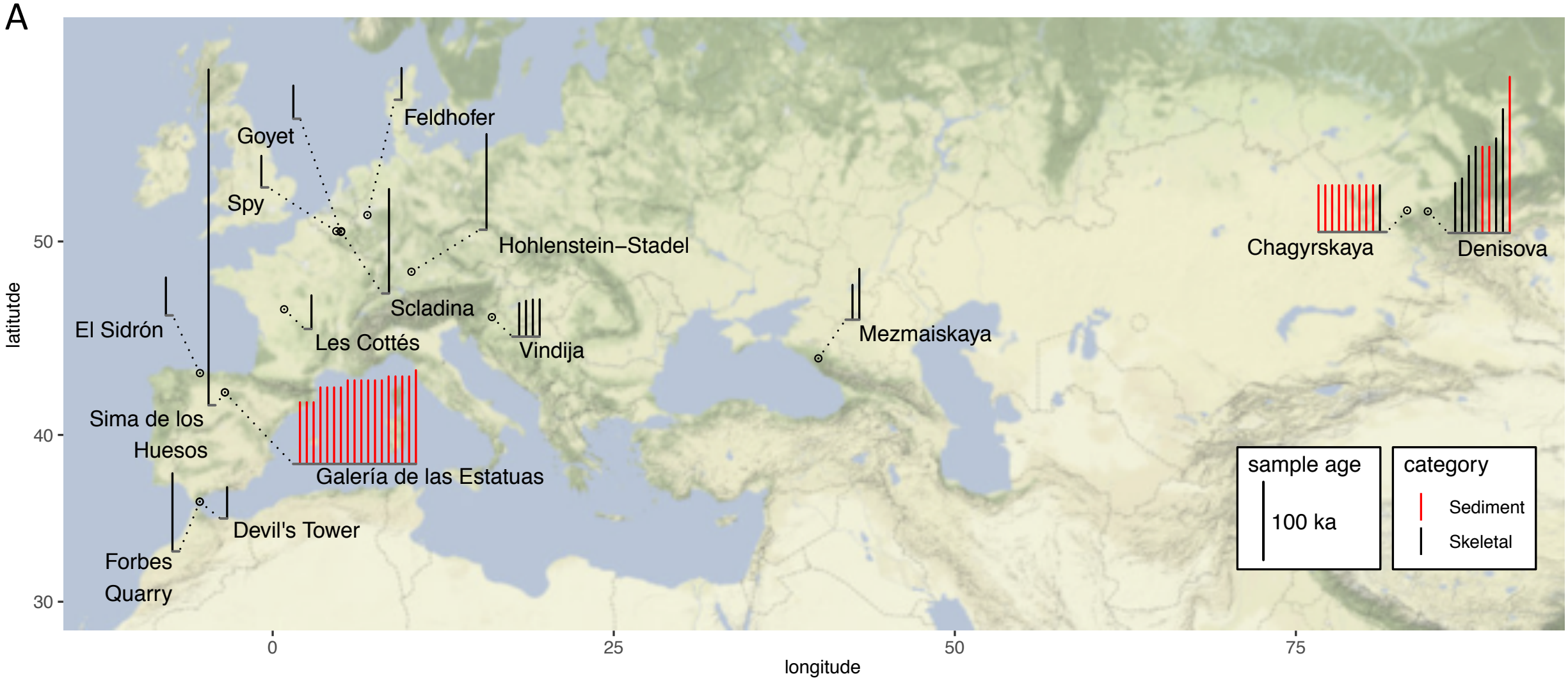
Feldhofer
Goyet
Spy
Hohlenstein–Stadel
Scladina
El Sidrón
Les Cottés
Vindija
Mezmaiskaya
Chagyrskaya
Denisova
Sima de los Huesos
Galería de las Estatuas
Devil's Tower
Forbes Quarry
latitutde
longitude
50
40
30
0
25
50
75
sample age
100 ka
category
Sediment
Skeletal

B

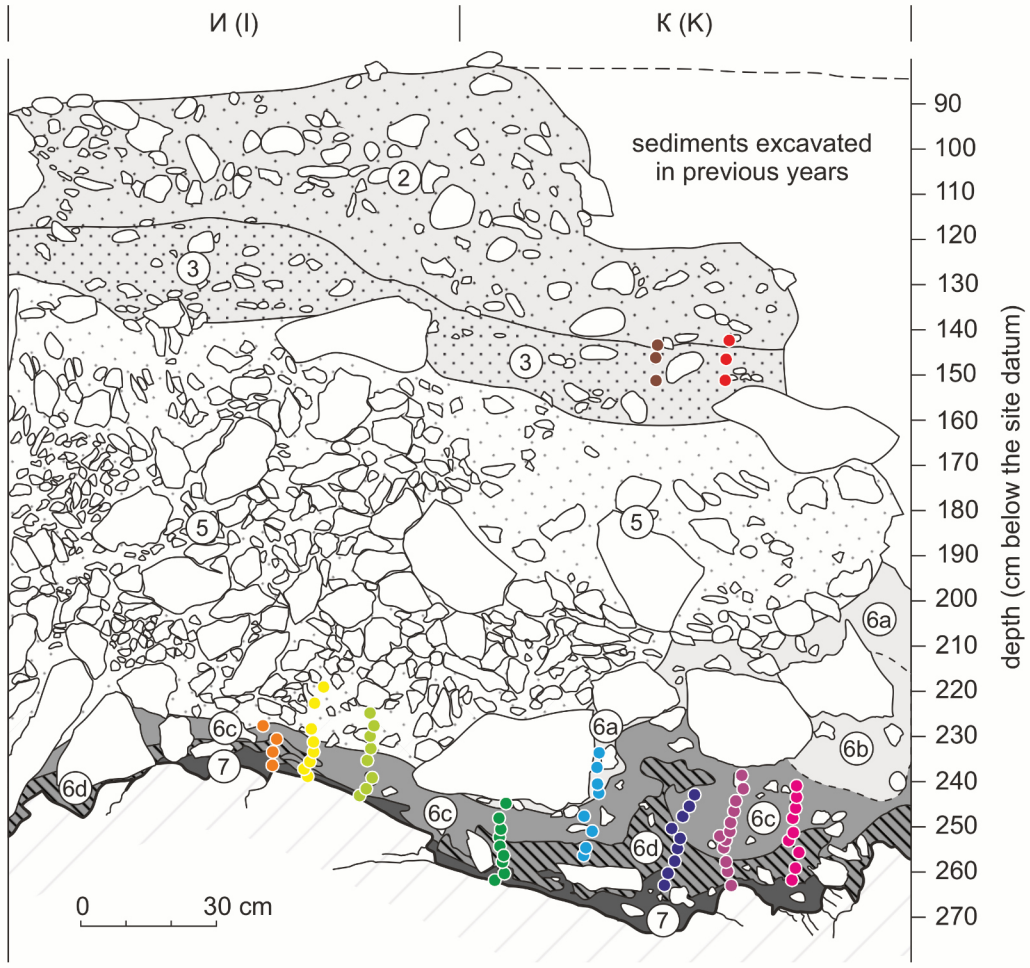
И (I)
К (К)
sediments excavated in previous years
depth (cm below the site datum)
0
30 cm
Sediment samples:
3001–3009
3010–3021
3022–3030
3031–3038
3039–3047
3048–3055
3056–3063
3064–3067
3068–3070
3071–3073

C

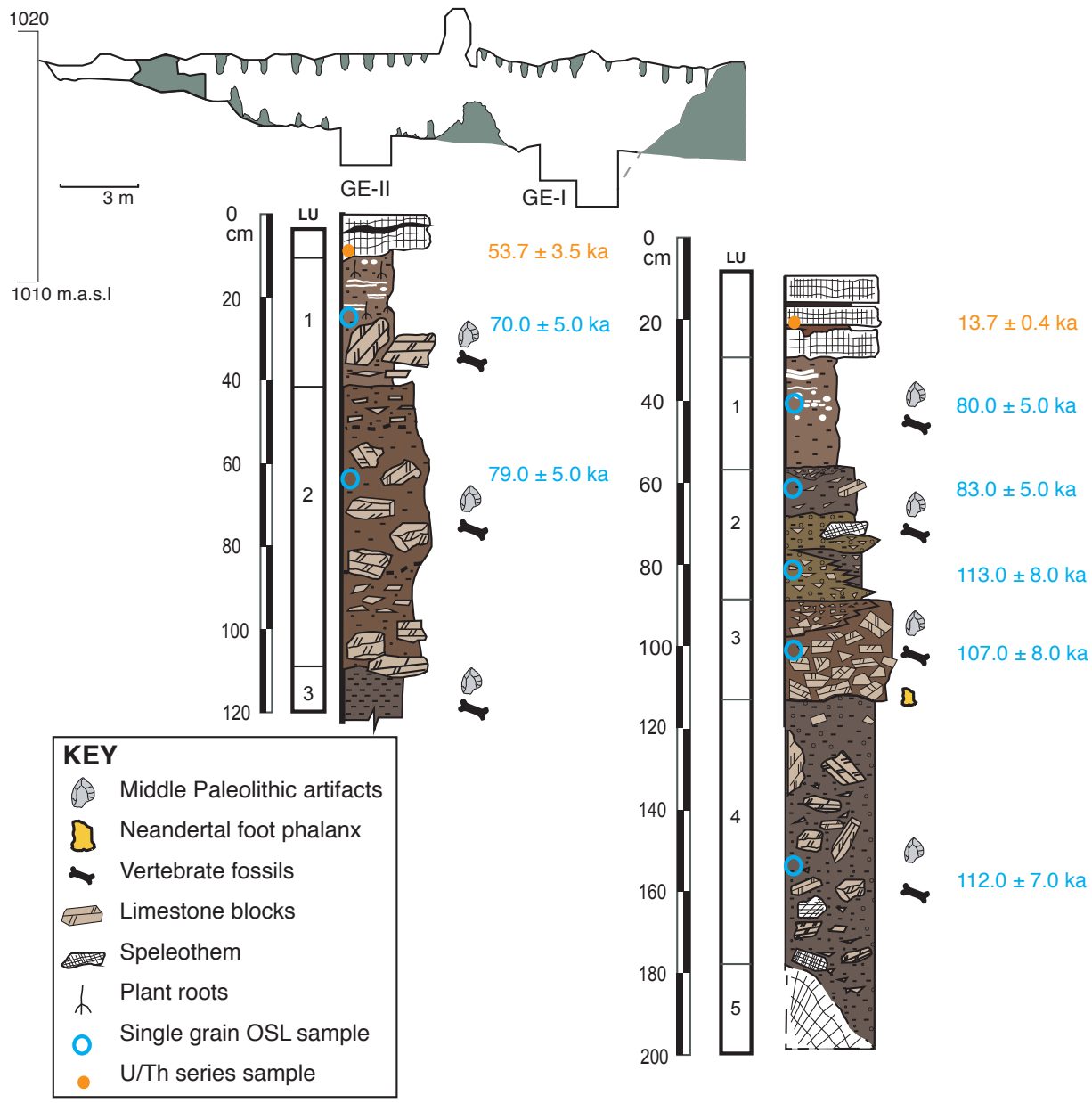
1020
1010 m.a.s.l
3 m
GE-II
GE-I
LU
53.7 ± 3.5 ka
70.0 ± 5.0 ka
79.0 ± 5.0 ka
13.7 ± 0.4 ka
80.0 ± 5.0 ka
83.0 ± 5.0 ka
113.0 ± 8.0 ka
107.0 ± 8.0 ka
112.0 ± 7.0 ka
KEY
Middle Paleolithic artifacts
Neandertal foot phalanx
Vertebrate fossils
Limestone blocks
Speleothem
Plant roots
Single grain OSL sample
U/Th series sample

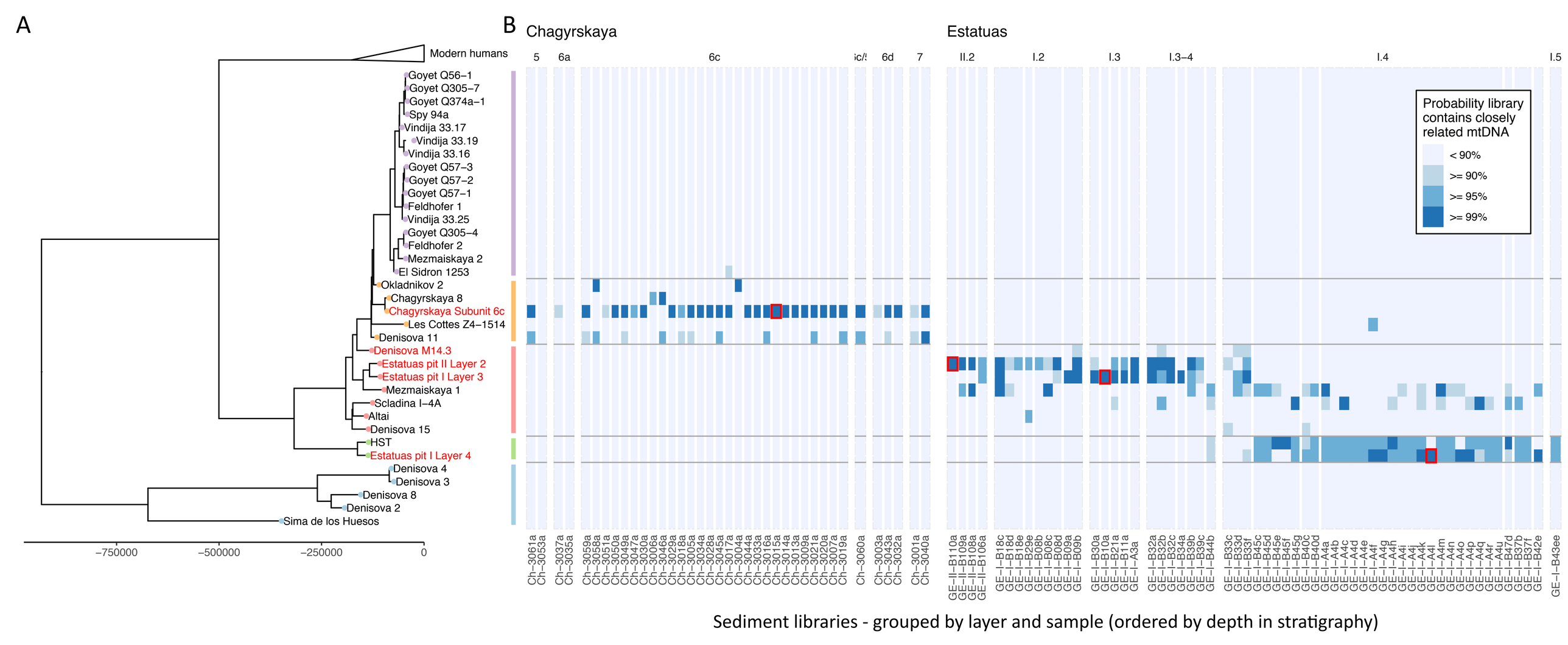
A
Modern humans
Goyet Q56−1
Goyet Q305−7
Goyet Q374a−1
Spy 94a
Vindija 33.17
Vindija 33.19
Vindija 33.16
Goyet Q57−3
Goyet Q57−2
Goyet Q57−1
Feldhofer 1
Vindija 33.25
Goyet Q305−4
Feldhofer 2
Mezmaiskaya 2
El Sidron 1253
Okladnikov 2
Chagyrskaya 8
Chagyrskaya Subunit 6c
Les Cottes Z4−1514
Denisova 11
Denisova M14.3
Estatuas pit II Layer 2
Estatuas pit I Layer 3
Mezmaiskaya 1
Scladina I−4A
Altai
Denisova 15
HST
Estatuas pit I Layer 4
Denisova 4
Denisova 3
Denisova 8
Denisova 2
Sima de los Huesos
−750000
−500000
−250000
0
B
Chagyrskaya
Estatuas
5
6a
6c
6d
7
II.2
I.2
I.3
I.3−4
I.4
I.5
Probability library contains closely related mtDNA
< 90%
>= 90%
>= 95%
>= 99%
Ch−3061a
Ch−3053a
Ch−3037a
Ch−3035a
Ch−3059a
Ch−3058a
Ch−3051a
Ch−3050a
Ch−3049a
Ch−3047a
Ch−3030a
Ch−3006a
Ch−3046a
Ch−3029a
Ch−3018a
Ch−3005a
Ch−3034a
Ch−3028a
Ch−3045a
Ch−3017a
Ch−3004a
Ch−3044a
Ch−3033a
Ch−3016a
Ch−3015a
Ch−3014a
Ch−3013a
Ch−3009a
Ch−3021a
Ch−3020a
Ch−3007a
Ch−3019a
Ch−3060a
Ch−3003a
Ch−3043a
Ch−3032a
Ch−3001a
Ch−3040a
GE−II−B110a
GE−II−B109a
GE−II−B108a
GE−II−B106a
GE−I−B18c
GE−I−B18d
GE−I−B18e
GE−I−B29e
GE−I−B08b
GE−I−B08c
GE−I−B08d
GE−I−B09a
GE−I−B09b
GE−I−B30a
GE−I−B10a
GE−I−B21a
GE−I−B11a
GE−I−A3a
GE−I−B32a
GE−I−B32b
GE−I−B32c
GE−I−B34a
GE−I−B39b
GE−I−B39c
GE−I−B44b
GE−I−B33c
GE−I−B33d
GE−I−B33f
GE−I−B45c
GE−I−B45d
GE−I−B45e
GE−I−B45f
GE−I−B45g
GE−I−B40c
GE−I−B40d
GE−I−A4a
GE−I−A4b
GE−I−A4c
GE−I−A4d
GE−I−A4e
GE−I−A4f
GE−I−A4g
GE−I−A4h
GE−I−A4i
GE−I−A4j
GE−I−A4k
GE−I−A4l
GE−I−A4m
GE−I−A4n
GE−I−A4o
GE−I−A4p
GE−I−A4q
GE−I−A4r
GE−I−A4u
GE−I−B47d
GE−I−B37b
GE−I−B37f
GE−I−B42e
GE−I−B43ee
Sediment libraries - grouped by layer and sample (ordered by depth in stratigraphy)

A

Low-diversity MSA – Chr1:19684006 (rev)

```
GTCTACCTCTGGGATCTGGATCATGGCTTTGCTGGAGTGATCCTCATAAAGA Homo sapiens
.........................G.......................... Altai Neandertal
.........................G.......................... Vindija Neandertal
.......................................................... Denisovan
.......................................................... Pan troglodytes
.......................................................... Gorilla gorilla
.......................................................... Pongo abelii
.......................................................... Macaca mulatta
.......................................................... Callithrix jacchus
............................G............................. Oryctolagus cuniculus
..............C........................................... Rattus norvegicus
..............T........................................... Mus musculus
....................C..T..C.....C.......................... Sus scrofa
............C..........T.......................... Ovis aries
.........................T.......................... Bos taurus
.......................................................... Equus caballus
............C..........T.......................... Canis familiaris
.........................T.......................... Felis catus
```

B

High-diversity MSA - Chr1:11236464 (rev)

```
TGAGCGTTGCCCCAGCTGTGCCTGCAGATGCTCCTTG--CTGCCTGAGGACTTT Homo sapiens
.........................T.......................... Altai Neandertal
.........................T.......................... Vindija Neandertal
.......................................................... Denisovan
........C.......................................... Pan troglodytes
........C.......................................... Gorilla gorilla
........C.......................................... Pongo abelii
....T...C......A.......................................... Macaca mulatta
....T...C......A..............T...C....T.............. Callithrix jacchus
....T...C......A...C-....C.G.......CA.T.....C..-A.--.. Oryctolagus cuniculus
C....AC..----...A...A-GCA..........CG...TCTG...G.C.--.C Rattus norvegicus
CA...A..T---...A..GA-GCC..........AGT...A.....G.C.--.C Mus musculus
.A...AGCC.T....A.....................C.T.G..A.-----.A.. Sus scrofa
....TAG.C......A..CCA.......C......CTT.G..A...---G.... Ovis aries
....TAG.C......A..CCA.......C......C.T.G..A...---G.... Bos taurus
.A....G-C......A....A....T.........C-T.T..A.--------.-- Equus caballus
......G.C......A....A.C.T...........AT.T..A.---------- Canis familiaris
.A....G.C......A....A.C.............AT.T..A.---------- Felis catus
```

C

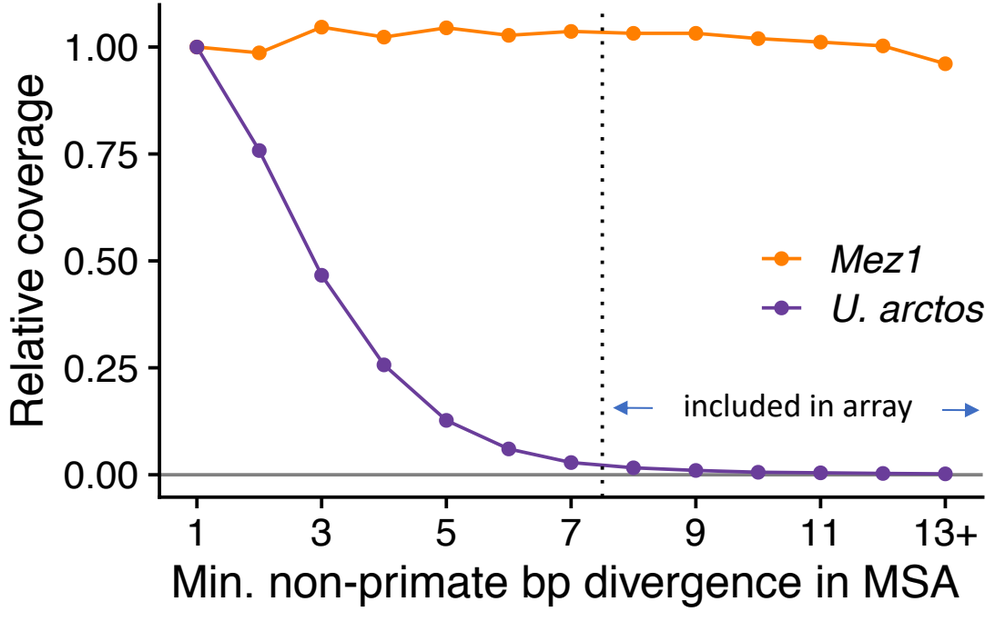

D

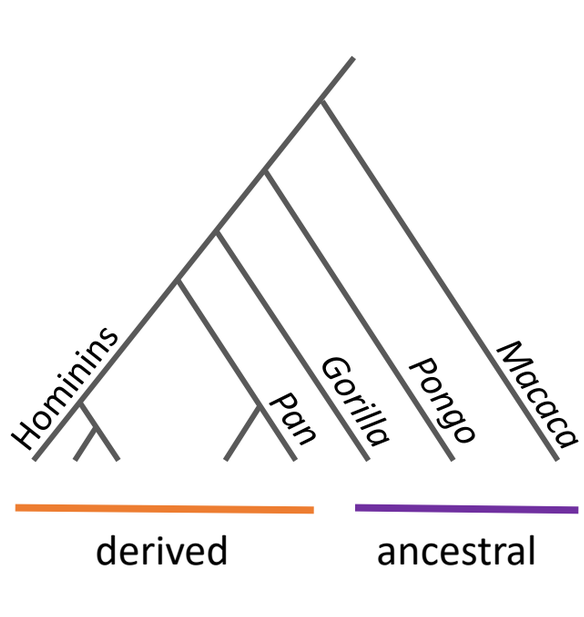

E

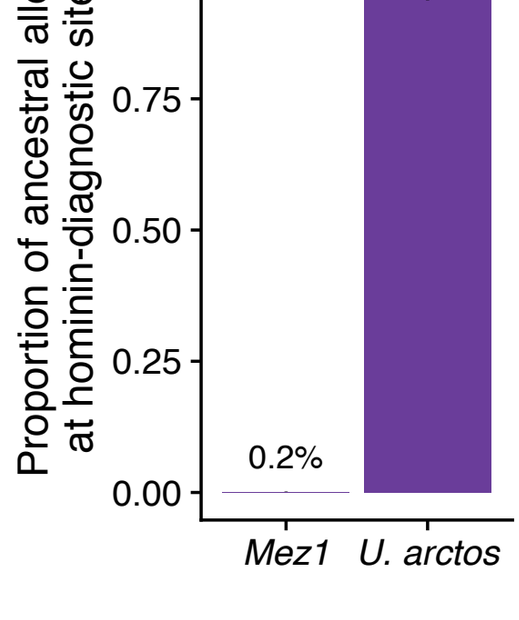

A

Population assignments

Denisova sediments

Chagyrskaya sediments

Estatuas sediments

Skeletal

mtDNA
Denisovan
Neandertal

Denisova 11

Prop. Denisovan derived alleles

Prop. Altai Neandertal derived alleles

B

X-autosome proportions indicate sex

Skeletal

Sediment

Mult. MT
Single MT
Unknown

Female CI

Male CI

GE-II-B110a

GE-I-B10a

Ch-3058a

De-M14.3a

GE-I-A4l

X proportion

Female

Male

Chag.

Den.

Est.

C

Modeling population split time of sample X

Example for one SNP

Time (ka)

p(X = 1)

1

2

3

4

5

X?

Altai
0/0

Chagyrskaya 8
0/0

Vindija 33.19
0/1

D

Divergence from Neandertal lineage

Maximum likelihood estimates

log(likelihood)

De-E11.4
Denisova Cave
East Chamber
Layer 11.4

Ch-3058a
Chagyrskaya Cave
Layer 6c

De-M14.3
Denisova Cave
Main Chamber
Layer 14.3

Ch-3007a
Chagyrskaya Cave
Layer 6c

Time (ka)

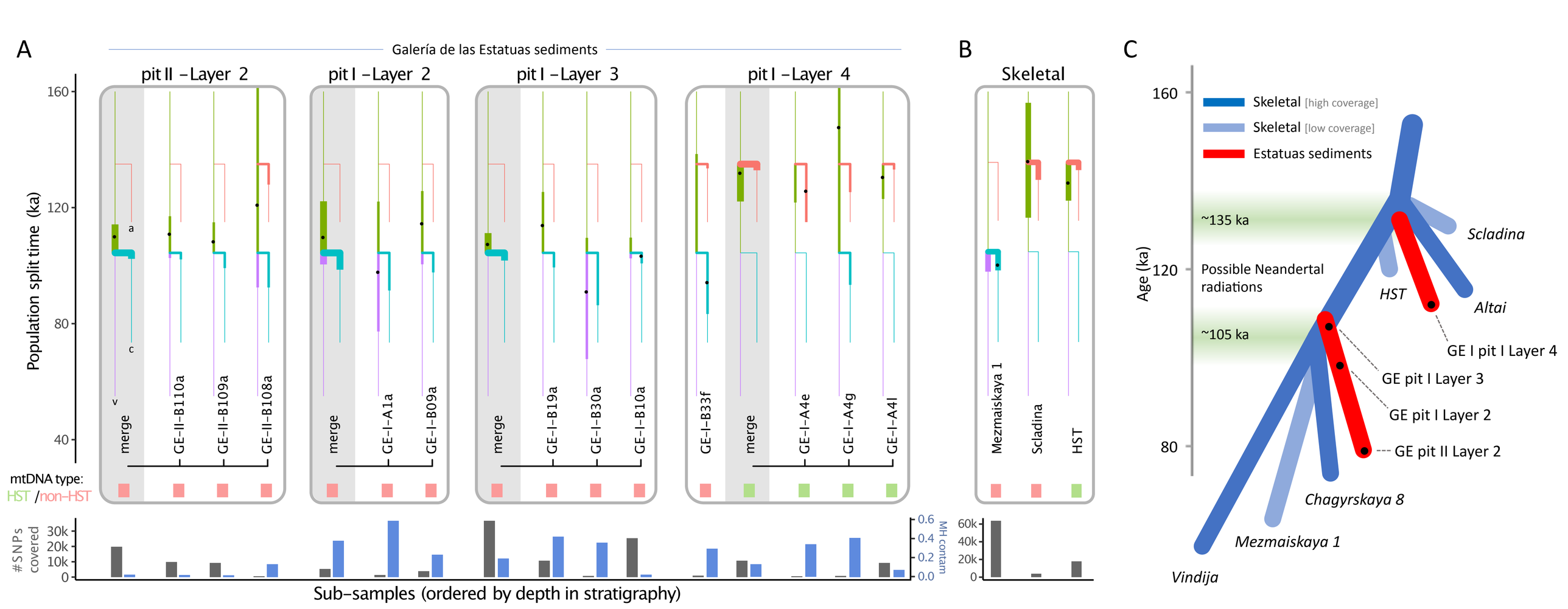
A
Galería de las Estatuas sediments
pit II – Layer 2
pit I – Layer 2
pit I – Layer 3
pit I – Layer 4
Population split time (ka)
160
120
80
40
a
c
merge
GE-II-B110a
GE-II-B109a
GE-II-B108a
merge
GE-I-A1a
GE-I-B09a
merge
GE-I-B19a
GE-I-B30a
GE-I-B10a
GE-I-B33f
merge
GE-I-A4e
GE-I-A4g
GE-I-A4l
mtDNA type:
HST /non-HST
#SNPs covered
30k
20k
10k
0
0.6
0.4
0.2
0.0
MH contam
Sub-samples (ordered by depth in stratigraphy)
B
Skeletal
Mezmaiskaya 1
Scladina
HST
60k
40k
20k
0
C
160
120
80
Age (ka)
Skeletal [high coverage]
Skeletal [low coverage]
Estatuas sediments
~135 ka
Possible Neandertal radiations
~105 ka
Scladina
HST
Altai
GE I pit I Layer 4
GE pit I Layer 3
GE pit I Layer 2
GE pit II Layer 2
Chagyrskaya 8
Mezmaiskaya 1
Vindija

Supplementary Materials for

Unearthing Neandertal population history using nuclear and mitochondrial DNA from cave sediments

Benjamin Vernot,* Elena I. Zavala, Asier Gómez-Olivencia, Zenobia Jacobs, Viviane Slon, Fabrizio Mafessoni, Frédéric Romagné, Alice Pearson, Martin Petr, Nohemi Sala, Adrián Pablos, Arantza Aranburu , José María Bermúdez de Castro, Eudald Carbonell, Bo Li, Maciej T. Krajcarz, Andrey I. Krivoshapkin, Kseniya A. Kolobova, Maxim B. Kozlikin, Michael V. Shunkov, Anatoly P. Derevianko, Bence Viola, Steffi Grote, Elena Essel, David López Herráez, Sarah Nagel, Birgit Nickel, Julia Richter, Anna Schmidt, Benjamin Peter, Janet Kelso, Richard G. Roberts, Juan-Luis Arsuaga, Matthias Meyer*

* correspondence to: benjamin_vernot@eva.mpg.de (B.V.); mmeyer@eva.mpg.de (M.M.)

This PDF file includes:

Materials and Methods
Figures S1 to S26
Tables S1 to S14
References 46-103

Other Supplementary Materials for this manuscript includes the following:

Tables S10 to S14, Excel tables.

Supplemental Text

SI 1: Archaeological context and sediment sampling

Whereas the analysis of nuclear DNA from Denisova Cave sediments relied on previously prepared DNA libraries (*2*), extensive sediment sampling was performed at Chagyrskaya Cave and Galería de las Estatuas.

Chagyrskaya Cave

Detailed background on the stratigraphy, chronology and archaeological assemblages from Chagyrskaya Cave are available elsewhere (*5*). Seventy-three sediment samples were collected from Layers 7, 6, 5, 3 and 2 in the south face of squares И8 and К8 during the 2017 excavations (Fig. 1B, Fig. S1A). Layer 7 is archaeologically sterile, rests directly on bedrock and is only a few cm thick at most at the sampled section. The upper surface of Layer 7 may once have been a living floor, but it has been subjected to post-depositional disturbance by cryoturbation, resulting in the incorporation of sediments from the lower parts of the overlying strata (Subunit 6c). Subunit 6d is the product of such processes, complicating the identification of the contact between Subunit 6c and Layer 7 in some places and resulting in the incorporation of bones and stone artifacts from Subunit 6c, which represents the primary depositional context of the Middle Paleolithic assemblage (*5*). Layers 6 and 5 contain abundant stone and bone artifacts associated with the Middle Paleolithic, as well as the remains of Neandertals and a range of animals and plants (*5*). Layers 3 and 2 accumulated during the Bronze Age. Sediment samples were collected from 10 vertical columns: eight columns (67 samples) transecting the Neandertal-bearing deposits, and two columns (6 samples) through the Bronze Age deposits as a cross-check on potential DNA contamination; no Neandertal DNA was retrieved from the latter samples. Samples were spaced 2–3 cm apart in the lower columns and 3–5 cm apart in the upper columns (Fig. 1B, Fig. S1B–E). After first cleaning the section and donning protective headwear, gloves and a mask, a clean scalpel blade was used to excavate a few grams of sediment at each pre-marked location. To further prevent potential cross-contamination, we sampled from bottom to top in each column. Samples were sealed in individual zip-lock plastic bags and labelled with unique barcodes. The location of each sample relative to site datum was then recorded using a total station (Table S10).

Galería de las Estatuas

Overview

The Sierra de Atapuerca (Burgos, Spain) archaeo-paleontological site complex, located at the north of Spain (Fig. S2), is well known for its Early and Middle Pleistocene paleoanthropological record (*29*, *46–50*). Several Middle Paleolithic sites in Atapuerca have also been described (*11*, *51–54*), but Galería de las Estatuas is the only one which has yielded a Neandertal remain (*12*).

The Galería de las Estatuas (GE or Estatuas) is a Middle Paleolithic site in the upper level of the Cueva Mayor-Cueva del Silo karstic system (Sierra de Atapuerca, Burgos, Spain). GE is

interpreted as an ancient entrance to the cave system, which is currently closed and sealed by a stalagmitic flowstone. In this site, two test pits (Estatuas pit I, or GE-I, and Estatuas pit II, or GE-II) have been excavated from 2008 to present (*11*), separated from each other by approximately 6 m in horizontal distance (Fig. 1C, Fig. S2). Pit II is located in the area closest to the original entrance and somewhat topographically higher than pit I, which is located in a more internal and wider area of the cave. The stratigraphic analysis has revealed the presence of at least five lithostratigraphic units (LU), which have yielded evidence of human occupations with sporadic carnivore activity (*11*, *55*).

In both Estatuas Pit I (GE-I) and Estatuas Pit II (GE-II), a detrital sequence is sealed by a stalagmitic flowstone, varying in thickness depending on location. The stalagmitic crust thickens from Pit I towards the ancient cave entrance (Pit GE-II). The detrital phase beneath is of a clearly allochthonous nature, based on the presence of quartz, feldspar, phyllosilicates and different extraclasts (sandstone, gneiss, and iron oxides) together with dolomite, limestone or speleothem intraclasts (*55*). The ^{14}C, OSL and U-series dating for Galería de las Estatuas (*10*, *11*, *56–59*) are summarized in Table S1. Uranium series dating provides minimum ages for the detritral sequence (Table S2) (*60*, *61*). A series of eight radiocarbon (^{14}C) ages obtained on faunal remains provided minimum ages older than 45 ka cal BP for the Middle Paleolithic layers (*11*). More recently, the Middle Paleolithic levels have provided older datings (from ~70 ka to 113 ka ago) using single-grain optically stimulated luminescence (OSL), which places the sequence at the end of MIS5 and the beginning of MIS4 (*10*).

The different LUs have yielded lithic tools of clear Middle Paleolithic affinity, as well as ungulate and carnivore fossil remains dominated by equids and cervids (*11*). A single Neandertal bone has been found in square L-31 in the interface between LU3 and LU4 with a chronology of c. 110 ka (Table S1): a distal foot phalanx (*12*) (Fig. S3).

For an initial DNA analysis, a set of 9 bulk samples was taken from both pits of Galería de las Estatuas, 5 from pit I (**GE-I-A1 to 5**) and 4 from pit II (**GE-II-A6 to 9**). These samples were collected into ziplock bags using a trowel that was carefully cleaned from sediment in-between samplings and stored in the fridge until sub-samples were removed for ancient DNA extraction. In Estatuas Pit I (GE-I), for 4 out of the 5 samples, sampling was performed besides (n=2) or in close proximity (n=2) to the locations from which samples had been previously removed for OSL dating (*10*) (Figs. S4 and S5).

Galería de las Estatuas-Pit I

In Estatuas Pit I (GE-I), a first pit reached a depth of *ca.* 2 m. The excavation surface was then enlarged, resulting in an uneven floor for this pit. This detrital sequence overlies an ancient flowstone that also occupies the east wall of the cave (*55*). The chronology of this flowstone appears to correspond to the Matuyama Chron, but falls before 1.22 Ma (*62*). Information is lacking as to what happened between the deposition of the Matuyama age flowstone and the start of the detrital sequence.

From top to bottom, the geological sequence at the excavation zone starts with a stalagmitic flowstone, varying in depth between 12 and 20 cm depending on location (*55*). Within this flowstone type speleothem, some ash-rich layers and charcoal fragments have been found, corresponding to Neolithic and Bronze age human activity (*56*). Furthermore, a fine sediment layer remains, which contains some pottery fragments and is embedded inside the base of the stalagmites in certain areas of the site, also attributed to these same chronologies.

The detrital sequence underneath the flowstone has been divided into five lithostratigraphic units (LUs), of which LU5 is the oldest and LU1 the most recent. The main sedimentological differences are related to the texture, size, morphology and abundance of the framework clasts, matrix abundance and matrix composition (quartz, potassium feldspar and plagioclase, and phyllosilicates).

LU1 is composed of orange clays with fine quartz sand (40%) and centimetric oblate fragments of dolomite. At LU1 there are abundant nodules and laminar millimetric levels of micritic calcite (due to precipitation by water infiltration), which provide a whitish color to the stratigraphic level, laterally variable. A single grain OSL dating has provided an age of 80,000 ± 5,000 BP (GE16-2; (*10*)).

LU2 is composed of black clays with silty orange sublevels and has abundant clasts, the size of which decreases towards the top of the level. LU2 is a very inhomogeneous stratigraphic level with variations both in color (black to reddish) and in the proportion of gravel and pebbles, with respect to the clay loam. Very angular planar or slabby clasts with triangular shapes, edges and faces unworn, and homometric (3-5 cm) in size predominate in LU2. They are reminiscent of the gravity flow type rock fragments that form the scree, in this case remobilized by more or less dense mud flow toward the cavity. Equant cobbles, 10-15 cm in size, and subrounded by granular disintegration are also present. The predominant lithology of the rock fragments (98%) is dolomite/limestone. The matrix has around 50% quartz, silt-fine sand in size. The percentage of calcite present in the level varies with the texture, predominating in the most washed facies (65%) due to infiltration water (the calcite is cemented into the faces of the clasts) and being less prevalent in the matrix-rich facies (16%). Two single-grain OSL dates have been performed in this level. On the uppermost part, darker in colour, it has yielded 83,000 ± 5,000 BP (GE16-1; ref. (*10*)). On the lowermost part, orange in colour, it has yielded 113,000 ± 8,000 BP (GE16-3; ref. (*10*)), which is statistically indistinguishable from the dates obtained in LU3 and LU4.

LU3 is composed of orangish silty clays, which are browner towards the base. It is matrix-supported and the clasts are oblong (or elongate) at the base and more equant at the top. The faces of the clast, mainly of dolomite (97%) are unworn, and the edges worn. The texture of LU3 is mainly matrix-supported. Within LU3 there are two sub-levels. At the base, angular pebbles/cobbles with equant and elongated shapes predominate. Some of the elongated clasts show a vertical orientation/disposition, probably due to the gravitational (debris) flow thrust on the clasts. In the upper part, however, pebbles can be distinguished with clast-supported texture and open-work, with positive size-decreasing sequences. The clasts are mainly subrounded, with edges and faces worn but clearly distinguishable. This increase in particle roundness could be related to alteration due to weathering rather than transport, and be caused by granular disintegration of the dolomite, particularly in particle edges. Single grain OSL dating of this level has provided an age of 107,000 ± 8,000 BP (GE16-4; ref. (*10*)).

LU4 is composed of a matrix of dark silty-clays, with decimetric, oblate and equant-shaped fragments of flowstone-type speleothem (12%) and dolomite/limestone (80%), which are very heterometric in size (pebbles-boulders). The face and edges are unworn. They are to a greater or lesser extent enclosed in the matrix (matrix-supported). The matrix is composed of quartz silts and phyllosilicates (30% and 30%), the main type being illite. Calcite is also present as cement (40%). A single grain OSL dating of this level has provided an age of 112,000 ± 7,000 BP (GE16-5; ref. (*10*)).

Finally, LU5 was first described as composed of a pink(ish) carbonate (76-91% calcite) silty fraction with no clasts. The description of LU5 suggests very degraded flowstone, probably

related to the flowstone corresponding to the Matuyama Chron. In the NE of GE-I we have revealed a larger surface of this level composed by silty fraction with flowstone clasts which are recovered by a carbonatic regrowth. Some (scarce) faunal remains have been found in this level, also generally covered by a carbonate layer and some of them are vertically oriented.

Additional DNA samples from Estatuas pit I (GE-I) were taken from two complementary profiles: from the western profiles of the original pit (square M30; LU4 and LU5; samples: GE-I-B34 to B48) and from the current western profile (square: L31; from the speleothem to the contact between LU3-LU4; samples: GE-I-B01 to B33) (Fig. S4). Except for the OSL sample GE-16-1, located c. 50 cm from the sampling area, the DNA sampling area is coincident with the OSL sampling area. Sampling was performed using 5-ml screw cap tubes with a diameter of ~13 mm that were pushed into the sediment while rotating the tube in a drill-like manner. Prior to sampling, a thin layer of surface material (~ 5mm) was cut or scraped off using disposable scalpels. Samples were taken in multiple columns every few centimeters. This sampling strategy yielded a few grams of sediment per tube, although much smaller amounts (< 0.1 gram) were obtained from a few spots with particularly hard material (e.g. speleothems). Sampling locations were then labeled with pins or used scalpels, their precise location recorded using a total station (Table S10), and the samples stored in the fridge.

Stratigraphic integrity of Estatuas Pit I:

Arsuaga *et al.* 2017 (*11*) found no evidence of bioturbation at Galería de las Estatuas. Evidence against bioturbation includes clear differences in terms of color, lithology and the matrix composition between the different layers (Table 1 of (*11*)). Additionally, there are differences in flora, as derived from pollen, between LU3 and LU4 (Figure 4 of (*11*)): there is an increase of mesophilous and arboreal taxa and a decrease in the steppic taxa from LU3 to LU4. Most significantly, taxa such as *Brassicaceae*, *Spergula* and *Papaveracea* were found in LU3, but were absent in LU4, suggesting that movement of sediments between the layers was not appreciable. Due to these differences in the flora, LU4 was interpreted as a less dry period with more abundant tree pollen than LU3.

Additional evidence against bioturbation and leaching of DNA can be derived from genetic analyses. First, the mtDNA signals are quite different between LU3 and LU4, and are not compatible with mixing of sediments or translocation of DNA between the two layers (SI 5). Second, the richest sediment samples in terms of hominin DNA content were found in isolated samples scattered throughout all layers (Tables S10and S12), indicating a highly non-uniform distribution of hominin DNA. In contrast, if this DNA were instead distributed via leaching, one might expect a more uniform distribution, with larger amounts of DNA in upper layers, followed by steadily decreasing amounts of DNA as a function of distance to the initial deposit.

Finally, a previous single-grain OSL study (*10*) found no evidence of post-depositional mixing between pit I / Layers 2, 3 and 4, on the basis of low scatter, no significant positive skew, and "overdispersion values … in agreement at 2σ with what is typically observed for well-bleached samples." (*10*)

Galería de las Estatuas-Pit II

In Estatuas Pit II (GE-II), the excavation has reached a depth of c. 1.5 m and there are differences in the geochemical composition from that of Estatuas Pit I (GE-I; (*11*)), which might

be due to the location of this sector (it is closer to the cave entrance, as also evidenced by the abundance of plant roots in this sector of the cave), and/or to potential chronological differences between these two sectors. The base of the flowstone speleothem has yielded an age of 53,774±3,447 by U/Th, which is older than the date obtained in Estatuas I.

The detrital sequence of GE-II has been divided into three LUs, the uppermost of which is further subdivided into two sublevels. LU1a from Estatuas Pit II (GE-II) is composed of light sands of quartz with subhorizontal, whitish, altered limestone clasts while LU1b is composed of orange silty-clays (around 50% of quartz and 25% of clay minerals) with decimetric equant isolated clasts. The percentage of calcite in the matrix is around 25%. A single grain OSL dating of this level has provided an age of 70,000 ± 5,000 BP (GE16-6; ref. (*10*)).

LU2 is composed of dark silty clay, with abundant quartz (40-60%), with decimetric, abundant, angular-edged clasts of speleothem fragments and dolomite. A single grain OSL dating has provided an age of 79,000 ± 5,000 BP (GE16-7; ref. (*10*)). We have recently started to reveal a new LU (LU3), darker in color, which has yet to be properly assessed. The matrix contains less quartz and calcite (34% and 13%, respectively), and yet is richer phyllosilicates (more than 50%). This level was not sampled for ancient DNA.

The OSL samples were taken in the southern profile in 2016. The 4 bulk samples were taken in the mid-part of the pit, in opposite profiles: 2 in the western profile of D33 and 2 in the eastern profile of E33 (Fig. S5). As the excavation continued we realized that the northern and north-western profiles provided a better spot for **further DNA sampling** (Fig. S5), due to the presence of a longer stratigraphic sequence. We currently cannot rule out older chronologies for the deepest samples from Estatuas pit II. Samples for DNA analysis were collected using the same strategy as for pit I.

SI 2: DNA extraction and library preparation

DNA was extracted using a silica-based DNA extraction method described elsewhere (*14*), starting from sub-samples of between 21 to 128 mg sediment that were removed using sterile disposable spatulas. Briefly, one milliliter of lysis buffer 'D' was added to each subsample (or 2 ml to subsamples larger than 100 mg) and the sample suspension incubated overnight with rotation at 37°C. Residual solid components were pelleted in a centrifuge and the supernatant (the 'lysate') transferred to a fresh tube. DNA was purified from the lysates using either silica spin-columns or an automated version of the protocol based on silica-coated magnetic beads (*14*). In the manual procedure, DNA was extracted from the entire lysate, resulting in a final volume of 50 µl. In the automated procedure, lysate aliquots of 150 µl were used for DNA extraction in 96-well format using the Bravo NGS workstation B (Agilent Technologies), yielding DNA extracts with a volume of 30 µl.

Single-stranded DNA libraries were prepared in 48- or 96-well format on a Bravo NGS workstation B as described elsewhere (*15*), using either 10 µl of manually extracted DNA (corresponding to 20% of the lysate) or the whole volume of DNA extract obtained from automated extraction (corresponding to 15% of the lysate) as input. No treatment with uracil-DNA-glycosylase was performed to retain the full signal of cytosine to thymine substitutions in sequencing, which result from the deamination of cytosine to uracil in ancient DNA (*63*). Following library preparation, the yield of library molecules was determined by quantitative PCR (*15*, *64*), and the libraries amplified and tagged with pairs of sample-specific indices (*15*, *65*).

Several extraction and library preparation negative controls, containing no sample material or water instead of DNA extract, were included in each set of experiments and carried alongside the further steps of sample preparation and sequencing. For some samples, multiple DNA extracts and libraries were prepared, using either additional aliquots of the same lysate (representing libraries from the same sub-sample) or aliquots of different lysates (representing libraries from independent sub-samples). All lysates and libraries prepared in this study are listed in Table S10.

SI 3: Initial assessment of mammalian mtDNA preservation in the Galería de las Estatuas sediments

In contrast to Denisova and Chagyrskaya Cave, where the retrieval of ancient mammalian and hominin DNA from sediments was previously demonstrated (*2*), the state of DNA preservation was unknown in the sediments from Galería de las Estatuas. We therefore screened libraries from nine samples that had been collected first (and their corresponding extraction and library negative controls) for the presence of ancient mammalian mtDNA using two successive rounds of automated on-bead hybridization capture (*2*) with probes encompassing the mtDNA genomes of 242 mammalian species (*33*). The enriched sample and control libraries were then pooled with libraries from other projects and sequenced on a MiSeq (Illumina) in 2x 75 cycles paired-end mode with two index reads.

After base calling using Illumina's Bustard software, demultiplexing was performed requiring perfect matches to the expected index combination. Overlapping-paired end reads were merged into full-length molecule sequences using leeHom (*66*). Reads that could not be merged and sequences shorter than 35bp were discarded. The sequences were then assigned to mammalian families using an analysis pipeline described earlier (*2*). Briefly, the sequences were aligned to a concatenated genome sequence comprised of the 242 mammalian mtDNA genomes used to generate the capture probes, using BWA (*67*) with parameters adapted to ancient DNA (*8*). Unmapped sequences and those shorter than 35bp were discarded. To remove PCR duplicates while mitigating the effect of spurious sequencing errors, identical sequences were collapsed using bam-rmdup (https://github.com/mpieva/biohazard-tools), and only sequences seen at least twice were retained. The remaining sequences were then compared to a non-redundant dataset of mammalian mtDNA genomes (RefSeq database of NCBI (*68*)) using BLAST (*69*), the results of which were parsed through the Lowest Common Ancestor algorithm of MEGAN for taxon identification (*70*). Deviating from the strategy described in Slon et al., 2017 (*2*), for each mammalian family identified, relevant sequences were aligned to all reference mtDNA genomes pertaining to that family, using BWA as above. The alignment yielding the highest number of mapped sequences after filtering for mapping quality of at least 25 was retained for further analysis.

Taxa were identified as ancient if: (i) the fragments sequenced presented significant evidence for cytosine deamination (significantly more than 10% cytosine to thymine (C-to-T) changes compared to the chosen reference genome on both ends of the sequenced fragments, as determined based on the 95% binomial confidence intervals computed for these changes); (ii) the sequences assigned to the taxon constituted at least 1% of identifiable sequences; and (iii) the sequences covered at least 105 bases of the reference genome. The latter filter was implemented to further verify the assignation of sequences to a taxon, as the DNA fragments retrieved are expected to be distributed randomly across the correct reference genome rather than map to a restricted part of it.

All nine samples tested presented evidence for ancient DNA preservation, with between 88 and 11,286 sequences assigned to one of seven mammalian families. All samples contained sequences originating from Bovidae, Cervidae, Equidae and Hyaenidae mitochondrial genomes. One sample from GE-I and one sample from GE-II also contained Leporidae mtDNA, as well as Ursidae mtDNA in the former and Suidae mtDNA in the latter sample (Table S11, Fig. S6). We

note that none of the five negative controls contained DNA assigned to any of these families, and no ancient DNA in general (Table S11).

Encouraged by these results, we further enriched the libraries for hominin DNA and found evidence for the preservation of Neanderthal DNA in 7 out of the 9 samples (see next section for details), motivating the second, in-depth sampling of sediments at Galería de las Estatuas described in SI 1.

SI 4: Enrichment and analysis of hominin mtDNA

4.1 Hominin mtDNA enrichment and raw data processing

All libraries prepared in this study were enriched for hominin mtDNA in two successive rounds of on-bead hybridization capture (*71*) using an automated protocol described earlier (*2*) and a probe-set designed based on the revised Cambridge Reference Sequence of the human mitochondrial genome (rCRS (*72*)) in 1 bp tiling. Enriched libraries were pooled and sequenced on Illumina's MiSeq or HiSeq2500 sequencers in 2x 75 cycles or 2x 76 cycles paired-end mode with two index reads. The resulting reads were demultiplexed, overlap-merged and filtered for a minimum length of 35 bp as described in SI 3 above. All remaining sequences were mapped to the rCRS using BWA (*67*) with parameters adjusted for the mapping of ancient DNA (*8*) and unmapped sequences discarded. Bam-rmdup was used to identify sequences originating from the same molecule based on their identical alignment start and end coordinates and to collapse them into single sequences by consensus calling. Hominid mtDNA sequences were distinguished from other mammalian sequences using BLAST and MEGAN and their ancient origin tested exactly as described in SI 3. Summary statistics of sequencing and the identification of hominin sequences are provided in Table S10. We note that 47 negative controls were processed in an identical manner, and that none of these contained ancient hominin DNA (Table S10).

4.2 Assignment to hominin mtDNA lineages

To enable a rough phylogenetic placement of the hominin sequences recovered from each library and to estimate the proportion of present-day human contamination, we used a set of previously published 'diagnostic' positions in the human mtDNA genome (*3*) to determine the support for the modern human, Neandertal and Denisova branches. We performed this analysis twice, using all mtDNA fragments overlapping diagnostic positions and only those showing evidence for deamination at the first or last position. We then accepted a branch support of significantly more than 10% (based on 95% binomial confidence intervals) as evidence for the presence of mtDNA from one of the three hominin groups (Table S10).

As expected, none of the 369 libraries from the Chagyrskaya Cave and Galería de las Estatuas sediments showed significant support for the Denisova branch. Of the 223 libraries that showed evidence for the presence of ancient hominin DNA, 203 showed significant support for the Neandertal branch when using all fragments or deaminated fragments only. Of the remaining 20, one library (A16087), from Estatuas pit I Layer 4, showed support for the modern human branch in the fraction of deaminated sequences (three out of four putatively deaminated sequences supporting the modern human state). This is unexpected, as present-day human contamination should in principle be depleted by the deamination filter. However, a visual inspection of the three human-like sequences revealed that the terminal C-to-T substitutions were flanked by several additional substitutions in two of the three cases, indicating that sequence error or divergence to the reference genome led to their erroneous identification as deaminated sequences. When considering all mtDNA fragments, 150 of the 369 libraries from Chagyrskaya and Estatuas sediments yielded significant support for the modern human branch, pointing to the presence of human contamination. Based on these results we conclude that Neandertal mtDNA is

the only ancient hominin DNA that was detected at both sites, and that present-day human contamination is present in many libraries and has to be accounted for in down-stream analyses.

4.3 Reconstructing mtDNA consensus sequences

To determine if some of the libraries are suitable for reconstructing complete mitochondrial genome sequences and performing in-depth phylogenetic analyses, we attempted consensus calling for all libraries from Galería de las Estatuas and Chagyrskaya Cave that yielded more than 6,000 unique hominin mtDNA fragments (corresponding to more than ~ 17-fold coverage of the mitochondrial genome) and point estimates of human contamination lower than 10% (see Table S10). If more than one library that was produced from the same DNA extract or lysate fulfilled these criteria, i.e. if libraries did not originate from independent sub-samples of sediments, only the library with the highest mtDNA coverage was analyzed. These criteria left us with 9 libraries from Galería de las Estatuas and 5 libraries from Chagyrskaya Cave for further analysis. In addition, we reprocessed published mtDNA sequence data from a library from a Denisova Cave sediment sample (D5276, published in ref. (*2*)), for which nuclear capture data was generated in the present study. The sequences in this library had been shown to represent a single mitochondrial genome sequence, presumably from a single Neandertal individual.

In order to minimize the loss of sequences that may occur in mapping due to sequence divergence between Neandertal and modern human mtDNA, we first re-aligned all sequences that were generated from these libraries to either the Hohlenstein Stadl (*HST*) mtDNA (Genbank acc. no. KY751400.2) genome or the mtDNA genome of Vindija 33.19 (Genbank acc. no. KJ533545), which represents the 'classical' Neandertal mtDNA in this analysis. The reference genome was chosen according to the results of the kallisto analysis (see SI 5) and mapping performed using BWA with 'ancient parameters' as described in SI 2. PCR duplicates were removed, sequences filtered and assigned to Hominidae as described earlier (see SI 3). In order to call a consensus base, we then required a position to be covered by at least 5 unique fragments and at least 75% of fragments to agree on a single base. To mitigate the influence of deamination, T's were disregarded during consensus calling if they were present in the first and last three positions of a sequenced fragment.

Using this approach, the number of missing positions due to low coverage ranged between 136 and 1,784 in the mtDNA consensus sequences generated from the 14 Galería de las Estatuas and Chagyrskaya libraries. In addition, there were between 4 and 53 positions where the coverage was high enough but no consensus call was made due to insufficient support of a single base. These positions may reflect true sequence diversity in the mtDNA fragments, which will often originate from more than one individual (*2*). However, there are other factors that may also contribute to the presence of different bases at the same position of the mtDNA genome: first, since hybridization capture probes carry modern human mtDNA sequence, capture bias may lead to an over-representation of modern human DNA fragments in regions of the mtDNA genome that show above-average sequence divergence between Neandertals and modern humans, such as the D-loop. Second, regions that are highly conserved among the mtDNA genomes of mammals, especially the 12S and 16S rRNA genes, may attract faunal mtDNA fragments that are misclassified as belonging to Hominidae. We therefore disregarded the 12S and 16S rRNA genes, the D-loop, as well as the short tRNA genes in further analyses and focused on the 13 protein-coding genes of the mtDNA genome, which comprise ~11.3 Kbp of sequence. In addition, we visually inspected the sequence alignments at all positions where conflicting bases

were observed, and identified a short stretch of sequence in the ND5 gene (positions 13,452 – 13,495 in the coordinate space of the Vindija 33.19 reference) with an excess of coverage and conflicting bases. We hypothesized that DNA fragments with conflicting bases in this region may have been misclassified as hominin by MEGAN (*16*), and searched for closely related sequences using BLASTN (*69*). The closest matches were consistently from Bovidae, leading us to identify these as misclassified bovid sequences. We manually corrected the consensus sequences at these positions (19 instances in total; Table S3). In addition, we made manual consensus calls at positions where a deamination at the fourth or fifth position from the end of the sequence was the likely cause of a missed call (9 instances in total; Table S3).

In summary, we obtained consensus sequences with 0 or 1 conflicting calls from 3 libraries from Galería de las Estatuas (A16045, A20281 and A16112; see Fig. S7 for coverage plots and consensus support) and one library from Chagyrskaya Cave (A15850). These sequences possibly represent single individuals and are therefore suitable for tree building and estimating the ages of the individuals based on the length of their branches in the phylogenetic tree. Nine additional libraries produced sequences with between 2 and 9 conflicting calls, making it less likely that they contained the mtDNA of single hominin individuals. Among these is library A15858 from Chagyrskaya Cave (with two conflicting calls), whose consensus sequence is identical to the Chagyrskaya Cave consensus sequence A15850 at every position where A15850 has a non-missing base. Due to higher coverage for A15858, we are able to call an additional 836 consensus bases. We therefore use the A15858 consensus sequence in the kallisto analysis presented in SI 5, as that analysis removes bases that are uncalled in any mtDNA genome, and including this larger consensus sequence allows us to use more of the mtDNA genome. Another library, A11423 from Galería de las Estatuas, produced a consensus sequence with 24 conflicting positions, indicating that it represents a composite sequence of relatively divergent mtDNA types. These sequences were therefore omitted from the branch shortening analysis.

4.4 Mitochondrial phylogeny and branch shortening

To place the three sediment samples from Galería de las Estatuas and the sample from Chagyrskaya Cave from which high-quality consensus sequences could be obtained in the context of previously published mtDNA genomes, we constructed phylogenetic trees using BEAST2 (17) and estimated the molecular date for each sample based on the length of its branch in the tree. We also included in this analysis the Neandertal mtDNA genome reconstructed from a previously published sediment sample from Layer 14.3 of the East Chamber of Denisova Cave (library D5276) (2).

The five sediment mtDNA sequences were combined into a multiple sequence alignment with the mtDNA genomes of 54 modern humans (*73*) and 10 ancient modern humans (*74*), all published Neandertal (n=25) and Denisovan (n=4) mtDNA genomes and a chimpanzee mtDNA genome (*75*) using mafft (*76*) and the 11.3 kb of the protein-coding genes were extracted and used for analysis. In order to identify the best fitting clock and tree model for the tree we used a path sampling approach from the MODEL_SELECTION package (*77–79*) in BEAST2. For each model test we used 40 path steps, a chain length of 25,000,000 iterations, a parameter alpha of 0.3, a pre-burn-in of 75,000 iterations and an 80% burn-in of the whole chain. A mutation rate 1.57 x 10E-8 was used. For the relaxed log normal and strict clock a normal distribution was used with the mean set to the mutation rate mentioned above and a sigma of 1.-E-10 (*74*). For all models the substitution model Tamura-Nei 1993 (TN93) (*80*) was used. The tree was calibrated

using carbon dates from ancient modern humans and Neandertals where available (*18*, *74*, *81*). Modern samples were set to date = 0. For Neandertals of unknown age, a range of 30,000 to 200,000 years was used, with the exclusion of Sima de los Huesos which was constrained to 200,000 to 780,000 years. For Denisovans 2, 4 and 8 ranges of 30,000 to 300,000 years were used. As used in previous analyses (19), Denisova 3 was restricted to the rage of 30,000 to 100,000 years based on previous analysis on the nuclear genome. For each sample we used a uniform prior over the allowed range of dates. The Neandertals, modern humans, and Denisovans were also constrained to monophyletic groups, enabling us to estimate their respective TMRCAs.

No substantial difference was observed between the different models (Table S4), therefore a strict clock and constant population was used as it is the simplest model. Three MCMC runs of 75,000,000 iterations, with a pre burn-in of 10,000,000 iterations and sampling every 2,000 trees were then performed on each dataset. The log and tree files of the runs for each respective dataset were then merged using logcombiner2 from BEAST2, and the merged tree file was then run through the program treeannotater from BEAST2 in order to summarize the output into a single tree. The resulting tip dates and TMRCA estimates were examined using the program Tracer from BEAST2 (Table S5) and a tree generated using Figtree from BEAST2 (Fig. S8).

We find that the Chagyrskaya sample falls in a clade with the previously published Chagyrskaya mitochondrial genome and the two are estimated to have lived at approximately 85-90 thousand years ago (95% HPDI: 54,986 - 126,590 and 49,627 - 122,190 years ago for the sediment sample and Chagryskaya 8, respectively). The molecular date for the sample from Layer 14.3 of the Main Chamber of Denisova Cave is estimated at 127,560 years ago (95% HPDI: 85,136 - 171,380), which places it at a similar time to the sample from Layer 4, pit I from Galería de las Estatuas (136,150, 95% HPDI: 75,095 - 199,590) as well as the mitochondrial genomes of Hohlenstein-Stadel, Scladina, Altai and Denisova 15. Despite their similar ages, the sediment sample from Denisova Cave falls between the late Neandertals and Altai-like Neandertal, while the Galería de las Estatuas sample groups with Hohlenstein-Stadel. The remaining two Galería de las Estatuas mitochondrial genomes form a clade with Mezmaiskaya 1 and are both dated to ~105,000 years ago (95% HPD: 59,765 - 154,260 and 60,455 - 154,600 for A16045 and A16112 respectively).

SI 5 mtDNA haplotype identification from sparse data using kallisto

Rationale

Many sediment libraries are not suitable for reconstructing consensus sequences, either because they do not contain enough mtDNA fragments, are too contaminated with present-day human DNA, or because they appear to originate from multiple mtDNA sequences. We hypothesized that the mtDNA composition of a library could be inferred using kallisto, a tool that was designed for quantification of mRNA transcripts from RNA-seq reads (*34*), but that has also been applied to metagenomics analyses (*82*).

Given a set of RNA sequencing reads for a sample, kallisto attempts to estimate the particular transcript isoforms which generated those sequencing reads. Specifically, kallisto estimates isoform *abundances*. Due to the existence of multiple isoforms of a transcript, many sequencing reads are ambiguous as to their true origin. That is, a sequencing read may match multiple possible transcripts, even though it must, by definition, originate from only a single transcript. Other sequencing reads may match only a single transcript. Although these may comprise only a small fraction of the total sequencing data, these reads constitute evidence for the presence of one transcript over the others, and thus constitute evidence for the true origin of the ambiguous reads. In this way, even ambiguous reads can be counted towards the abundance of the appropriate transcript. Given a set of sequencing reads, kallisto takes a k-mer based approach to estimating the abundance of every transcript in a panel of reference transcripts.

In many ways, the problem of resolving the mtDNA haplotypes in a sediment library presents similar challenges. Here, rather than isoforms, we have homologous mtDNA haplotypes. Due to sequence conservation and short evolutionary times, many pairs or groups of haplotypes share stretches of identical sequence. Thus, many sequencing reads cannot distinguish between haplotypes. Even when they overlap sites that differ between haplotypes, these sites may still be shared among a group or clade of mtDNA genomes.

However, our application also presents a few unique challenges:

- Given the high levels of sequence similarity between any two mtDNA haplotypes, combined with low amounts of sequence data, it may not be possible to distinguish between closely related haplotypes.

- As opposed to transcript isoforms, mtDNA haplotypes differ by the presence or absence of ancestral and derived alleles. Imagine that we are analyzing DNA from an mtDNA haplotype X that is not well-represented in our set of reference genomes: for example a haplotype that diverged from the *Mezmaiskaya 1* branch after this branch diverged from the rest of the tree (Fig. 2A). Our goal is to identify *Mezmaiskaya 1* as the closest relative of this mtDNA. Because differences between mtDNA genomes are often due to single point mutations, at any site on haplotype X where X lacks a mutation found in *Mezmaiskaya 1*, it shares the ancestral state with many other mtDNA haplotypes. In the kallisto framework, a read that overlaps this site therefore counts as evidence *against* the presence of *Mezmaiskaya 1* DNA,

while any reads overlapping *Mezmaiskaya 1* -specific sites will count as evidence for *Mezmaiskaya 1* DNA. Therefore, unless the sediment haplotype(s) are well-represented in the reference panel, kallisto will likely infer the presence of multiple closely related haplotypes, and may incorrectly prefer haplotypes with ancestral states.

Here, we explore the use of kallisto for identifying mtDNA haplotypes. We simulate ancient DNA reads from mtDNA haplotypes, as described in SI 6, and:

- Investigate the use of kallisto when the full set of reference genomes is known.
- Investigate the use of kallisto when the simulated genome is removed from the reference set.
- Simulate ancestral sequences, and evaluate kallisto performance for more basal sequences.
- Quantify the probability of observing a given kallisto abundance estimate given the true presence or absence of mtDNA from a closely related haplotype.

Evaluating kallisto with simulated ancient mtDNA reads

We first constructed a multiple sequence alignment (MSA) of mtDNA genomes from 25 Neandertals (including Denisova 11), 5 Neandertals from the Estatuas, Chagryskaya and Denisova cave sediments (SI 4), 4 Denisovans, Sima, 54 modern humans and 10 ancient modern humans (described in SI 4). As some mtDNA genomes are more complete than others, which could lead to reads being preferentially assigned to more complete genomes, we removed all columns from the MSA in which any sequence was unresolved (denoted with an N), leaving an MSA with 15256 columns (out of 16604); note that the consensus sequence for Chagyrskaya Cave library A15858 was substituted for A15850, as described in SI 4, due to its larger consensus sequence. We note that this N-removal creates an MSA with some "nonsensical" kmers - that is, by removing N columns, bases that are ordinarily non-adjacent are concatenated together. However, as this creates semi-random kmers, and affects all genomes equally, we expect it has a minor impact on the analysis.

We next simulated (as described below in Simulated Ancient DNA) 5,000 “ancient” DNA reads from each mtDNA genome in the MSA. To eliminate unresolved bases (i.e., N), we inferred ancestral states across the full phylogeny with the software treetime (*83*) and the mtDNA phylogenetic tree (Fig. 2A), and replaced unresolved bases with these ancestral states. We note that these inferred bases are still not included in the kallisto references, and thus should not have a large impact on the analyses – but that we are simulating the full mtDNA, more closely replicating true ancient DNA sequences.

We then estimated mtDNA genome abundance for each simulated dataset of 5000 reads, using kallisto, first using the full set of mtDNA genomes as the set of references – that is, each simulated genome is included in the reference set. We find that abundance estimates are highly accurate, with the correct genome generally receiving ~80-95% of the total estimated abundance (Fig. S9, highest abundance reference(s) indicated with one or more red dots). The only exceptions are when multiple mtDNA genomes are identical, and therefore the abundance is

exactly equally distributed amongst several genomes (e.g., several Goyet Neandertal individuals). In further analysis, we therefore partitioned the tree into a set of 5 "major groups" that are closely related to each other (Fig. 2A, colors; Fig. S9, red boxes). Each of these are either sibling nodes, or diverge from the larger tree at around the same time.

We next considered a more typical situation, where the mtDNA may come from a previously unknown genome. Specifically, we estimated mtDNA genome abundance where, for each simulated dataset, we use a reference set that excludes the simulated genome. In all cases, the top hit(s) come from within the same "major group" (Fig. S10). However, certain mtDNA references may be more challenging to quantify – for example, the consensus sequence from a Chagyrskaya Cave sediment sample (Chag_6c in Fig. S10) often has low levels of abundance when used as a reference, even for simulated data from distantly related genomes (Fig. S10). We note that this is not due to its origin as a sediment sample – if this sequence is removed, *Chagyrskaya 8* shows similar patterns. Additionally, consensus sequences from Estatuas sediment samples do not attract abundance from distantly related sequences (Est_2, Est_3, Est_4, from Estatuas pit II/Layer 2, pit I/Layer 3, and pit I/Layer 4, respectively).

Probabilistic genome assignment with ancestralized mitochondrial genomes

We further investigated the effect of sequence divergence between the sample mtDNA and the most closely related genome in the reference set on our analysis, by simulating DNA from "ancestralized" mtDNA genomes.

We simulated ancestralized genomes at intervals along each internal and tip branch – at 1ky intervals up to 25ky, then 30ky, 40ky, 50ky, 100ky, 150ky, 200ky and 250ky. As described above, we used treetime to identify mutations occurring on each branch of the mtDNA tree. We then reverted a random set of these mutations to the ancestral state, where each mutation is selected with probability equal to the relative position of the simulated mtDNA on the branch. We note that the majority of branches are shorter than 50ky long. For each simulated ancestral genome, we then simulated aDNA reads as described below (Simulated Ancient DNA), and quantified mtDNA abundances using the full set of original (i.e., tip) mtDNA genomes as references. Although we simulated "true" ancestral mtDNA genomes, which would lie directly on the internal branches of the mtDNA tree, we note that additional divergence is simulated in the generation of the aDNA reads (see below) – effectively "evolving" the mtDNA genomes away from the ancestral branch.

For each reference, we then identified abundance thresholds at which it is likely that DNA in the sample actually originates from a closely related mtDNA genome. For example, in Figure S10 we see that it is not uncommon to observe low amounts of DNA abundance assigned to the Chagyrskaya Cave sediment sequence (Chag_6c), even for distantly related genomes – thus, a higher threshold may be required when identifying a sample as containing closely related DNA. When simulating 1000 reads from each ancestralized mtDNA genome, we find that at least 36% of the total abundance from a sample must be assigned to the Chagyrskaya Cave sediment sample before there is a >90% chance that this sample actually contains DNA from a closely related genome. This threshold depends on the number of aDNA reads analyzed – for 250 aDNA reads, the threshold is 62%. The threshold is also different for each reference – for example, *Mezmaiskaya 1* is much less likely to attract spurious abundance: for 90% certainty, we require only 16% or 7% of total abundance to be assigned to *Mezmaiskaya 1* (for 1000 and 250

simulated reads, respectively). Several examples are given in Figure S11. Here, closely related is defined as "on the same branch, or within 50kya distance of the root of the branch".

We calculated these thresholds for 250 and 1000 reads (Fig. S11, upper and lower rows), and for 90, 95 and 99% thresholds (Fig. S11, three dotted red lines, from bottom to top). The red vertical line in Figure S11 is placed at 50ky.

Application of the method to sediment libraries

We then ran kallisto on all sediment samples with >=250 ancient hominin reads (Fig. S12), where the number of ancient hominin reads is calculated as *(1 - modern human contamination) * (number of unique reads)*. The modern human contamination proportion is calculated using diagnostic alleles, as described in SI 4. For each sample we calculated the proportion of non-modern human abundance assigned to each reference, under the assumption that any modern human signal originates from contamination. To convert these proportions into probabilities, we applied the thresholds as calculated above. For samples with 250-999 ancient hominin reads, we conservatively use the 250 read thresholds, for samples with >=1000, we use the 1000 read thresholds. The results are presented in Figure 2B, and described in the main text.

No mtDNA evidence of leaching between upper and lower layers in Galería de las Estatuas

On first glance, the results in Figure 2B may seem to indicate leaching of DNA downward from GE-I Layers 2 and 3 ("upper layers") into GE-I Layers 4 and 5 ("lower layers"), due to the presence of non-*HST*-like mtDNA in both the upper and lower layers, but in smaller amounts in the lower levels. Specifically, throughout the upper layers we find substantial similarity to one or both of the two mtDNA haplotypes derived from samples in those layers (in Figure 2B, "Estatuas II layer 2" and "Estatuas I layer 3"; in Figure S13, "Est_2" and "Est_3"). In the lower layers, we observe primarily *HST*-like assignment, in addition to some assignment to *Mezmaiskaya 1* and *Scladina 1-4A*. Notably, however, with the exception of three sub-samples taken from the very top of Layer 4 (GE-I-B33 c/d/f), in Layer 4 we find no assignment to the specific haplotypes found in the upper layers. As described here, we find that leaching would always be expected to present with some assignment to "Est_2" and "Est_3", and that the absence of these specific haplotypes in the lower layers is incompatible with leaching of DNA downwards from the upper layers. Thus, the signals observed in Layer 4 are likely to represent true mtDNA heterogeneity in that population.

To evaluate more formally whether the observed distribution of hominin mtDNA could have been generated by mixing of sediments, or more specifically by leaching downward of DNA from the upper to lower layers, we artificially mixed sequencing reads from the upper and lower layers. We generated artificial datasets comprised of 1000 mtDNA fragments (40% of all Layer 4 libraries contain at least 1000 Neandertal fragments), where between 0 and 100% of the fragments are taken from an upper layer sample, and the remaining fragments are taken from a lower layer sample. The upper layer samples were either GE-II-B110a (library A16112), GE-II-B108a (library A16110), or GE-I-B10a (library A16045), from GE-II Layer 2 (A16112/ A16110) and GE-I Layer 3 respectively. The lower layer sample was GE-I-A4l (library A24519), from GE-I Layer 4. All but A16110 are exceptionally rich samples with a single mtDNA haplotype (SI 4; Figure 2B red squares), guaranteeing sufficient data to perform adequate resampling of

fragments, and avoiding the presence of non-*HST*-like haplotypes in the Layer 4 sample. A16110 represents a mixture of haplotypes common to the upper layers. Each simulated mixture was performed 10 times, each time randomly sampling fragments from the appropriate library (Figure S13B, individual columns).

In contrast to the patterns observed in the lower layers of Estatuas, where we observe non-*HST*-like signal in different specific haplotypes than in the upper layers (e.g., no signal in the yellow box of Figure S13A in the lower layers), when artificially mixing sequencing data from the upper and lower layers, we consistently observe affinity to the *same* non-*HST*-like mtDNA haplotypes observed in the upper layers (e.g., ample lower layer signal in the yellow box of Figure S13B). These results indicate that if the signal in the lower layers were a product of mixing, we would not expect to see a complete shift in the specific non-*HST*-like haplotypes, suggesting that the signal observed in Layer 4 is unlikely to have been generated by mixing. We do note, however, that the signal in the upper three subsamples of Layer 4 (GE-I-B33 c/d/f) is consistent with mixing between the upper and lower layers, and accordingly we do not consider this to be a "true" signal of e.g. co-existing populations.

Simulated Ancient DNA

For several analyses, we required simulated ancient DNA – either from faunal nuclear genomes, or from hominin mtDNA genomes. Here we describe simulations of 225 million ancient DNA reads from the *Ursus arctos* genome, equivalent to approximately 5x coverage – the same procedure was used to simulate hominin mtDNA.

We used custom python code, available here:
https://zenodo.org/record/4468181 (*43*)

This software simulates ancient DNA reads, given:

- A fasta reference genome
- A read length distribution
- Per-position error/substitution probabilities
- An optional uniform substitution probability

For these simulations, we used the following:

- *U. arctos* reference genome: assembly ASM358476v1, downloaded from RefSeq (accession GCF_003584765.1, RefSeq v95) (*84*, *85*). As this genome contains 6672 scaffolds, many of which are a few hundred bp long, we simulated data only from the first 100 scaffolds. These represent 2.21 gigabases, and 95% of the *U. arctos* genome.
- Read length distribution taken from the *Vindija 33.19* high coverage genome, library A9180 (*26*). We simulated only reads with length >= 35bp; taking only reads at least 35 bp long, the average read length is 51bp.
- Per-position error/substitution probabilities inferred using the genotyping software snpAD for the *Vindija 33.19* high coverage genome (*26*, *86*).

We note that the error/substitution probabilities incorporate all possible base-pair changes, and thus include:

- Sequencing errors.
- Mutational differences between the *Vindija 33.19* genome and the human reference.
- Deamination, aka apparent C to T substitutions.

In this way, we create a set of simulated ancient DNA reads that closely mimic the characteristics of the ancient DNA used to produce the *Vindija 33.19* genome.

SI 6 – Nuclear capture methods and analysis

6a. Identification of high-diversity genomic regions

A primary challenge for analyzing hominin nuclear DNA from sediments is the abundant faunal DNA present in nearly all samples (*2*). In particular, due to homology and conservation, it may be challenging to distinguish between faunal and hominin DNA at many loci (e.g., Fig. 3A). We hypothesized that these challenges could be overcome by targeting regions with high mammalian sequence diversity (e.g., Fig. 3B), and that hominin nuclear DNA could be enriched in these regions via hybridization capture (*2*).

To measure mammalian diversity, we downloaded 15-placental-mammal EPO multiple sequence alignments (MSA) as provided by ENSEMBL (*87*) (15 eutherian mammals EPO, ENSEMBL release 75).

http://feb2014.archive.ensembl.org/info/genome/compara/analyses.html#epo
ftp://ftp.ensembl.org/pub/release-75/emf/ensembl-compara/epo_15_eutherian/

This MSA includes the following six primate species:

1. *Homo sapiens*
2. *Pan troglodytes*
3. *Gorilla gorilla*
4. *Pongo abelii*
5. *Macaca mulatta*
6. *Callithrix jacchus*

And the following nine non-primate species, from three major clades:

Glires:

7. *Oryctolagus cuniculus*
8. *Rattus norvegicus*
9. *Mus musculus*

Ungulates:

10. *Sus scrofa*
11. *Ovis aries*
12. *Bos taurus*
13. *Equus caballus*

Carnivora:

14. *Canis familiaris*
15. *Felis catus*

For every single nucleotide polymorphisms (SNP) of interest (defined in SI 6c), we downloaded an MSA for the 52 base pairs (bp) immediately surrounding the SNP (25bp upstream and 26bp downstream, plus the targeted SNP itself). Not all species are represented in all MSAs – for example because there may not be a homologous region in all genomes. To ensure even phylogenetic coverage, we require that an MSA represent at least one species from each of the three major non-primate clades (Glires, Ungulates, Carnivora). We then calculated the number of bases at which each species' sequence differed from the *Homo sapiens* sequence, and take the minimum such divergence among all nine non-primate species. For example, the minimum divergence for the MSA in Fig. 3A is 0 bp (vs *E. caballus*), and for Fig. 3B is 13 bp (vs *F. catus*). This minimum divergence is referred to as the "diversity" of the region around a particular SNP.

6b.Faunal mapping to high-diversity genomic regions

To explore the possibility that faunal DNA may incorrectly map (i.e. mis-map) to the human genome, we mapped 225 million (m) simulated *U. arctos* reads (SI 5) to the human genome (hg19), using BWA (*67*). BWA parameters were adjusted for ancient DNA ("-n 0.01 –o 2 –l 16500"), to allow for more mismatches and indels and to turn off the seeding (*8*).

We note that 225m DNA fragments is approximately 1% of the estimated number of DNA fragments in a typical sediment library (for libraries in this project, median number of fragments, estimated with qPCR, is 15.8 billion), and thus representative of the amount of faunal DNA in a library with 1% faunal molecules. We observed that approximately 9m out of 225m reads (~4%) map to the human genome (hg19), suggesting that faunal false alignments are common. We next considered how the probability of mapping changed as a function of mammalian diversity (SI 6a). Specifically, we considered faunal reads mapping to ~1.35m SNPs that are informative for archaic population history (*3*, *19*) (lineage informative sites in SI 6c), and where a multiple sequence alignment of mammalian genomes (MSA) was available with coverage across the mammalian phylogeny (see SI 6a).

Encouragingly, false *U. arctos* alignment dramatically decreases at sites of interest as a function of flanking mammalian sequence diversity (Fig. 3C). For example, sites with diversity = 1 are covered on average 2 times, and sites with diversity < 8 are covered on average 0.43 times; in contrast, sites with diversity >= 8 are covered on average 0.009 times – a 48-fold decrease in faunal mis-mapping. Genome-wide, average coverage is 0.0029. In contrast, a library from the 60-70 ky old *Mezmaiskaya 1* Neandertal shows even coverage across faunal diversity, indicating that this effect is specific to faunal DNA (library R5661 from (*26*); Fig. 3C). We therefore restrict our capture set and analysis to SNPs with diversity >= 8 (SI 6c).

We note that sites with diversity = 0 do not follow this general pattern, and have lower average coverage than sites with diversity = 1. These regions, with seemingly no divergence over tens of millions of years of mammalian evolution, may be enriched for artifacts, or may represent super-conserved elements. Additionally, the requirement of having at least one species from all three non-primate clades in the MSA may be too restrictive: we observe similar patterns when requiring data from two out of three clades, which might point to the possibility of larger future array designs.

6c. Probe-set design

We designed a probe-set (internally named ssAA197-200) targeting 1.6 million informative single nucleotide polymorphisms (SNPs) in the nuclear genome, restricting our design to SNPs in regions of high mammalian diversity (SI 6a).

Specifically, we selected SNPs with diversity >= 8, that is, where the minimum divergence between *H. sapiens* and any of nine non-primate mammalian species is 8 or larger (SI 6b). SNPs in this category have a 48-fold decrease in faunal mis-mapping, vs SNPs with diversity less than 8 (SI 6b). Additionally, we required:

a) each SNP to be within previously defined "manifesto" regions - those regions where genotypes in three high-coverage archaic genomes are deemed accurate (*26*)

b) the 50bp up and downstream of the SNP to be devoid of simple repeat elements, as defined by the UCSC simpleRepeats table (*88*, *89*).

c) each SNP to be biallelic in the following genomes: hg19, Altai Neandertal, *Vindija 33.19*, *Denisova 3*, pantro4, panpan1.1, gorgor3, ponabe2, rhemac3. An uncalled or deleted SNP does not count as a separate allelic state. For each site, the ancestral allele was set to the allele in pantro4. Primate states were taken from (*26*). Briefly: Whole genome alignments to the human reference genome (hg19) were obtained from the UCSC genome browser for the chimpanzee, gorilla, orangutan and rhesus macaque genomes (*90*). Alignments to the bonobo genome are described in (*26*). Table of all primate states is available here:

https://dx.doi.org/10.17617/3.5h (*45*)

We next collected categories of SNPs that would be informative for various types of analyses, and applied the above filters to these categories.

SNP categories:

1. **Lineage informative sites** (447,172 sites): SNPs that are polymorphic in the Altai Neandertal (*Denisova 5*), *Vindija 33.19*, *Denisova 3* and one modern human, when selecting a single allele at random from each individual. Methodology as described in (*19*), with the exception that here the modern human individual is Mbuti individual SS6004471 from Table S4.1 in (*7*). Note that only transversion polymorphisms are included in this set – the remaining categories include transitions unless noted.
2. **"1240k"** (411,492 sites): Generally used for investigating population histories in modern humans. Described as Panels 1 and 2 in (*91*). Consists of: "all SNPs on the Human Origins array, all SNPs on the Illumina 610-Quad array, all SNPs on the Affymetrix 50k array, and smaller numbers of SNPs chosen for other purposes." (*91*)
3. **Big Yoruba** (328,825 sites): Transversion heterozygotes from two Yoruban individuals: panel 3 in (*91*).
4. **Archaic admixture array** (276,284 sites): SNP panel 4 in (*92*)
5. **Archaic heterozygotes** (351,733 sites): All heterozygotes in three archaic individuals with high-coverage genomes (Altai Neandertal (*Denisova 5*), *Vindija 33.19*, *Denisova 3*).

6. **Hominin diagnostic sites** (494,696 sites): To allow estimation of the extent of faunal mis-alignment, we included SNPs which are fixed-derived in hominins, chimpanzee and bonobo (Fig. 2D, SI 6d).

As might be expected, there is substantial overlap between these categories of sites, such that altogether they represent 1,563,323 sites.

We then constructed a probe-set (ssAA197-200 in Table S12) with the following design: two probes targeting each SNP: one probe containing the derived allele at the targeted site, and the other containing the ancestral allele. Each probe was 52bp long (25bp upstream of the SNP, the SNP itself, and 26bp downstream). We added 8bp adapter sequence, ordered these probes on 1 million feature arrays (Agilent Technologies), and converted them into probe libraries as described elsewhere (*32*).

Supplementary probe-set

We designed a second probe-set (ssAA211 in Table S12) targeting a similar set of 377k SNPs in the nuclear genome. The main advantage of this array is that we include the new high coverage *Chagyrskaya 8* Neandertal genome in defining sites that are polymorphic in archaic humans (*9*). This increases from three to four the number of archaic individuals used. A subset of libraries were additionally captured on this second array; for these libraries, data from both captures were merged [Tables S12, S13].

To define the set of SNPs targeted by the array we ascertained biallelic transversions in the Manifesto-filtered regions of the high coverage genome sequences of three Neandertals (the 'Altai Neandertal' *Denisova 5*, *Vindija 33.19*, and *Chagyrskaya 8*) and one Denisovan (*Denisova 3*), and in 504 individuals from African populations included in the 1000 Genomes Phase 3 dataset (99 Esan in Nigeria (ESN), 113 Gambian in Western Division (GWD), 99 Luhya in Webuye, Kenya (LWK), 85 Mende in Sierra Leone (MSL) and 108 Yoruba in Ibadan, Nigeria (YRI) (*93*)). We used the chimpanzee genome (panTro4) to determine the ancestral state.

We selected SNPs in two approximately equally represented categories:

1. Variation in present-day African populations:
    a. SNPs with derived allele frequency > 10%
    b. SNPs uniformly sampled in 2%-frequency-bins

2. Variation in archaic humans:
    a. Sites that are variable in any of the four archaic genomes
    b. Fixed differences between the archaic genomes and the 504 African genomes
    c. Sites that are fixed for the derived allele in the four archaic genomes, but where the derived allele is present at a frequency less than 1 in the 504 African genomes.
    d. Hominin diagnostic sites, as described above.

All SNPs were required to be in 52bp genomic regions that are uniquely mappable with 35 bp reads (*7*), have a unique alignment to panTro4, and do not lie within regions defined as repetitive by RepeatMasker (*94*) or TandemRepeat Finder (*88*).

We then filtered this set of sites for faunal diversity, designed and ordered probes, and constructed libraries as described above, yielding 377k total sites.

6d.Hominin diagnostic sites

To allow estimation of the extent of faunal mis-alignment, we ascertained SNPs which are fixed-derived in hominins and chimpanzees (Fig. 2D), and ancestral in some set of additional primates. At these sites, ancestral alleles should overwhelmingly indicate faunal mis-alignment, whereas reads originating from a hominin individual should contain the derived allele.

Specifically, we selected sites where all 1000 genomes individuals, hg19, three archaic individuals (Altai Neandertal [*Denisova 5*], *Vindija 33.19*, *Denisova 3*), pantro4, and panpan1.1 all share an allele. The ancestral state was set to the state in ponabe2 and rhemac3, which are required to share an allele. gorgor3 is allowed to carry either allele. Primate states were determined as described in SI 6c.

To test the behavior of these sites for identifying faunal mis-mapping, we counted derived and ancestral alleles at these sites in two datasets: 30m reads sampled from the *Mezmaiskaya 1* library R5661 (*26*), and 225m simulated ancient *U. arctos* reads (SI 5).

At these hominin diagnostic sites, we observed the ancestral allele in 0.2% of aligned reads for *Mezmaiskaya 1*, and in 95.3% of aligned reads for *U. arctos* (Fig. 2E). These proportions are calculated considering only reads carrying one of the two expected alleles (ancestral vs derived). We note that, in the *U. arctos* alignment, a large proportion of the aligned reads carry neither of the expected alleles, consistent with mis-mapping and/or multiple substitutions over long periods of evolutionary time. Additionally, the use of a third-allele reference, which ameliorates the effects of reference bias in mapping, is expected to produce higher counts of unexpected alleles (SI 6f).

6e.Metagenomic filtering of nuclear DNA with Kraken

To further reduce the extent of faunal mis-alignment in nuclear sediment DNA, we assigned each read to the NCBI taxonomy using the metagenomics software Kraken (*24*), and restrict our analyses to those reads classified to the primate clade.

We used Kraken version 1.1.1 and the RefSeq database (*85*) release 95 as the source of genomes for the following groups: Archaea (417 genomes), Bacteria (14,379), Fungi (288), Invertebrate (191), Plant (118), Plasmid (1507), Protozoa (88), Vertebrates mammalians (129) vertebrate other (171) and Viral (9,267). [https://ftp.ncbi.nlm.nih.gov/genomes/refseq/]. We filtered these genomes to those labeled ‘reference genome’ or ‘representative genome’, totaling 14,002,088 contigs for 12,604 unique taxa.

Each of the sequences have then been masked for low complexity using dustmasker (*95*) as per the recommended use of Kraken.

We generated a Kraken database using those sequences, with a k-mer of size 20 (small enough that short ancient DNA reads will have several k-mers). The resulting database, totaling

~1.5TB, was then loaded onto the memory of a machine powered with 2TB of RAM in order improve Kraken's running time.

Each read is assigned to the NCBI taxonomy using this database, and reads assigned to the primate clade are taken for further analysis.

6f. Reference bias - third allele reference and kraken

So-called "reference bias" is the enrichment of reads matching the reference allele (vs the alternative allele) when aligning to a reference genome (*96*, *97*). This effect is exacerbated for ancient DNA, where C to T DNA damage "uses up" allowed mis-matches to the reference, particularly on short molecules. In this situation, a read with the reference allele may align, where a read with the alternative allele will be pushed over the threshold allowed for alignment, and be missed. This effect may be even more problematic for sediment DNA, where faunal DNA will often carry the ancestral allele, and thus may be enriched at sites where the reference carries the ancestral allele, and depleted at sites where the reference carries the derived allele. Furthermore, at hominin diagnostic positions (SI 6d), the human reference by definition carries the derived allele. Reference bias would therefore lead to under-alignment of ancestral alleles in particular at these sites, leading to skewed estimates of faunal mis-mapping.

BWA mapping: We therefore map to a modified version of hg19, where at each targeted site, the reference allele is replaced by a third allele that is neither ancestral nor derived. This approach will cause a reduction in the number of reads mapped to targeted sites, but this is because it equalizes the penalty for reads carrying reference or alternative alleles. Reads are considered for analysis only if they carry the ancestral or derived alleles.

Kraken: In addition, reference bias may confound k-mer based metagenomic analyses such as Kraken, which attempt to assign individual reads to branches on the NCBI taxonomy (*24*) (SI 6e). Here, reads with the ancestral allele may be more likely to be placed in ancestral positions in the NCBI taxonomy, and reads with derived alleles may be more likely to be placed in more recent branches. When assigning reads to the NCBI phylogeny in Kraken, we therefore mask the target base in each read, converting it to an N. This leads to a slight reduction in the number of reads assigned to Order Primates (approximately 10%). Out of an abundance of caution, we also add a second human reference genome to the NCBI taxonomy, where at every targeted SNP, we replace the reference allele with the alternative allele. In this way, kmers with both the derived and ancestral alleles are equally represented in the hominin portion of the NCBI taxonomy.

6g. Nuclear capture summary

We selected a subset of 149 libraries for nuclear capture. In general, we prioritized libraries with larger amounts of ancient hominin mtDNA, although in some instances we selected libraries with low amounts of mtDNA in an attempt to maximize data representation across layers. Two rounds of in-solution hybridization capture were performed using a protocol described elsewhere (*32*), and the enriched libraries pooled and sequenced using Illumina's HiSeq 2500 platform in 2x 75 cycles paired end mode with 2x 7 cycles index reads (*65*). We note that 13 negative controls were processed in an identical manner, and that none of these contained ancient DNA (Table S13).

We then performed the following processing steps for each sequencing run of each captured library (each step corresponds to a column in Table S12):

1. **Split:** We split each sequencing run into separate bams, one for each library, requiring exact sequence matching of both indices.
2. **Mapped:** These split bams were then mapped to a modified version of hg19/GRCH37, where each SNP targeted in the capture array was replaced by a "third" base - i.e., a randomly selected base excluding the expected ancestral and derived alleles. See SI 6f.
3. **Target:** We then restricted to reads overlapping the targeted sites.
4. **uniqueL35MQ25:** We restricted to reads with length >=35bp and mapping quality >= 25, and removed PCR duplicates using bam-rmdup (https://github.com/mpieva/biohazard-tools).
5. **dupRate:** The average number of times a read was observed (high rates indicate libraries that have likely been sequenced to exhaustion).

We then merged all captures and sequencing runs for a given library, if more than one was produced, and performed the following steps / computed the following statistics (each point corresponds to a column in Table S13:

1. **Merged captures:** Merge all captures and sequencing runs for a given library, if more than one exists, and again remove PCR duplicates.
2. **QC / coverage filter:**
    a. Coverage: due to the low coverage in sediment samples, it is unlikely that the same site will be covered by many reads. We therefore remove sites with >4 unique reads mapping in any single sediment library. These sites are considered potential hotspots for mis-alignment, and are thus removed from analyses for all libraries. In this manuscript, 0.22% of all sites with at least one mapped read (2103/955371) account for 2.63% of the reads, and were removed.
    b. We remove reads where the targeted allele does not match either of the expected allele states.
3. **Random read sampling:** We randomly selected a single read at each site.
4. **Proportion deaminated:** The proportion of C-T substitutions in reads with a reference C in the first or last three bases. [all Kraken categories – i.e., all reads, before metagenomic filtering with Kraken]
5. **Proportion hominin derived:** The proportion of derived alleles found at hominin-diagnostic positions - at such positions, ancestral alleles are expected to originate predominantly from faunal mis-alignment. See SI 6d. [all Kraken categories]
6. **Proportion hominin derived – deam only:** The proportion of derived alleles found at hominin-diagnostic positions - at such positions, ancestral alleles are expected to originate predominantly from faunal mis-alignment. [all Kraken categories, deaminated reads only]
7. **Primate:** Number of reads classified as Order Primate. Using the metagenomics software Kraken, we placed each read on the NCBI Taxonomy (*98*), and retained only reads classified to the primate clade. See SI 6e.

8. **Proportion deaminated (Primate):** The proportion of C-T substitutions in reads with a reference C in the first or last three bases, here only for reads classified as Primate.
9. **Proportion hominin derived (Primate):** The proportion of derived alleles found at hominin-diagnostic positions, here only for reads classified as Primate.
10. **Proportion hominin derived (Primate deam):** The proportion of derived alleles found at hominin-diagnostic positions, here only for *deaminated* reads classified as Primate.

6h.Simple population assignment

We explored the possibility of assigning sediment samples to broad archaic population groups defined by high-coverage individuals, similar to approaches taken in (*3*, *99*). Specifically, we considered deaminated DNA fragments overlapping sites where two high-coverage individuals are each homozygous, but differ from each other. The state in chimpanzee is taken as the ancestral state. In this way, we identify sites where one high-coverage individual (e.g. Altai Neandertal) is homozygous derived, and the other is homozygous ancestral (e.g. Denisovan individual); we would then refer to this category of sites as "Altai derived sites" (if comparing against another Neandertal) or "Neandertal derived sites" (if comparing against Denisovan, as in Fig. 4A – note that these are not necessarily derived in all Neandertals, these are conditioned on being derived in Altai, but we use them to represent the Neandertal state). For each sample and site category, we count the proportion of deaminated reads carrying a derived allele. For this analysis, we merged all libraries for a single sediment sample – including libraries that originated from independent sub-samples. In each of the analyses below, we required that a sample has data at least 30 informative sites, with the exception of two samples with Denisovan mtDNA: the previously published sediment sample SP3854 (De-E15) (*2*), and *Denisova 4*, with data at 29 and 28 sites, respectively. For comparison, we included sequencing data from 10 previously published skeletal samples with Neandertal or Denisovan nuclear DNA: *Denisova 11* (complete libraries R5780, R5782, R5783; (*1*)), *Denisova 8* (all libraries; (*27*)), *Denisova 4* (all libraries; (*27*)), *Mezmaiskaya 2* (30m reads from A9180; (*25*)), *Les Cottés Z4-1514* (30m reads from A9230; (*25*)), *Goyet Q56-1* (30m reads from A9229; (*25*)), *Spy 94a* (30m reads from R5556; (*25*)), *Mezmaiskaya 1* (150m reads from R5661; (*26*)), *Hohlenstein-Stadel (HST*; all libraries; (*19*)), *Scladina I-4a* (all libraries; (*19*)).

When considering sites where the Denisovan and *Altai Neandertal* genomes are homozygous and differ from each other, we find that all samples containing Neandertal mtDNA have high proportions of Neandertal derived alleles, and low proportions of Denisovan derived alleles; furthermore, sediment and skeletal samples cluster together (Fig. 4A, red points; lines are 95% binomial confidence intervals). In contrast, the sediment sample containing Denisovan mtDNA carries the Denisovan derived allele in 65% of cases but no Neandertal derived alleles (Fig. 4A, top left, blue point). Two previously published Denisovan skeletal samples (*Denisova 4* and *Denisova 8*) show similar results, although with a larger proportion of derived alleles at sites where the high-coverage Denisovan is homozygous derived. This may indicate that the Denisovan sediment sample originates from a more diverged Denisovan population – however, the number of informative sites in the sediment sample and *Denisova 4* are so low that the binomial confidence intervals of each overlap with the point estimate of *Denisova 8*, precluding

any strong interpretation. We note that even in richer samples, the number of informative sites is quite low. For 18 sediment samples from Chagyrskaya Cave and Estatuas, we have data at between 36 and 1220 sites per sample.

When considering sites that differ between two high coverage Neandertals, an even smaller number of sites are available for analysis; thus, confidence intervals are larger, fewer samples pass the 30-site threshold, and interpretations are more challenging. Specifically, when comparing Vindija vs Altai derived sites, 11 sediment samples from Chagyrskaya Cave and Estatuas have data at >30 sites (between 37 and 176 informative sites per sample); for Vindija vs *Chagyrskaya 8* sites, 5 sediment samples have data at >30 sites (between 37 and 78 informative sites per sample). In plots of these alleles (Figs. S15 and S16), even for samples with smaller CI, it is challenging to make strong interpretations, e.g about phylogenetic placement of sediment samples. We therefore developed a novel method for placing samples on a population tree of archaic individuals, described in SI 7.

6i. Coalescent simulations

For both the implementation of the branch time method (SI 7), and to evaluate the performance of said method (SI 6j), we performed coalescent simulations of the four high-coverage archaic individuals (*Chagyrskaya 8, Vindija 33.19, Altai Neandertal, Denisova 3*), a modern human population represented by Mbuti, and chimpanzee (pantro4). In each simulation, we also included an additional haploid population, representing a sediment sample. This population was placed at intervals throughout the entire phylogeny (example below).

Details of the demographic history were taken from (*9*). Specifically: Effective population sizes (Ne) were inferred with PSMC (*100*) for each high coverage archaic genome and one modern human [SI 6 of (*9*)]. For the common ancestors of more than one archaic (i.e., populations that are ancestral to the split of *Chagyrskaya 8* and *Vindija 33.19*), we used Ne estimates for *Vindija 33.19*. Tip dates for each archaic individual were inferred through branch shortening [SI 6 of (*9*)]. Population split times were inferred using the F(A|B) statistic. For the split of *Chagyrskaya 8* from *Vindija 33.19,* we used *Chagyrskaya 8* as the 'B' genome – that is, the split time is anchored to the tip date for *Chagyrskaya 8*. For the split of Altai from this branch, and the split of *Denisova 3* from all Neandertals, we performed the F(A|B) calculation in all configurations, and then averaged these values [SI 7 of (*9*)].

Implementation for population split time method: To place sediment samples on the Neandertal phylogeny, we require an estimate of the probability of observing a derived allele in a sediment sample, given its placement on the phylogeny. More specifically, we estimate p(*sed* = 1 | *b, t, archaics*), where *sed* is the haploid genotype of hominin DNA in a sediment sample, 1 represents a derived allele, *b* is the branch in the archaic phylogeny from which the sediment sample diverges, *t* is the time of divergence from this branch, and *archaics* is the set of genotypes of the four high coverage archaic genomes at the site of interest. We performed coalescent simulations as described above, in each simulation placing the population representing the sediment sample at either the split of two high-coverage individuals, or the tip of a branch. To obtain semi-independent SNPs, we simulated 100 million short regions (theta = 0.058, average 13 segregating sites per region). We then counted the proportion of derived states observed in the sediment sample for each configuration of archaic genotypes, branch, and branching time. Two examples are given in Table S6, where the probability of observing a

derived allele increases if it is more closely related to *Vindija 33.19*, when all archaics are homozygous ancestral, but *Vindija 33.19* contains a heterozygous site. Some configurations are much less likely to occur by chance, and thus have a smaller number of sites – in our simulations we observed between 3 thousand and 712 million sites for each configuration. In general, the least common configurations have heterozygous sites in all four archaic individuals – these configurations are removed in the real data, due to their increased probability of being caused by undetected paralogous regions.

6j. Evaluation of population split method with simulations

We evaluated the population split method both against simulated data (SI 6j, this section), and with previously published split-time estimates on skeletal data (SI 6m). We also artificially "contaminated" published skeletal data with modern human reads, to evaluate our ability to infer modern human contamination rates (SI 6k), and down-sampled published skeletal data to evaluate the robustness of our estimates with lower read counts in addition to modern human contamination (SI 6l).

We performed simulations as described in SI 6i, with a few modifications. First, to ensure independent sites, we sampled only a single site from each simulated region. Second, we placed the sediment sample at regular intervals along each branch - every 2.5ky for branch times up to 145ky, and then every 5ky for split times up to 245kya. Third, we simulated a larger number of modern human individuals, to obtain frequency estimates, and we artificially added 1000 sites to each simulation that are fixed derived in all hominins – these correspond to the hominin-diagnostic sites in the array design (SI 6d). For each branch and split time, we simulated ten iterations each, sampling between 1000 and 50000 SNPs (to evaluate performance on varying amount of data). The sites that are polymorphic in archaics make up about ¼ of these sites, and are the most informative for population split times, and thus we report this number below (therefore, the numbers below range from 250 SNPs to 12500 SNPs). In our array ascertainment, these make up ~40% of all sites.

For each simulation, we then estimated branch and population split time, along with modern human and faunal contamination.

Qualitatively, we find high correspondence with the simulated branch time and the estimated branch time (Fig. S18, x- and y-axis respectively), and the simulated branch and estimated branch (Fig. S18, colors vs rows). As expected, our accuracy increases with larger numbers of SNPs that are polymorphic in archaics (Fig. S18 columns, from 250 SNPs to 12500 SNPs), with high correlation coefficients on all branches with at least 2500 SNPs (Spearman's rho >= 0.948 on all branches).

Encouragingly, MLE estimates are robust for the time periods where we infer the Estatuas samples to have diverged – that is, the time periods around the split of Vindija and Chagyrskaya (104kya, Fig. S18 left black X), and the split of their ancestral population and Altai (135kya, Fig. S18 right black X). (Black box in Figure S18 shows +/- 20ky around these split times).

We do observe biases in other parts of the tree – for example, population split estimates on the Denisova branch, and on the Neandertal ancestral branch >150kya are generally under-

estimated. Split times on the Chagyrskaya branch are generally slightly over-estimated. Errors in the estimates for older timepoints appear to be associated with slight over-estimates of modern human contamination (Fig. S19, modern human contamination as a function of simulated split time; simulated contamination is 0%, estimated contamination ranges from 0-5%).

6k. Modern human contamination estimates are robust

We evaluated the population split method both against simulated data (SI 6j), and with previously published split-time estimates on skeletal data (SI 6m). We also artificially "contaminated" published skeletal data with modern human reads, to evaluate our ability to infer modern human contamination rates (SI 6k – this section), and down-sampled published skeletal data to evaluate the robustness of our estimates with lower read counts in addition to modern human contamination (SI 6l).

To evaluate our estimates of modern human contamination with real data, we combined sequencing data from low-coverage Neandertal genomes (*Mezmaiskaya 1* or *Goyet Q56-1*) and sequencing data from a modern human which has been treated to be similar to ancient DNA (*96*), and then estimated modern human contamination proportions, along with branch time estimates. This approach closely mimics real world situations.

We find that our modern human contamination estimates are highly accurate, with average absolute error of ~2% or less for both *Mezmaiskaya 1* and *Goyet Q56-1*, given at least 1500 DNA fragments (Fig. S20). We note that this comparison assumes that the true amount of modern human contamination in either *Mezmaiskaya 1* or *Goyet Q56-1* is 0%, which is likely not the case. Previously published estimates of modern human contamination for this *Mezmaiskaya 1* library are 1.99% (*26*) or 3% (*25*). Estimates for just this *Goyet Q56-1* library were not published, although for the whole low-coverage genome (constructed from three libraries), the point estimate is 0.89% (*25*). This low level of true modern human contamination would be expected to inflate our estimates, and could explain some of the 1-2% error in our estimates.

6l. Robustness of population split time estimates in down-sampled skeletal data with modern human contamination

We evaluated the population split method both against simulated data (SI 6j), and with previously published split-time estimates on skeletal data (SI 6m). We also artificially "contaminated" published skeletal data with modern human reads, to evaluate our ability to infer modern human contamination rates (SI 6k), and down-sampled published skeletal data to evaluate the robustness of our estimates with lower read counts in addition to modern human contamination (SI 6l – this section).

In addition to asking whether our method can recover the true branch and population split time, when these are known from simulations (SI 6j), we also investigated the robustness of the results on real data, with lower read counts. To this end, we compared results obtained from two skeletal samples with large amounts of data (*Mezmaiskaya 1*: 65454 reads; *Goyet Q56-1*: 52409 reads), with results on those same samples when reducing the number of reads.

Specifically, we sampled 20k reads from each sample, and estimated branch and population split times for those reads. There is little variability when re-sampling 20k reads 100 times (Fig. S21, right side; average absolute deviation from point estimates across resampling is 1-1.5ky); we thus take the average of these estimates as the "truth" (Fig. S21, dotted line), and compare

repeated down-samplings to this value. We find that average error is low even with small numbers of SNPs (Fig. S21, gray text) – for example, for both samples average absolute error is less than 5ky with at least 2500 SNPs.

We then added between 0% and 90% modern human contamination to each down-sampling, as described in SI 6k. We find that our population split time estimates are robust even with moderate levels of contamination, with less than 10ky average absolute error with at least 1500 endogenous DNA fragments and up to 75% contamination (Fig. S21).

6m. Comparison to previously published split times for low coverage Neandertal genomes

We evaluated the population split method both against simulated data (SI 6j), and with previously published split-time estimates on skeletal data (SI 6m – this section). We also artificially "contaminated" published skeletal data with modern human reads, to evaluate our ability to infer modern human contamination rates (SI 6k), and down-sampled published skeletal data to evaluate the robustness of our estimates with lower read counts in addition to modern human contamination (SI 6l).

We tested our EM method for estimating population split times by calculating split times for existing skeletal samples, and comparing against previously published results. We considered the following skeletal samples:

Four low-coverage late Neandertals from (*25*):

- *Mezmaiskaya 2*
- *Les Cottés Z4-1514*
- *Goyet Q56-1*
- *Spy 94a*

Additionally:

- *Mezmaiskaya 1*, 55–70 ka Neandertal individual from the Northern Caucasus (*26*).
- *Hohlenstein-Stadel (HST)*, a ~120 ka Neandertal from Hohlenstein-Stadel Germany (*19*)
- *Scladina I-4a*, a ~130 ka Neandertal from Western Europe (*19*)

For these samples, we estimated population split times and branches, along with modern human and faunal contamination (Table S9). For all samples, faunal contamination estimates were less than 0.001%, consistent with their origin as skeletal, and not sediment, samples. We compared these estimates with previous modern human contamination estimates (Table S8) and split time estimates (Table S7). Split time estimates are taken from (*19*) tables S46 and S47, which used two approaches for calculating split times: F(A|B) and a coalescent divergence model:

1. The F(A|B) statistic, which corresponds to the proportion of derived alleles observed in a haploid genome A, at sites which are heterozygous in a diploid genome B (*26*). This proportion depends on the divergence date of the two populations. Roughly: if A diverged quite close to the tip of the B lineage (that is, if A is closely related to

B), then A will share many derived alleles with B. As the divergence of A from B moves further into the past, A will share fewer derived alleles with B. The expected derived allele proportions depend on the demography of population B, but are independent of the demography of A. These expected proportions are calculated from simulations, where the tip date and effective population sizes of B are estimated using branch shortening and PSMC, respectively, on a high coverage genome of individual B.

2. A coalescent divergence model (*101*), which uses counts of alleles supporting three tree topologies, for two high coverage genomes and a low coverage sample of interest. In this case, *Vindija 33.19* and the Altai Neandertal were used. This model assumes a constant Ne for all populations – here we take estimates with Ne = 2000, which is closest the the PSMC estimates for Neandertals (*19*). For *Spy, Goyet, Mezmaiskaya 2, Mezmaiskaya 1, and Les Cottés*, the split time between *Vindija 33.19* and the Altai Neandertal was set to 137kya. For *HST* and *Scladina*, the split time was set to 130kya or 145ky (130kya is closest to the 135kya date used in this manuscript). We note that this model by its nature estimates a divergence time that is *younger* than the split time of the two high coverage individuals used in the analysis, and thus a confidence interval which includes the split time itself could indicate an even older true split time.

When comparing our population split results with previous results, we find stronger concordance with the coalescent split method, with the 95% CI overlapping for all samples except *Goyet* and *Spy*, for which we infer older split dates (Table S9). Previously published split dates for *Goyet* and *Spy* are very close to the tip of the Vindija branch, an area where our method tends to over-estimate split dates (Fig. S18) – consistent with this discrepancy.

Our estimates of modern human contamination (Table S9) are very similar to previous estimates (Table S8), with the exception of *HST* and *Scladina*, where we estimate higher modern human contamination proportions. However, several of the processing steps in our analysis may preferentially remove deaminated reads, thus increasing the relative proportion of human contaminants in highly contaminated libraries. For example, by aligning to a third-base-reference, where the number of allowed mismatches is essentially reduced by one, we are less likely to align highly deaminated sequences. In highly contaminated libraries, decreasing the proportion of deaminated sequences necessarily increases true levels of modern human contamination.

6n.Population split time estimates and implementation details

We ran our EM method for estimating population split times and branches for all sediment libraries with at least 100 DNA fragments overlapping informative SNPs (defined below), and in some cases for sets of libraries together (below).

For each run, we both ran the EM algorithm on the full dataset, and performed 100 block-bootstraps with 100 blocks; the full dataset and each block-bootstrap each have a MLE split time and branch. The full dataset MLE branch, split time, faunal and human contamination are reported in Table S14. We calculated 95% confidence intervals on the population split times by excluding the block-bootstraps with the oldest and youngest split times. All MLE branches

included in these bootstraps are reported as 95% CI for branches. 95% CI are also reported in Table S14.

Not all positions included in the array are informative for the MLE method – partially because our array design was built on previous array designs. We selected SNPs that fit one of three categories: 1) polymorphic in archaics (informative for placement on the archaic phylogeny), 2) fixed ancestral in archaics and polymorphic in modern humans (informative for estimating modern human contamination), and 3) hominin-diagnostic SNPs (informative for estimating faunal mis-alignment) (SI 6d).

As described in SI 6j-6l, accuracy of the method is low for libraries with <500 SNPs or with MLE modern human contamination estimates >70%. Additionally, we observed very broad confidence intervals for such libraries – with the 95% CI of possible branches often including all branches (including the Denisova branch). These results are therefore not considered for further analysis.

For Estatuas, we merged libraries originating from the same sub-sample. For example, the results presented for sub-sample GE-I-A4l in Figure 5A are inferred from four libraries: A20281, A24518, A24519 and A24756 (others described in Table S14, labeled as "Merged <subsample>"). We additionally performed MLE estimates for merged sub-samples originating from the same layer, as long as they also carried the same broad mtDNA type (*HST* vs non-*HST*). These are labeled as "Merged lysates" in Table S14.

SI7 - Likelihood model for population split times

Introduction

Here we describe a maximum-likelihood framework for identifying the population split time of a target population X, represented by a skeletal or sediment sample from which ancient DNA has been retrieved, from a phylogeny of four archaic individuals. This phylogeny is defined by the three high-coverage Neandertal genomes - *Denisova 5* (the 'Altai' Neandertal), *Vindija 33.19*, and *Chagyrskaya 8* (Fig. 4C, (*7, 9, 26*)), plus the high-coverage Denisovan genome (*Denisova 3*, (*8*)).

This method is similar to the $F(A|B)$ method, described in (*7*), which considers (i.e. ascertains) heterozygous sites in a single high-coverage genome, and calculates the proportion of these sites at which a sample X carries a derived allele. This proportion is then compared to simulations of two archaic populations which diverge from each other at some point back in time. One population represents the high-coverage individual, and a second represents X. As the time of divergence between the two populations increases, the expected proportion of derived alleles in X (at ascertained sites) will decrease - that is, when X is more distantly related to the high coverage individual, the two will share fewer derived alleles. By comparing the observed and expected proportions, we can estimate the time at which X diverged from the population of the high-coverage individual.

We extend this method to estimate divergence from a phylogeny, rather than a single lineage. In part, this allows us to extend the number of sites that are considered informative. For this application, all sites that are polymorphic in archaics are informative - we does not need to restrict themselves to heterozygous sites in a single individual. For example, at a site which is heterozygous in *Vindija 33.19*, but ancestral in all other archaics, the probability of observing a derived allele in a sample X varies based on the point at which X diverged from the overall tree (Fig. 4C, black points and bar plot). Similar to $F(A|B)$, these probabilities are obtained from coalescent simulations, for which effective population sizes, split times and tip dates are inferred from the respective high-coverage genomes (SI 6i).

In addition to estimating the population split time, we co-estimate faunal mis-alignment and modern human contamination, and do so independently for different portions of the data (described below).

Model Overview

Although the goal is to identify the branch from which a population diverged, and the time of the divergence t, the method considers each branch independently. Specifically, we determine the maximum likelihood estimate of t for each branch, and then select the branch (and t) with the highest likelihood. Thus, in the formulation of the model, we consider b as fixed and focus on estimating t.

We assume that we have genomic sequence data that can be subdivided into distinct read groups r. Read groups are simply disjoint sets of sequencing reads, for which we estimate independent contamination rates, similar to the approach in (*102*). We assume that at each SNP s we have a single read O_{rs}, each of which carries an ancestral or derived allele, represented as a 0 or 1, respectively. Each read either originates from an "endogenous" haploid genotype H, i.e. from an archaic hominin, or from faunal or human contamination at rates f and c respectively. These rates are independently estimated for each read group (f_r, c_r); for example a library may be divided into deaminated and non-deaminated reads, and these would be expected to have different rates of modern human contamination.

In the case of sediment DNA, we could imagine further subdivisions based on the probability that the read originates from a hominin individual, e.g. represented by its metagenomic assignment in Kraken (*24*). For simplicity, these subsets are considered separate read groups below. As stated above, each read group will have its own contamination and error parameters.

Notation

Let

- R, the number of read groups
- S_r, the number of SNPs from read group r - as a single read is sampled at each site, this is equivalent to the number of reads in a read group r
- S, the total number of SNPs - as a single read is sampled at each site, this is equivalent to the sum of all SNPs/reads in all read group r
- $O = (O_{rs})$, the set of observed alleles from read group r at SNP s - O_{rs} will always represent a single read, and thus either the ancestral or derived state (0 or 1, respectively)
- $H = (H_s)$, the set of haploid genotypes of SNP s. Each H_s is simply either the ancestral or derived genotype, represented by 0 or 1, respectively

- t, the divergence time of the sample from the larger phylogeny
- c_r, proportion of contaminant modern human reads in read group r
- f_r, proportion of non-hominin (faunal) mammalian reads in read group r
- p_s, the derived allele frequency of a modern human contaminant at SNP s
- p_f, the derived allele frequency of a mis-aligned faunal read
- e, a composite parameter of the rate of sequencing error and aDNA damage
- $\theta_r = (c_r, f_r)$, the set of non-time parameters to be estimated
- θ = (θ_r), the set of θ_r for all read groups r.

Algorithm details

We are primarily interested in estimating the divergence time t. The true underlying genotypes H are a latent state. We additionally estimate contamination parameters c and f.

The following data log-likelihood integrates over all possible values of H, and is easy to compute given t, θ, but may be challenging to optimize. For example, with four read groups, we have nine parameters to optimize (a global t, plus θ_r (c_r and f_r) for each read group).

$$\mathcal{L} = \log P(O|t,\theta) = \sum_{r=1}^{R}\sum_{s=1}^{S_r} \log \sum_{h=0}^{1} P(O_{rs}|H_s = h, \theta_r) P(H_s = h|t) \tag{1}$$

Instead, we can formulate the complete data log-likelihood (assuming the latent variable H is known), and maximize this using an EM-algorighm. The complete data log-likelihood is:

$$\begin{aligned}\mathcal{L} = \log P(O, H|t,\theta) = &\sum_{r=1}^{R}\sum_{s=1}^{S_r} \log P(O_{rs}|H_s, \theta_r) \\ &+ \sum_{r=1}^{R}\sum_{s=1}^{S_r} \log P(H_s|t)\end{aligned} \tag{2}$$

In this construction, where the t and all θ_r parameters are split into separate terms, each term can be optimized separately (described in the following section). The first term describes

the probability of the observed sequencing data for a sample, given the true haploid genotype and various contamination and error parameters. The second term describes the probability of a genotype, given the divergence time. We assume that genotypes are independent across sites.

Parameter Estimation

The Q-function to be maximized is:

$$\begin{aligned} Q(t,\theta|t',\theta') &= E_{\theta',t'}[\log P(O,H|t,\theta)] \\ &= \sum_{H} \log P(O,H|t,\theta) P(H|O,t',\theta') \\ &= \sum_{s=0}^{S} \sum_{H_s=0}^{1} \log P(O_s,H_s|t,\theta) P(H_s|O,t',\theta') \end{aligned}$$

where:

$$\log P(O_s,H_s|t,\theta) = \log P(O_s|H_s,\theta) + \log P(H_s|t)$$

and:

$$P(H_s|O_s,t',\theta') = \frac{P(O_s|H_s,\theta')P(H_s|t')}{\sum_{h=0}^{1} P(O_s|H_s=h,\theta')P(H_s=h|t')}$$

The vector $P(H_s = h|O_s,t',\theta')$ is precomputed for all s,h each EM round, using t',θ' from the previous round, and stored as γ_{sh}.

Independent optimizations

Because $\log P(O_s|H_s,\theta)$ depends only on θ, and $\log P(H_s|t)$ depends only on t, we can optimize these separately. Therefore, the Q-function for t is:

$$Q(t|t') = \sum_{r=1}^{R} \sum_{s=0}^{S_r} \sum_{h=0}^{1} \log P(H_s=h|t)\gamma_{sh}$$

and the Q-function for θ is:

$$Q(\theta|\theta') = \sum_{r=1}^{R} \sum_{s=0}^{S_r} \sum_{h=0}^{1} \log P(O_s|H_s = h, \theta)\gamma_{sh}$$

We therefore optimize branch time using data from all read groups:

$$\hat{t} = \underset{t}{\operatorname{argmax}} \sum_{r=1}^{R} \sum_{s=0}^{S_r} \sum_{h=0}^{1} \log P(H_s = h|t)\gamma_{sh}$$

and optimize f_r and c_r separately for each read group:

$$(\hat{f_r}, \hat{c_r}) = \underset{f_r, c_r}{\operatorname{argmax}} \sum_{s=0}^{S_r} \sum_{h=0}^{1} \log P(O_s|H_s = h, \theta)\gamma_{sh}$$

Haploid genotype probabilities given a branch and a branch time

The probability of observing the haploid genotype H_s, given branching time and branch t and b

$$P(H_s|b, t)$$

is obtained from simulations of the population history of four high coverage archaic individuals: in this case, three Neandertals and one Denisovan. Simulations are described in section SX. To ensure a smooth likelihood surface, for each branch we obtain $P(H_s|b, t)$ for the minimum and maximum values of t : (t_{min}, t_{max}), and set

$$P(H_s|b, t) = L_{min} + (L_{max} - L_{min}) \frac{t - t_{min}}{t_{max} - t_{min}}$$

where

$$\begin{aligned} L_{min} &= P(H_s|b, t_{min}) \\ L_{max} &= P(H_s|b, t_{max}) \end{aligned} \tag{3}$$

Haploid genotype likelihoods given observed reads and contamination and error parameters

We assume a simple Bernoulli mixture of contaminant and endogenous reads similar to (*103*). The error rate e switches the allele to the other state.

$$\log P(O_s = 1|H_s, \theta = (c_r, f_r, p_f, e)) = (1-e)p' + e(1-p')$$

where

$$p' = c_r p_c + f_r p_f + (1 - c_r - f_r)H_s$$

Practical Notes

To ensure a continuous parameter space, the EM is run once per branch, such that we estimate the MLE of t and θ for each branch. Given these optimized parameters, we then calculate the data log-likelihood for that branch using equation 1. The branch and parameters with the highest data log-likelihood are then selected as the MLE branch and parameters.

The parameters p_f and e are fixed for a given analysis. Typically, p_f is set in the range $0 - 0.05$, and e to 0.001. Note that it is unlikely that p_f is truly 0, given that double-mutations are likely to occur over the long evolutionary distances considered here.

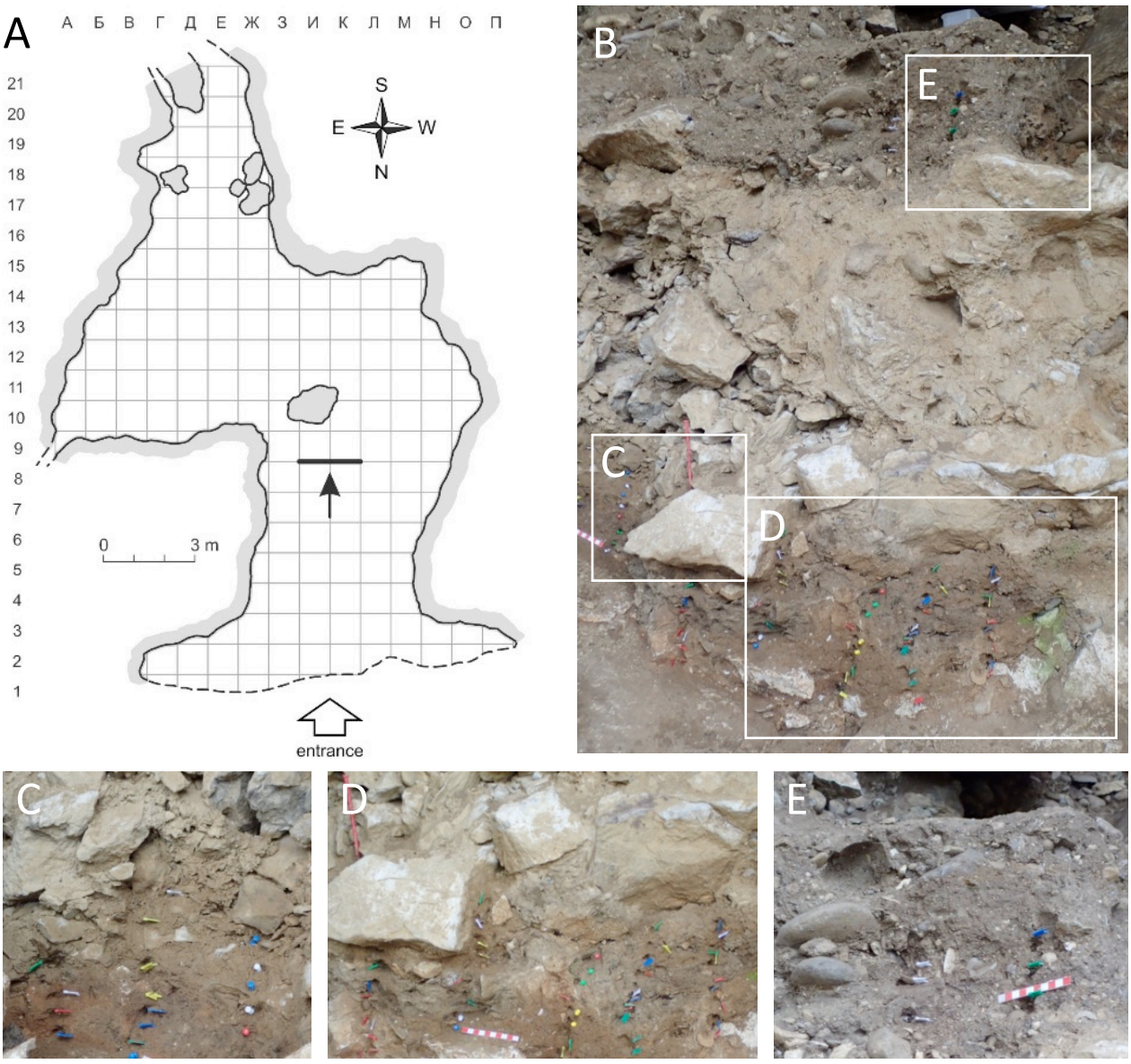

Figure S1 (**A**) Plan map of Chagyrskaya Cave showing the location of the stratigraphic section from which sediment DNA samples were collected in 2017. See Figure 1B for the corresponding section drawing with individual sample locations and Layer numbers. (**B**) Photo of the sampled section, showing the positions of the 10 vertical sample columns (8 and 2 columns towards the bottom and top of the photo, respectively). Colored flags mark individual sample locations and white squares correspond to the photos in panels C–E. (**C**)–(**E**) Photos showing detail of sample columns. Scale bar in each photo, 1 cm increments.

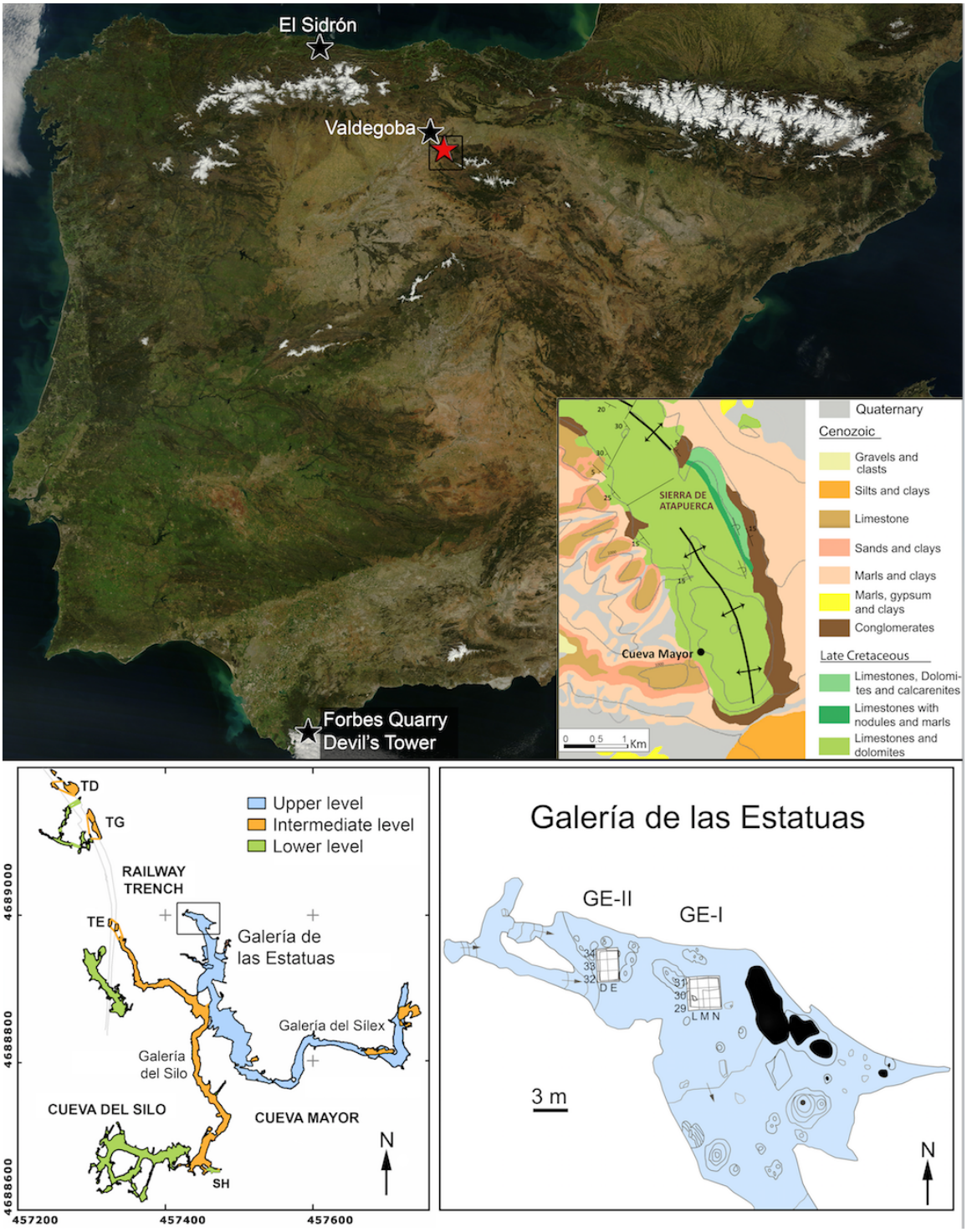

Figure S2 Top: Location of the Sierra de Atapuerca site complex within the Iberian Peninsula and geological setting of the Sierra de Atapuerca (small square). Other Neandertal sites that have yielded ancient DNA are represented by black stars. Modified from Arsuaga et al., 2017 (*11*). Bottom: Location of the Galería de las Estatuas within the Cueva Mayor-Cueva del Silo cave system and in relation to the sites located in the railway trench. The two test pits (GE-I to the east, and GE-II to the west) are located at the end of the Galería de las Estatuas. SH = Sima de los Huesos; TD = Trinchera Dolina; TE = Trinchera Elefante; TG = Trinchera.

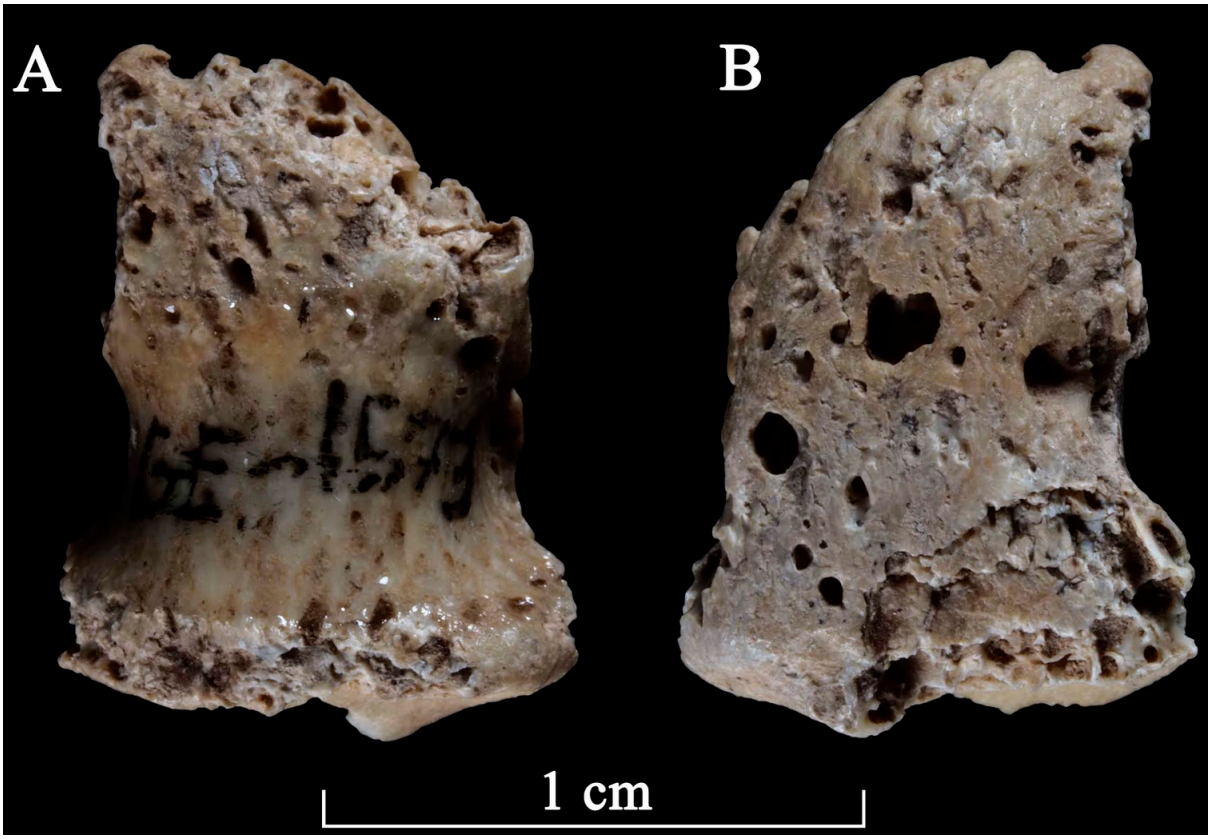

Figure S3 Neandertal right distal foot phalanx from the fifth toe (GE-1573) recovered at Galería de las Estatuas pit I in dorsal (A) and plantar (B) views. Images from Javier Trueba (Madrid Scientific Films). Modified from Pablos et al., 2019 (*12*).

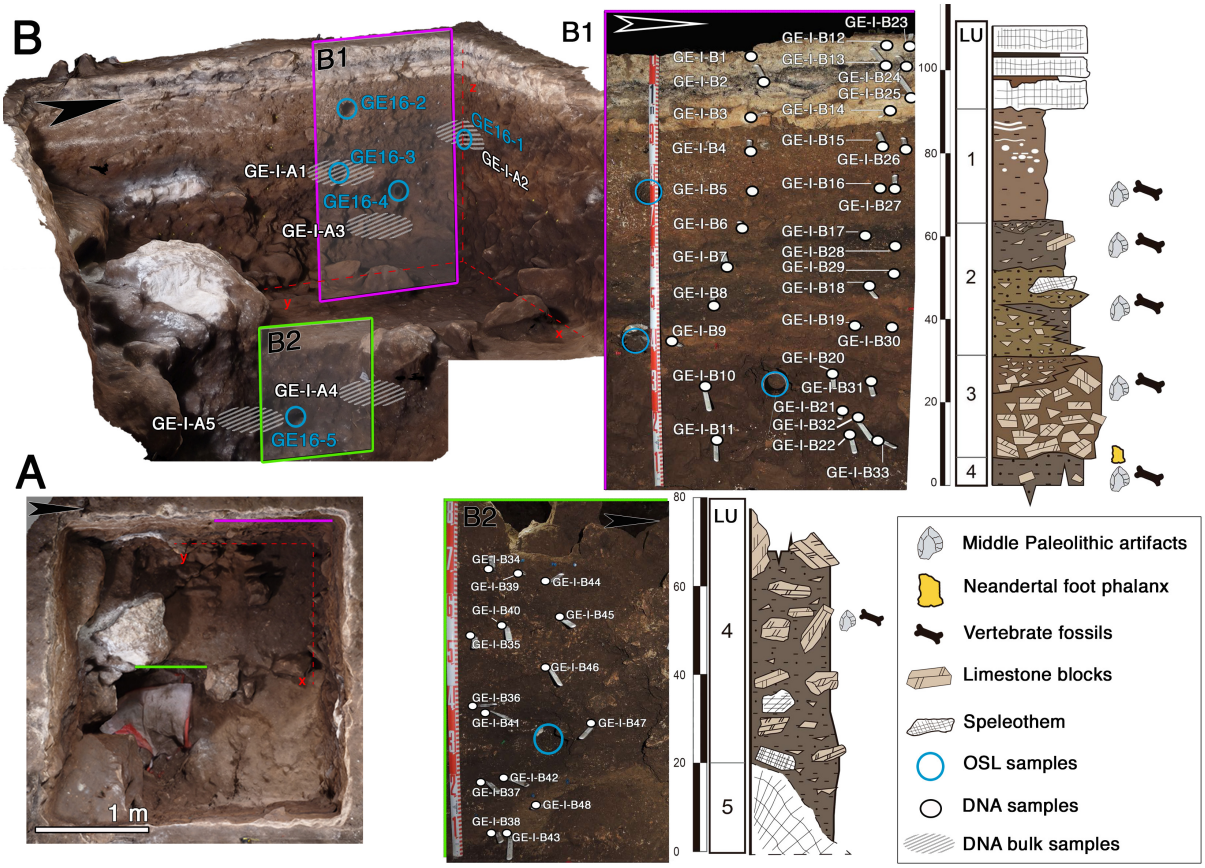

Figure S4 Location of DNA samples in Estatuas pit I (GE-I) in relationship with the OSL sampling points. (**A**) Cenital view of GE-I. (**B1**) Sampling performed in the western profile of square L31. (**B2**): Sampling performed in the western and northern profiles of square M30. The arrows indicate the north. Samples for DNA analysis were collected close to the sampling locations for OSL dating to provide a precise chronostratigraphic framework.

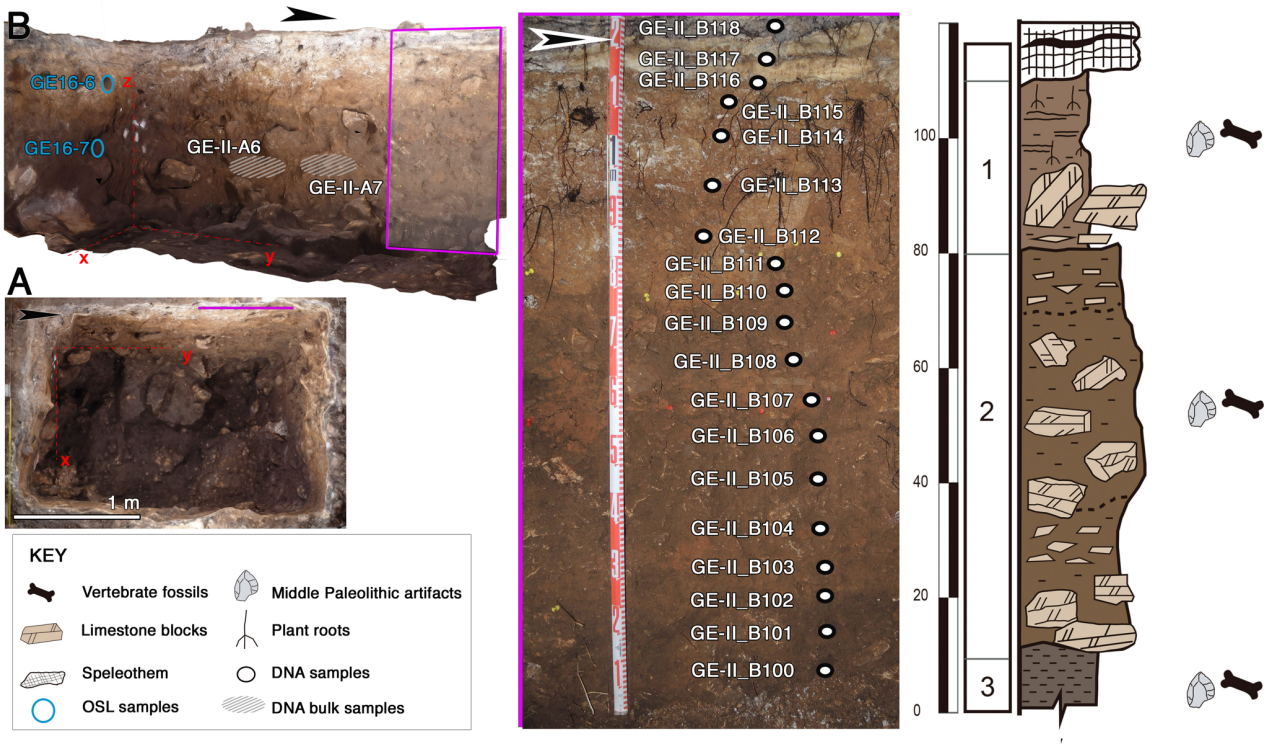

Figure S5 Location of DNA samples in Estatuas pit II (GE-II) in relationship with the OSL sampling points. (**A**) Cenital view of GE-II. (**B**) The detailed sampling was performed in the western profile of square D34. The arrows indicate the north. The bulk samples GE-II-A6 and GE-II-A7 were taken from the western profile of square D33. Two additional bulk samples were taken in the opposite profile (not shown).

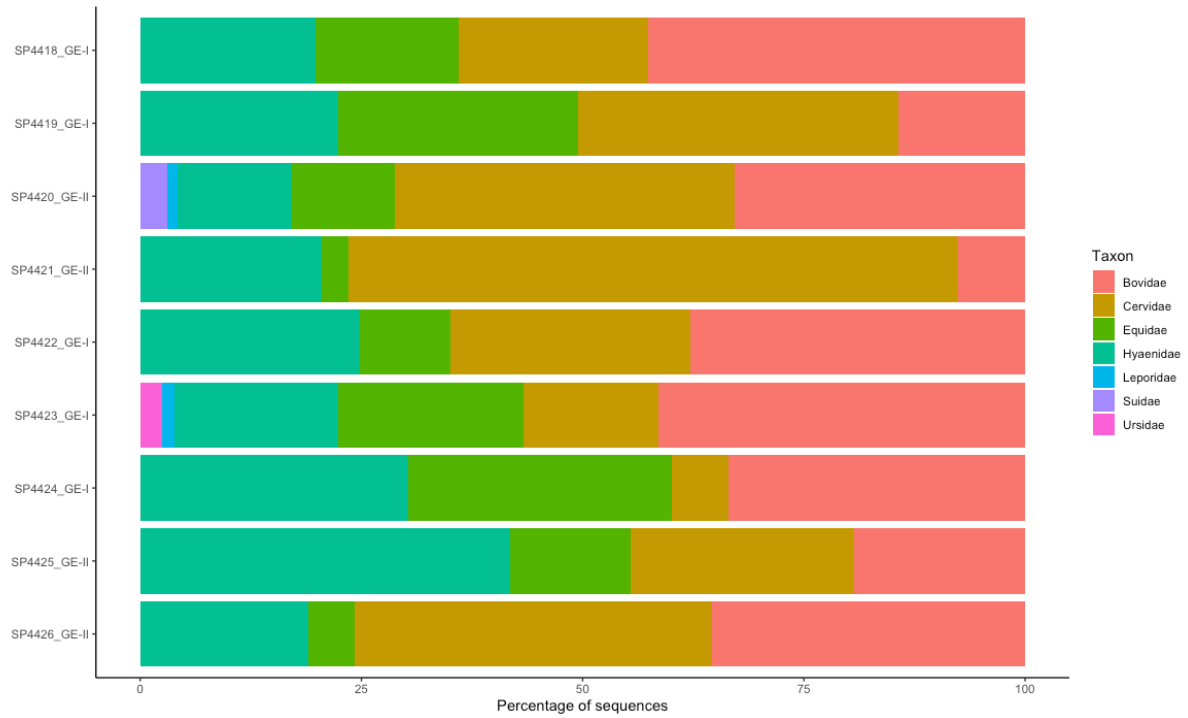

Figure S6 Ancient taxa identified in the first nine sediment samples collected at Galería de las Estatuas. Only mammalian families identified as containing ancient mtDNA fragments are plotted.

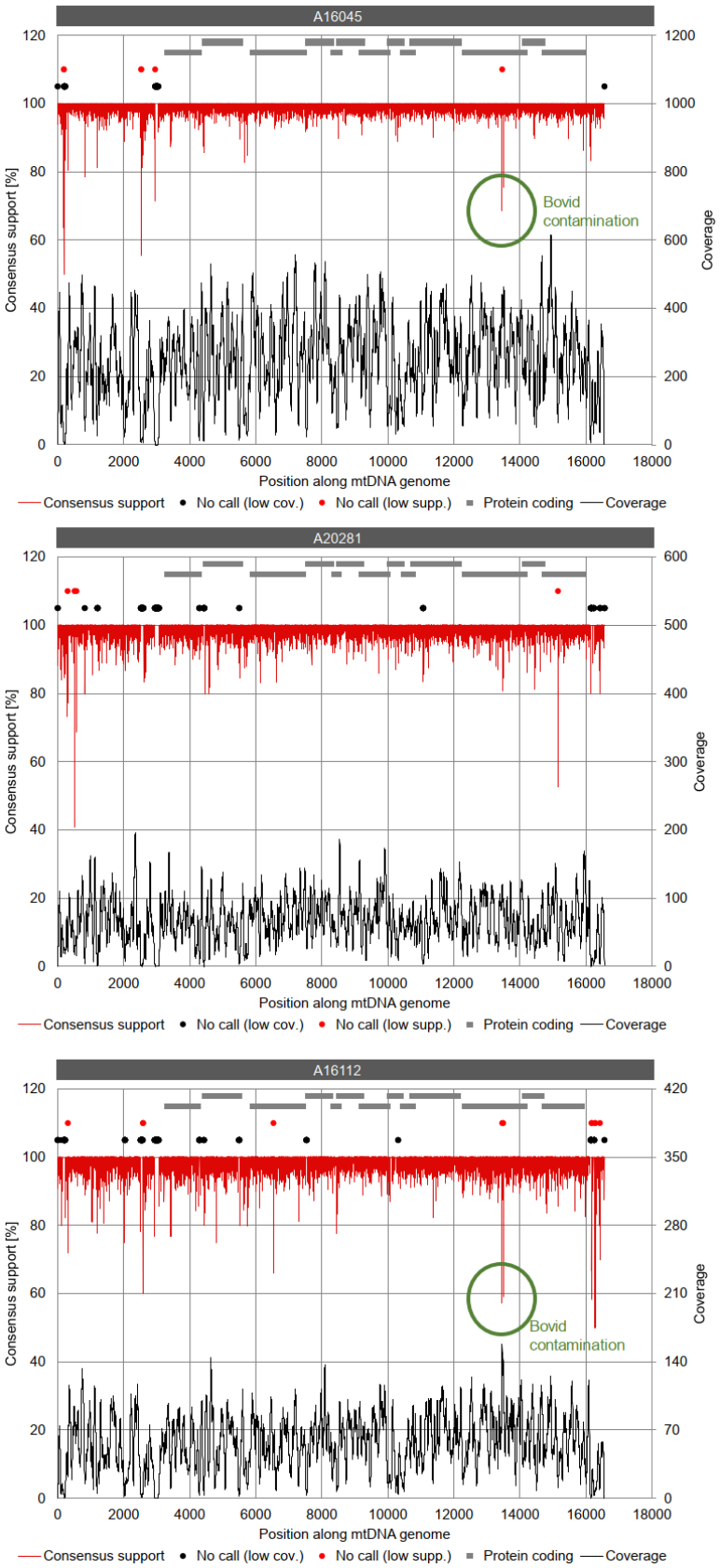

Figure S7 Mitochondrial coverage and consensus support for 3 libraries from Galería de las Estatuas sediment samples that are putatively dominated by mtDNA sequences from single individuals. Manual corrections of the consensus due to the presence of falsely assigned bovid sequences are marked by green circles.

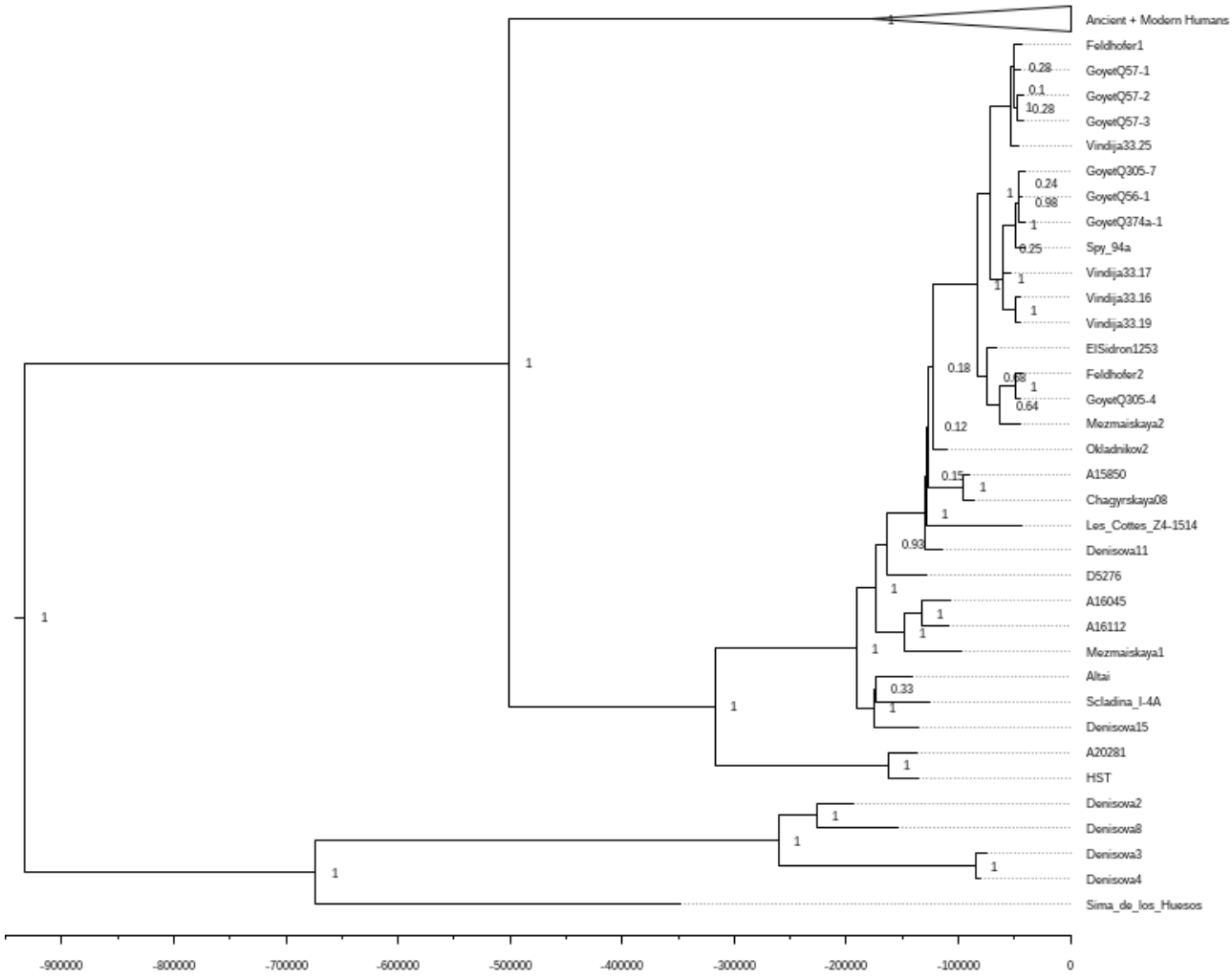

Figure S8 Hominin mtDNA tree determined from Bayesian analysis with Beast2. Each node shows the corresponding posterior probability of the branch and the x-axis represents the time in years before present. The branch for the Chimpanzee mtDNA genome used to root this tree is not shown.

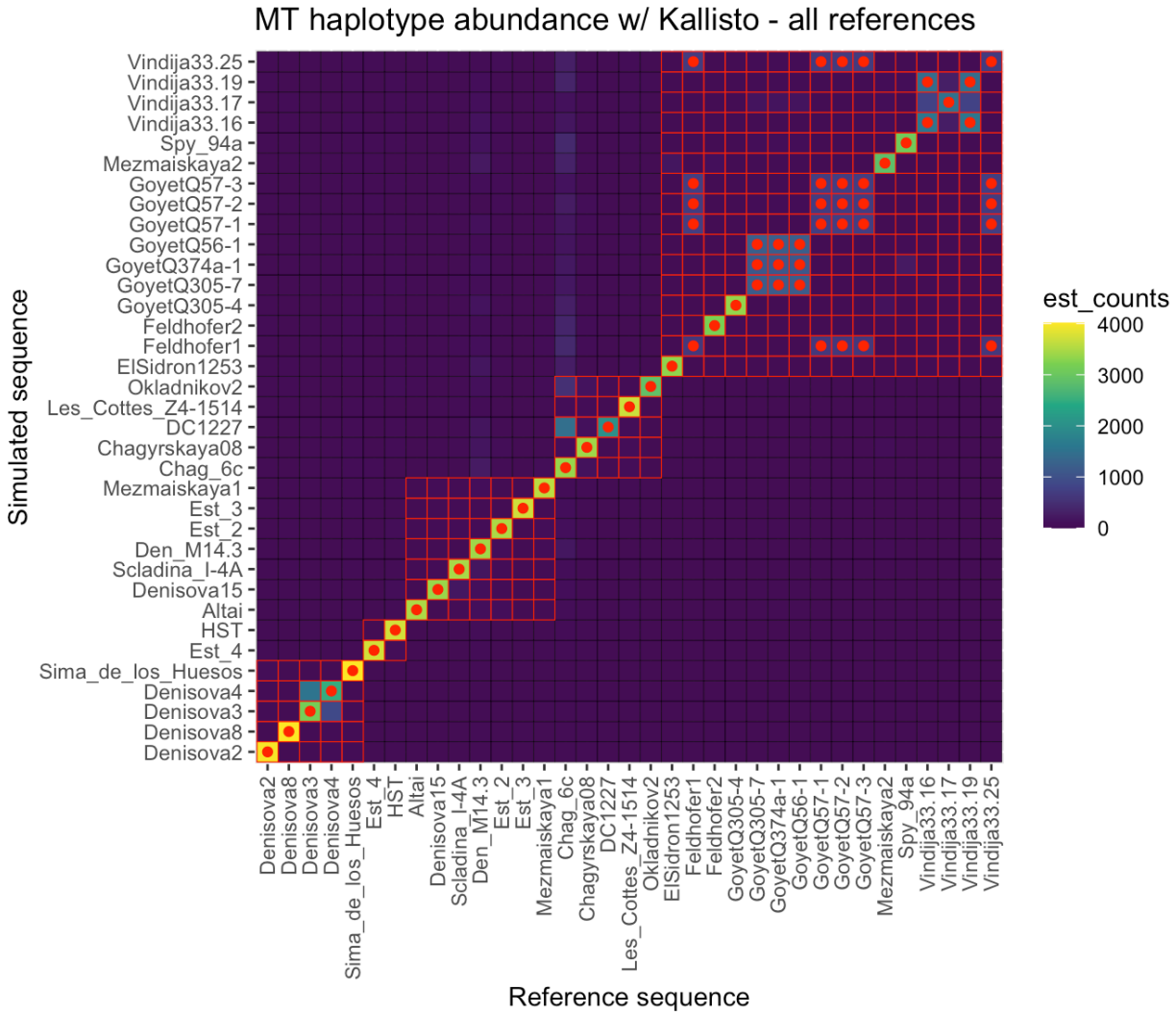

Figure S9 mtDNA haplotype abundance estimates with kallisto – full reference set.
Fill color shows kallisto abundance estimates for simulated mtDNA; haplotypes from which aDNA was simulated is shown on the y-axis, and reference haplotypes are shown on the x-axis. Each row represents abundance estimates for a single simulated dataset. Reference sequences are the same as in Figure 2B, and include five sediment consensus sequences: Est_2, Est_3 and Est_4 are from Estatuas pit II/Layer 2, pit I/Layer 3, and pit I/Layer 4, respectively. Chag_6c is from Chagyrskaya Cave Layer 6c. Den_M14.3 is from Denisova Cave Main Chamber, Layer 14.3. DC1227 is *Denisova 11*. Red boxes denote five major mtDNA groupings, and are the same as groupings in Figure 2A. Red dots denote the highest abundance reference(s) for each simulated dataset.

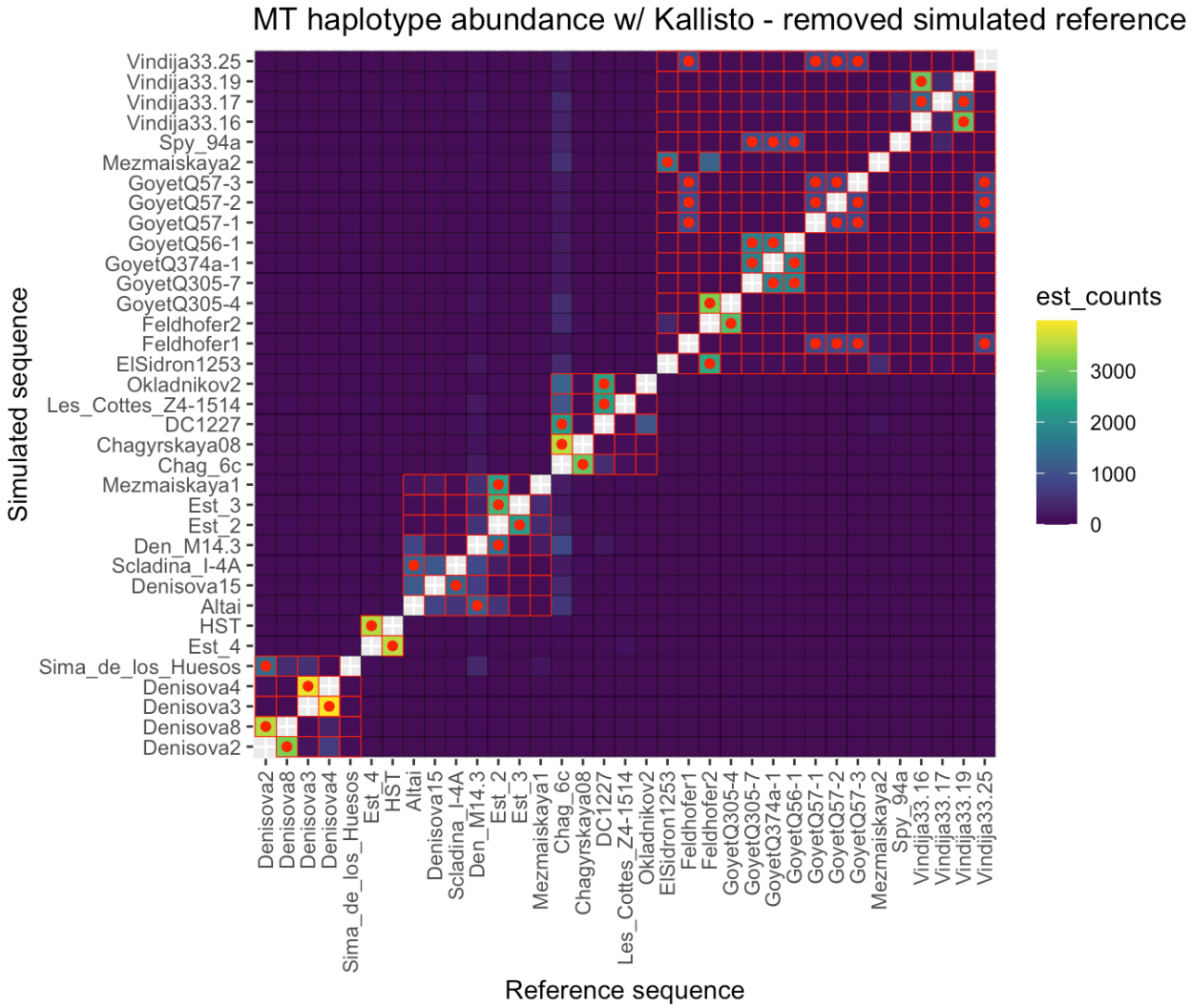

Figure S10 mtDNA haplotype abundance estimates with kallisto – dropping simulated haplotype. Fill color shows kallisto abundance estimates for simulated mtDNA; haplotypes from which aDNA was simulated is shown on the y-axis, and reference haplotypes are shown on the x-axis. For each simulated dataset, the "correct" haplotype was removed from the set of reference haplotypes (empty squares on diagonal). Each row represents abundance estimates for a single simulated dataset. Reference sequences are the same as in Figure 2B, and include five sediment consensus sequences: Est_2, Est_3 and Est_4 are from Estatuas pit II/Layer 2, pit I/Layer 3, and pit I/Layer 4, respectively. Chag_6c is from Chagyrskaya Cave Layer 6c. Den_M14.3 is from Denisova Cave Main Chamber, Layer 14.3. DC1227 is *Denisova 11*. Red boxes denote five major mtDNA groupings, and are the same as groupings in Figure 2A. Red dots denote the highest abundance reference(s) for each simulated dataset.

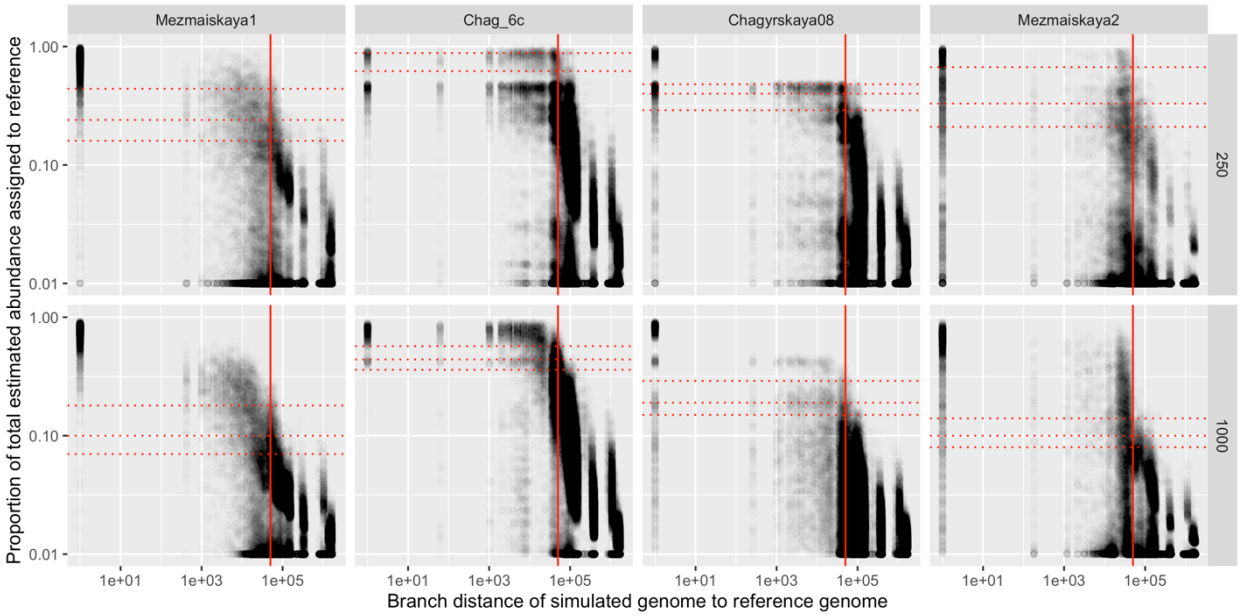

Figure S11 Example abundance thresholds for four mtDNA references. Normalized abundances assigned to each of four reference genomes (columns), for simulated ancient DNA from ancestralized genomes spanning the mitochondrial tree. Each point is one simulated mtDNA genome. Red vertical line denotes 50ky – points to the left of this line are from ancestralized genomes that are less than 50ky diverged from the reference genome branch, and are considered "closely related". For each reference, three abundance thresholds were calculated (red dotted lines), such that 90%, 95% and 99% (bottom to top) of all simulated sequences with at least this abundance are more closely related than 50ky. Thresholds were calculated for 250 and 1000 simulated DNA fragments (rows).

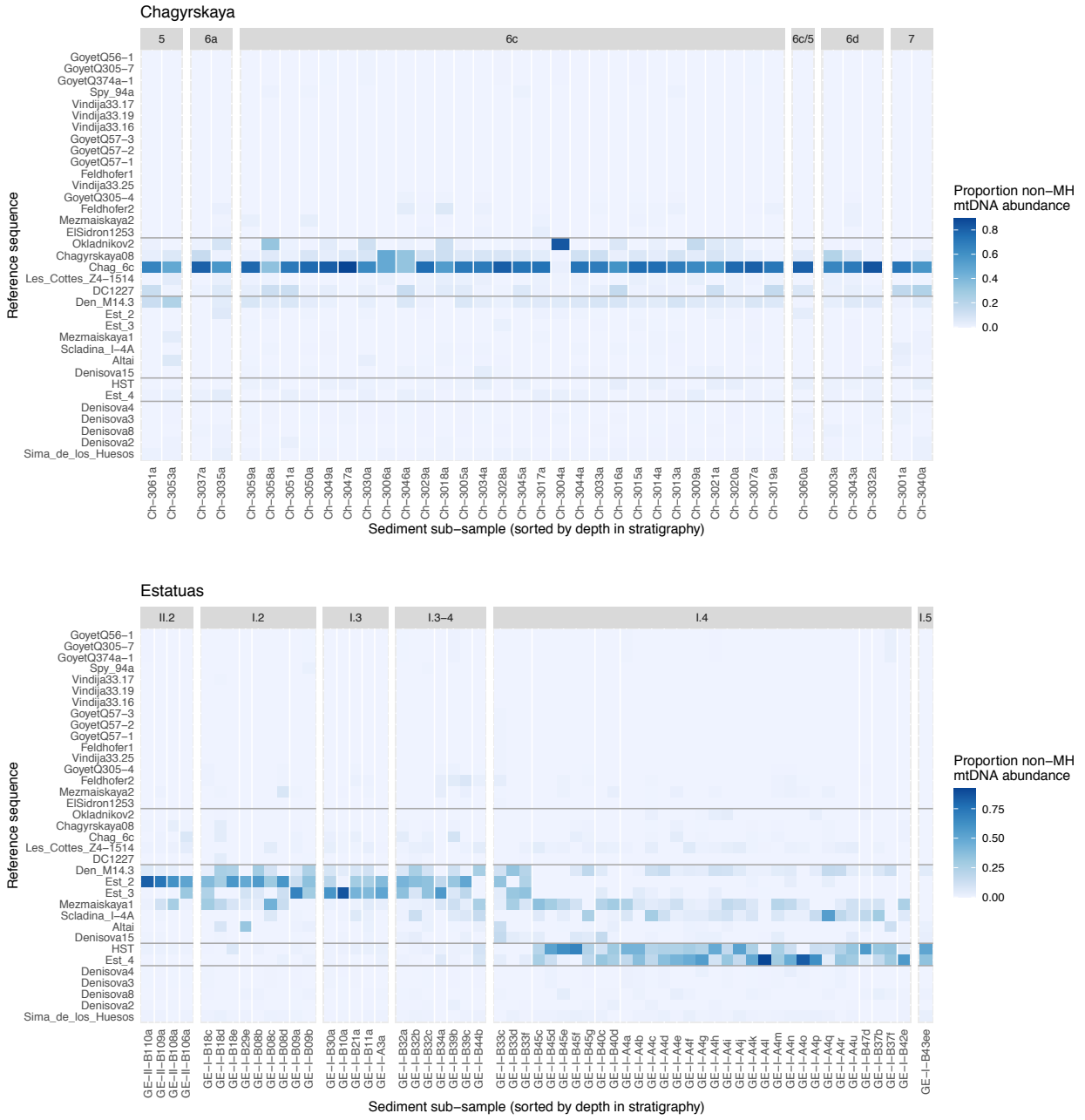

Figure S12 Kallisto mtDNA abundances for Chagyrskaya and Estatuas sediments. kallisto abundances for all Chagyrskaya and Estatuas sediment samples with at least 250 ancient hominin DNA fragments. Abundances are normalized to the total non-modern human abundance. Reference sequences are the same as in Figure 2B, and include five sediment consensus sequences: Est_2, Est_3 and Est_4 are from Estatuas pit II/Layer 2, pit I/Layer 3, and pit I/Layer 4, respectively. Chag_6c is from Chagyrskaya Cave Layer 6c. Den_M14.3 is from Denisova Cave Main Chamber, Layer 14.3. DC1227 is Denisova 11.

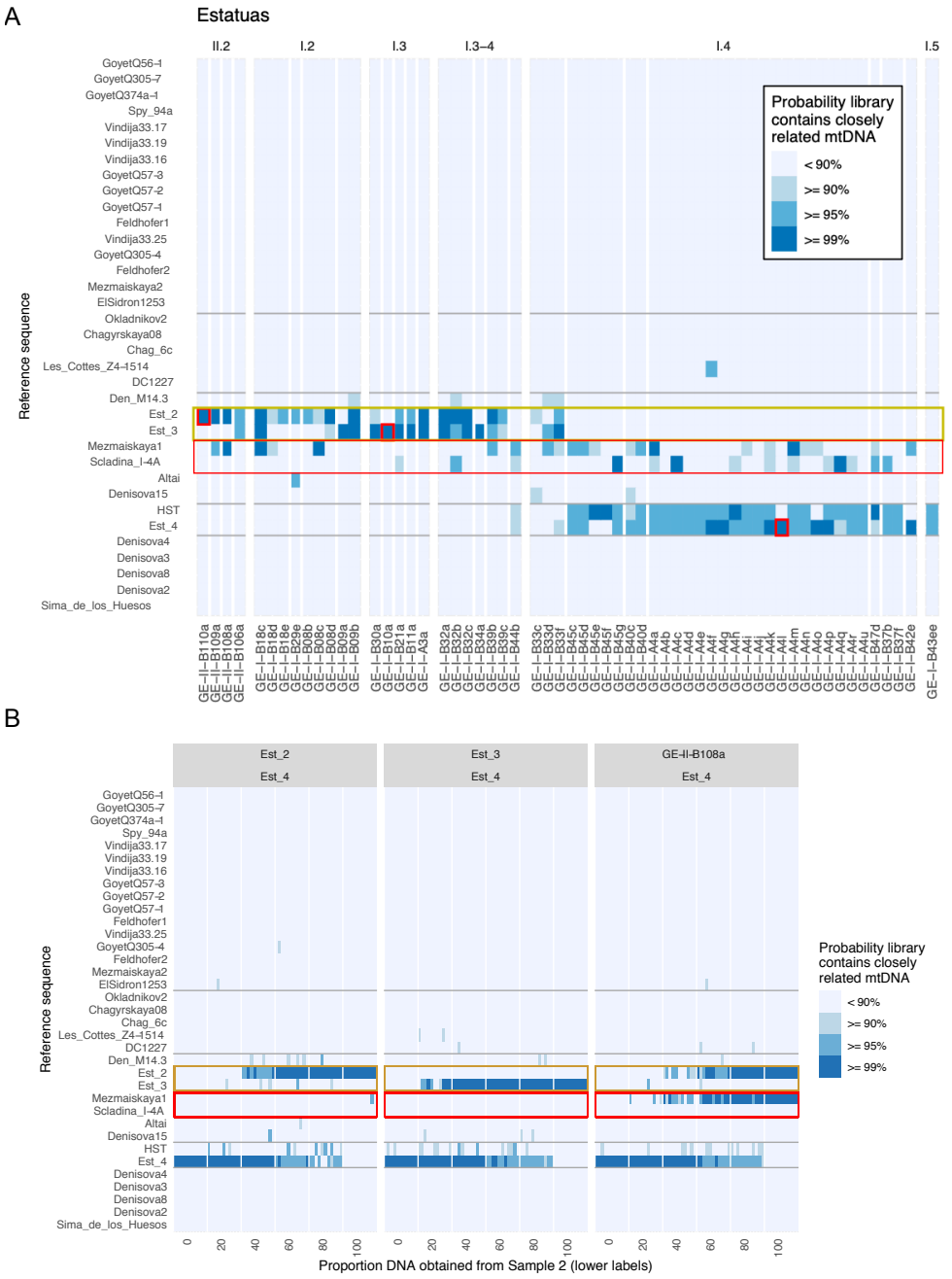

Figure S13 A) Inset from Figure 2B; yellow box highlights two mtDNA haplotypes observed primarily in the Estatuas upper layers (GE-II Layer 2 and GE-I Layers 2-3), but largely absent in the Estatuas lower layers (GE-I Layers 4-5). Large red box highlights *HST*-like mtDNA observed in Layers 4 and 5, but largely absent from upper layers. **B)** Probabilistic phylogenetic placement of mtDNA which has been artificially mixed: 1000 sequencing reads were sampled from an upper layer sample [either GE-II-B110a (library A16112; **Est_2**), GE-I-B10a (library A16045; **Est_3**)], or GE-II-B108a (library A16110), and a lower layer sample [GE-I-A4l (library A24519; **Est_4**)]. X-axis shows the proportion of DNA originating from the upper layer sample; 10 bootstraps were performed per proportion and sample pair (individual columns). Yellow and red boxes highlight the same haplotypes as highlighted in panel **A**. Rows are the same as Figure 2B and Figure S12.

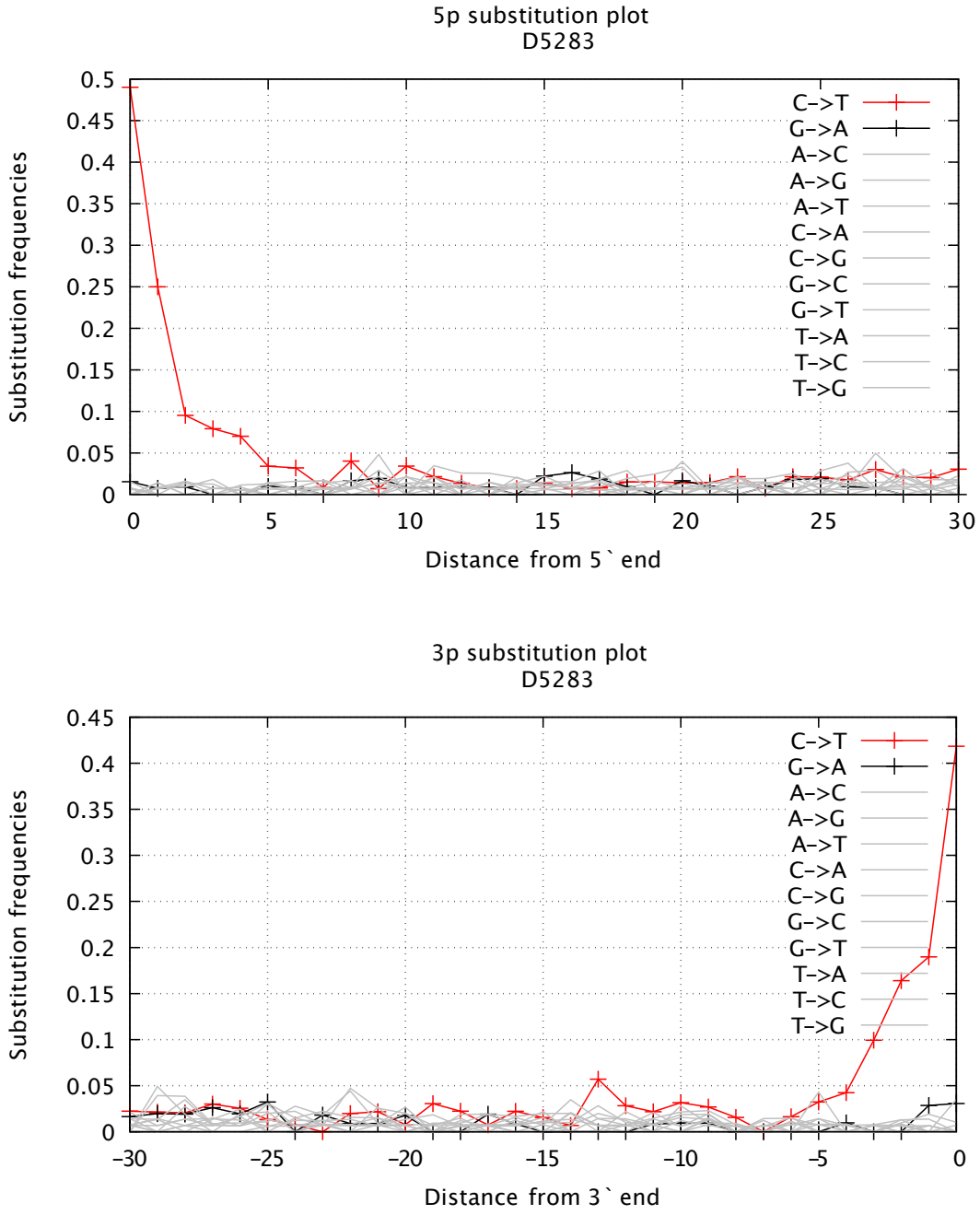

Figure S14 Deamination profiles (C-T substitutions, red line) for the kraken-filtered (Order Primate) nuclear captured library A20281, from sediment sample GE-I-A4l.

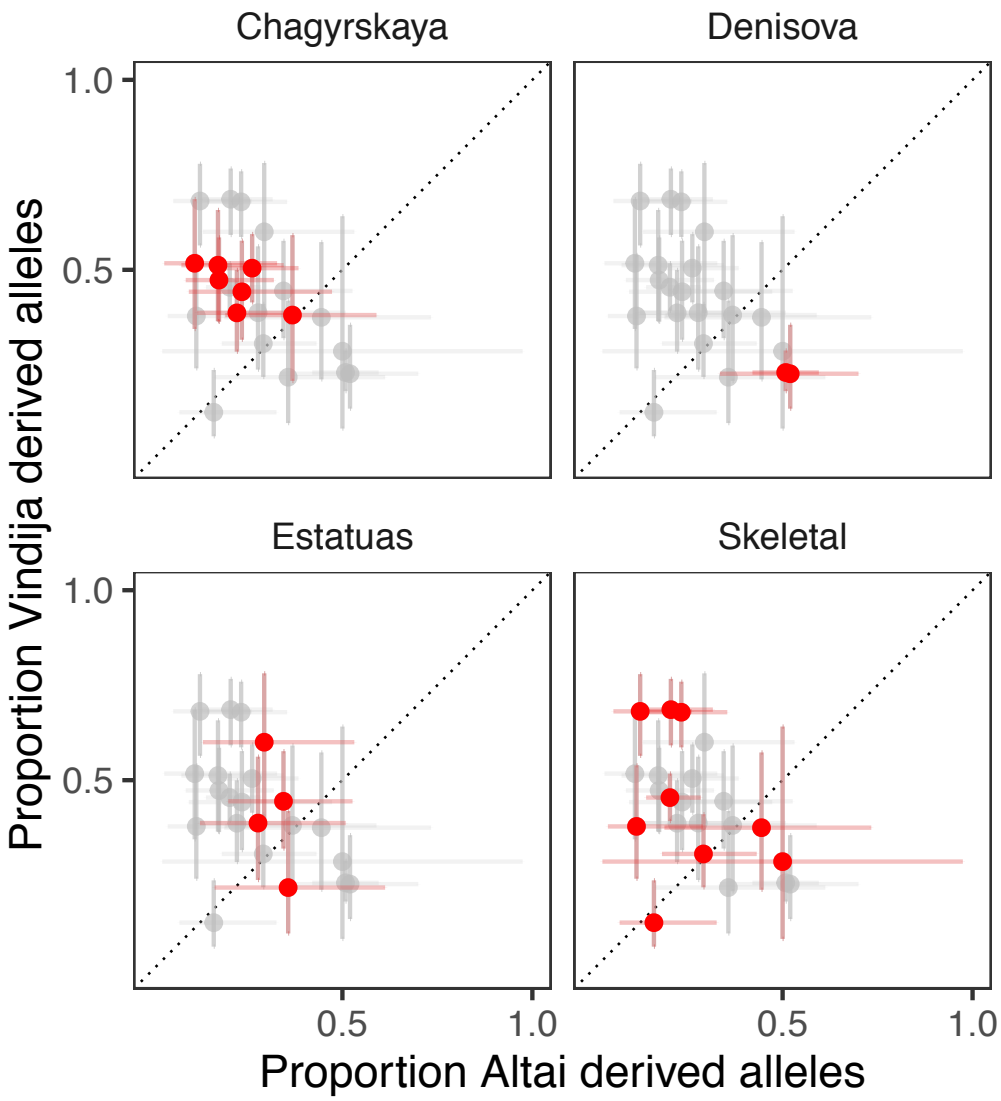

Figure S15 Derived allele proportions in sediment samples at lineage-informative sites – Altai vs Vindija. Proportion of derived alleles in deaminated DNA fragments at sites which are homozygous derived in one high-coverage individual, and homozygous ancestral in another. Plotted are sediment samples from three caves (top row, and bottom left), and previously published skeletal samples (bottom right) – all samples must have DNA fragments overlapping >= 30 informative sites. In each box, red dots are from the listed category (Chagyrskaya, Denisova, Estatuas, Skeletal). All samples are plotted in gray in the background, for context. Lines are 95% binomial confidence intervals.

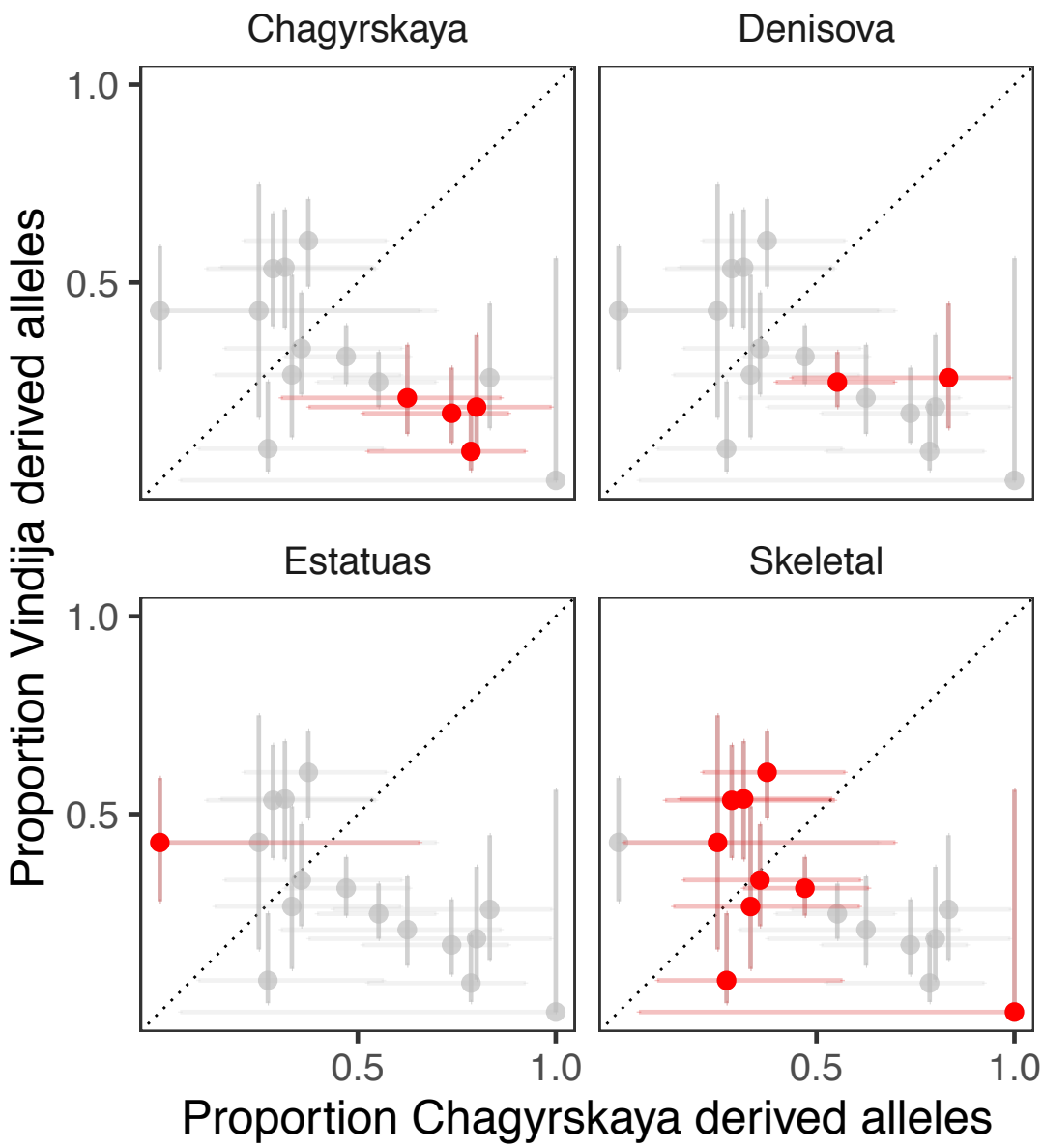

Figure S16 Derived allele proportions in sediment samples at lineage-informative sites – Vindija vs Chagyrskaya 8. Proportion of derived alleles in deaminated DNA fragments at sites which are homozygous derived in one high-coverage individual, and homozygous ancestral in another. Plotted are sediment samples from three caves (top row, and bottom left), and previously published skeletal samples (bottom right) – all samples must have DNA fragments overlapping >= 30 informative sites. In each box, red dots are from the listed category (Chagyrskaya, Denisova, Estatuas, Skeletal). All samples are plotted in gray in the background, for context. Lines are 95% binomial confidence intervals.

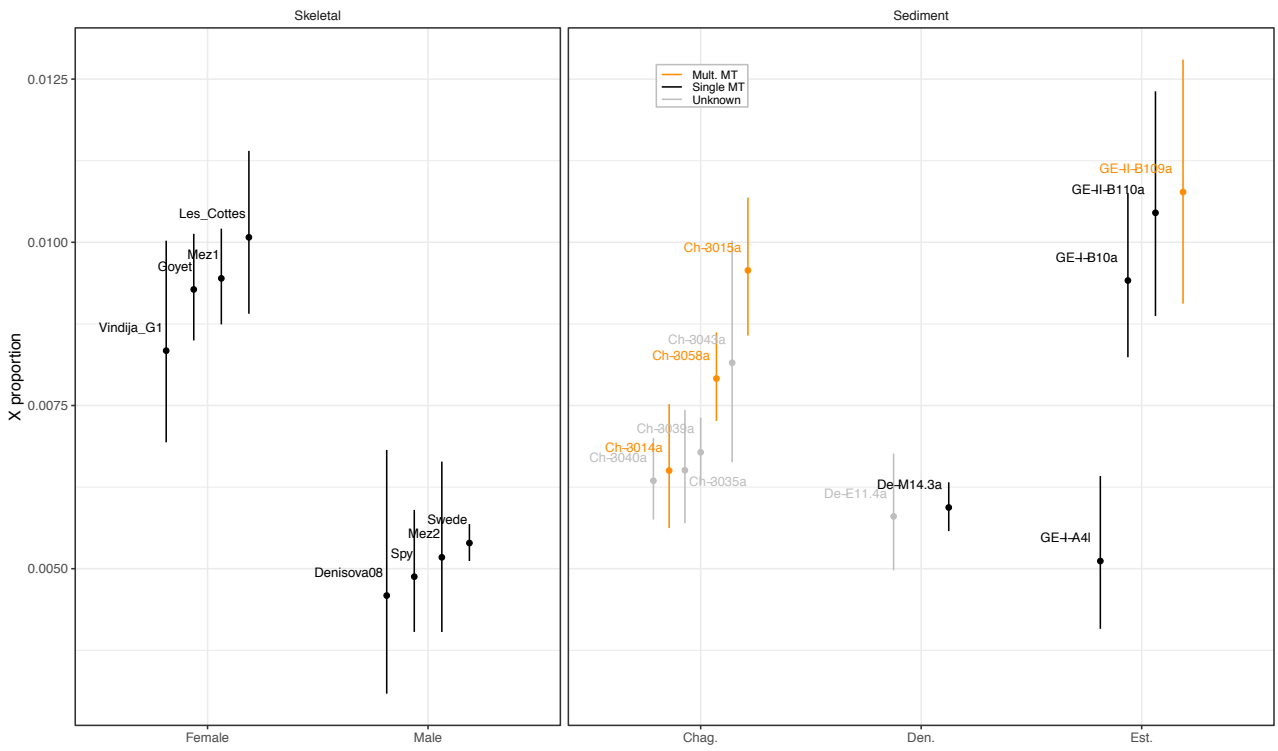

Figure S17 X-autosome proportions for skeletal and sediment samples

X-autosome proportions for skeletal and sediment samples – identical data shown in Figure 4B. CI are 95% binomial confidence intervals. Evidence of single (black) or multiple (orange) mtDNA haplotypes taken from Table S3. All samples are labeled. For consistency between sediment and skeletal samples, for sediment samples we only used data from the larger capture array (ssAA197-200), and for skeletal samples, we required a site to have been observed in at least one sediment capture.

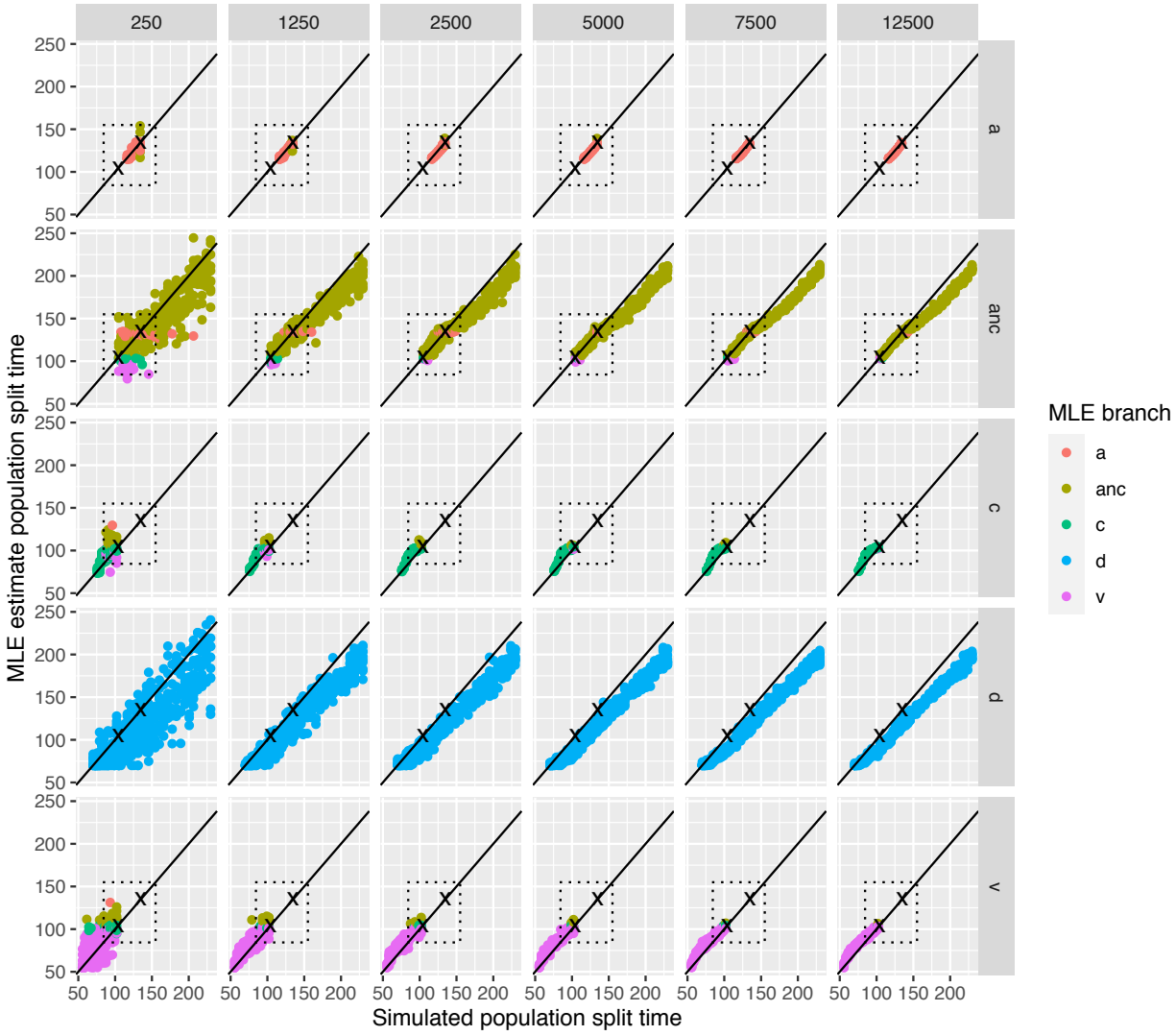

Figure S18 Accuracy of population split time estimates across population phylogeny
Estimated population split time (y-axis) vs simulated population split time (x-axis) across the archaic phylogeny, with population split times between 50 and 230kya. Simulated population split branch is denoted by rows: a, c, d, v are Altai, Chagyrskaya 8, Denisova and Vindija, respectively; anc is the ancestral branch, first of Chagyrskaya 8 and Vindija, then of all three high coverage Neandertals). Black X's denote split times of Vindija and Chagyrskaya 8 (left), and the ancestral branch and Altai (right). Dashed line box highlights +- 20ky around these split times, and is the period of interest around the estimated Estatuas split times (Fig. 5). Split times on the Denisovan branch, and on the ancestral branch older than ~140kya are under-estimated, even with large amounts of data.

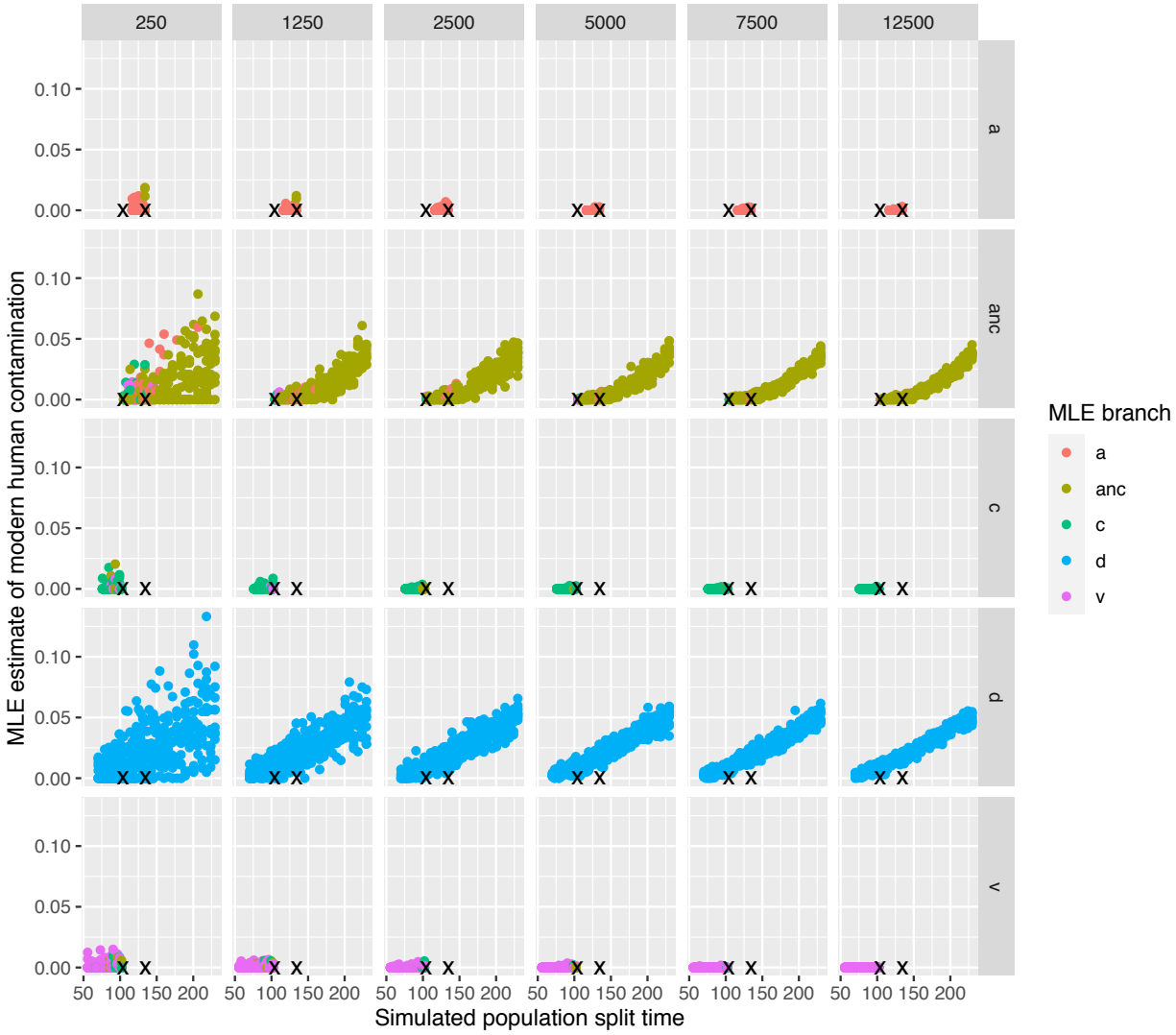

Figure S19 Over-estimated modern human contamination on Denisovan branch and for splits from the Neandertal branch older than 140kya.
MLE estimates of modern human contamination from previous figure. True modern human contamination for all simulations is 0%, but even with large amounts of data, we obtain MLE estimates of up to 5% for the oldest population split times. These time periods also generate under-estimates of the population split times, suggesting that the model may have a challenging time for older time points.

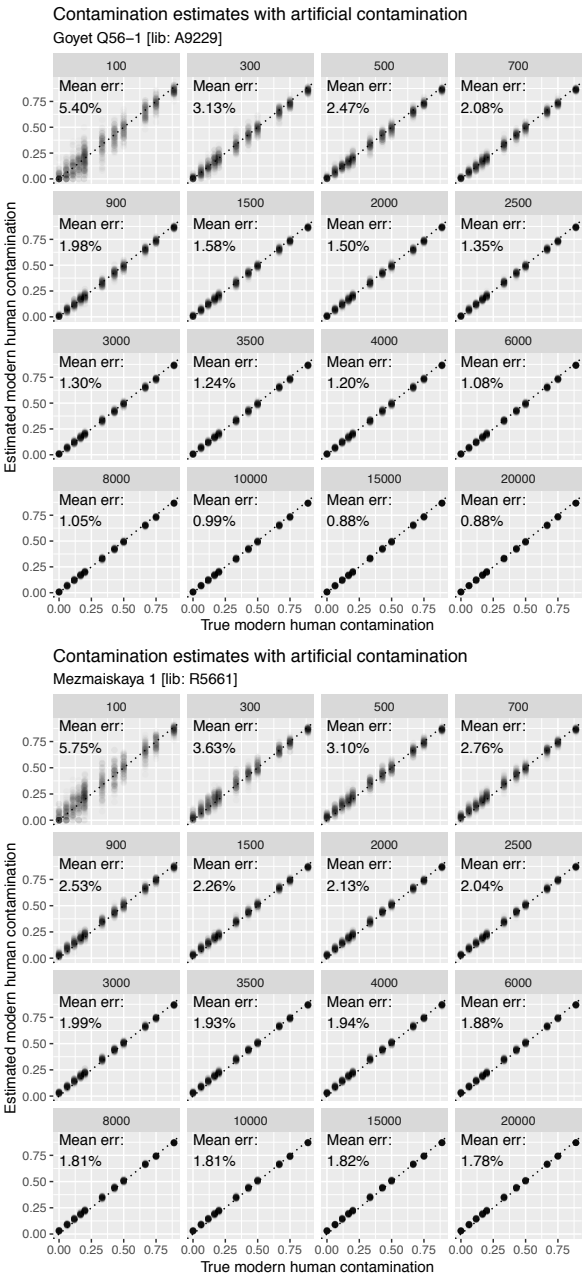

Figure S20 Modern human contamination estimates are accurate in real data
We combined real sequencing data from one of two low-coverage Neandertal genomes (Goyet Q56-1, top, or Mezmaiskaya 1, bottom), and from a modern human whose DNA was sheared to lengths comparable to aDNA fragment lengths. We did this for between 100 and 20000 Neandertal DNA fragments (facets), with additional modern human contamination such that this contamination comprised between 0% and 90% of the total dataset. We then compared true contamination levels (x-axis) with MLE estimates of contamination levels (y-axis).

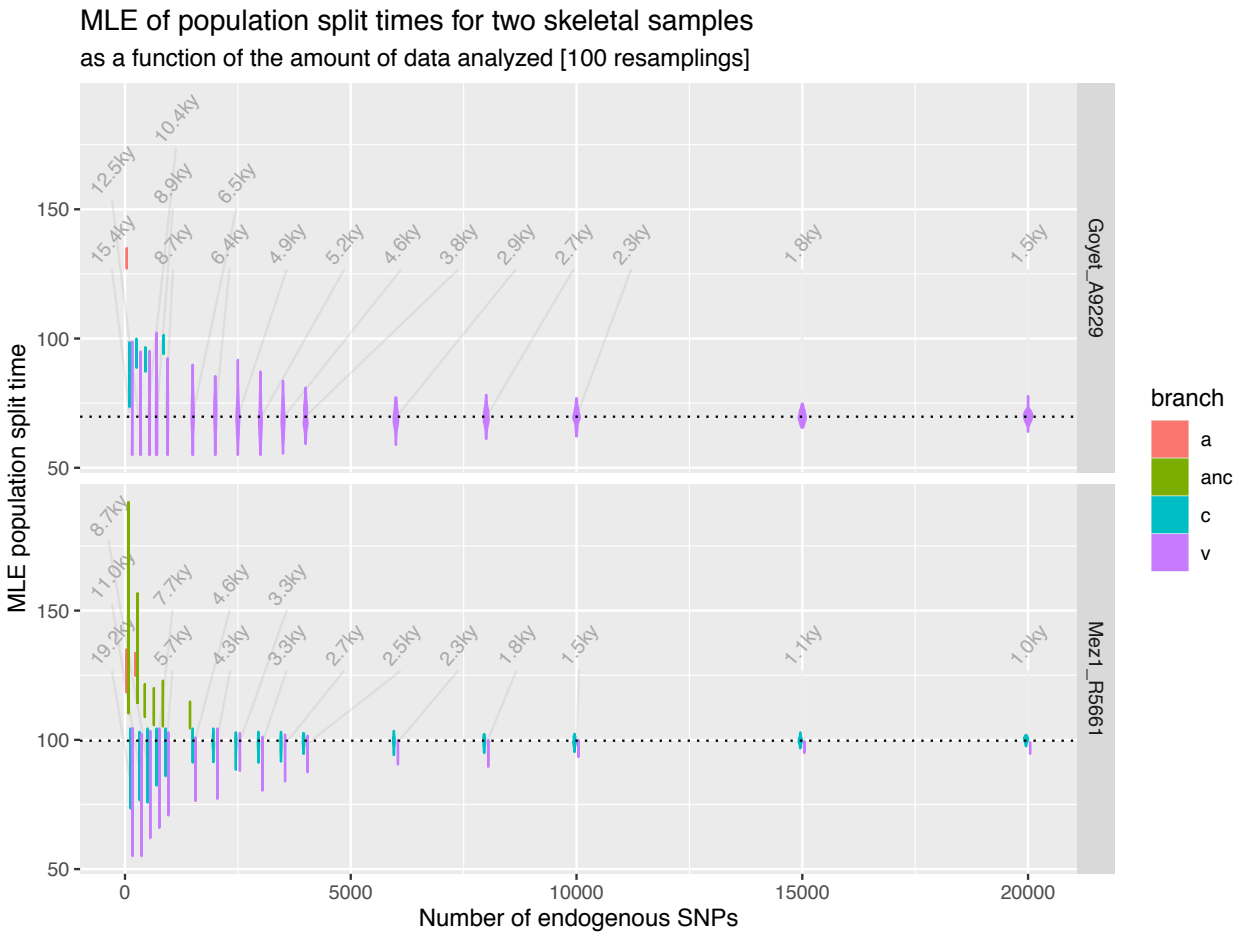

Figure S21 Population split time estimates in down-sampled data.
We performed 100 down-samplings of two libraries from published skeletal samples, Goyet Q56-1 and Mezmaiskaya 1, for 16 values of the number of endogenous SNPs. Average absolute error in population split time estimates for each SNP bin is shown in gray.

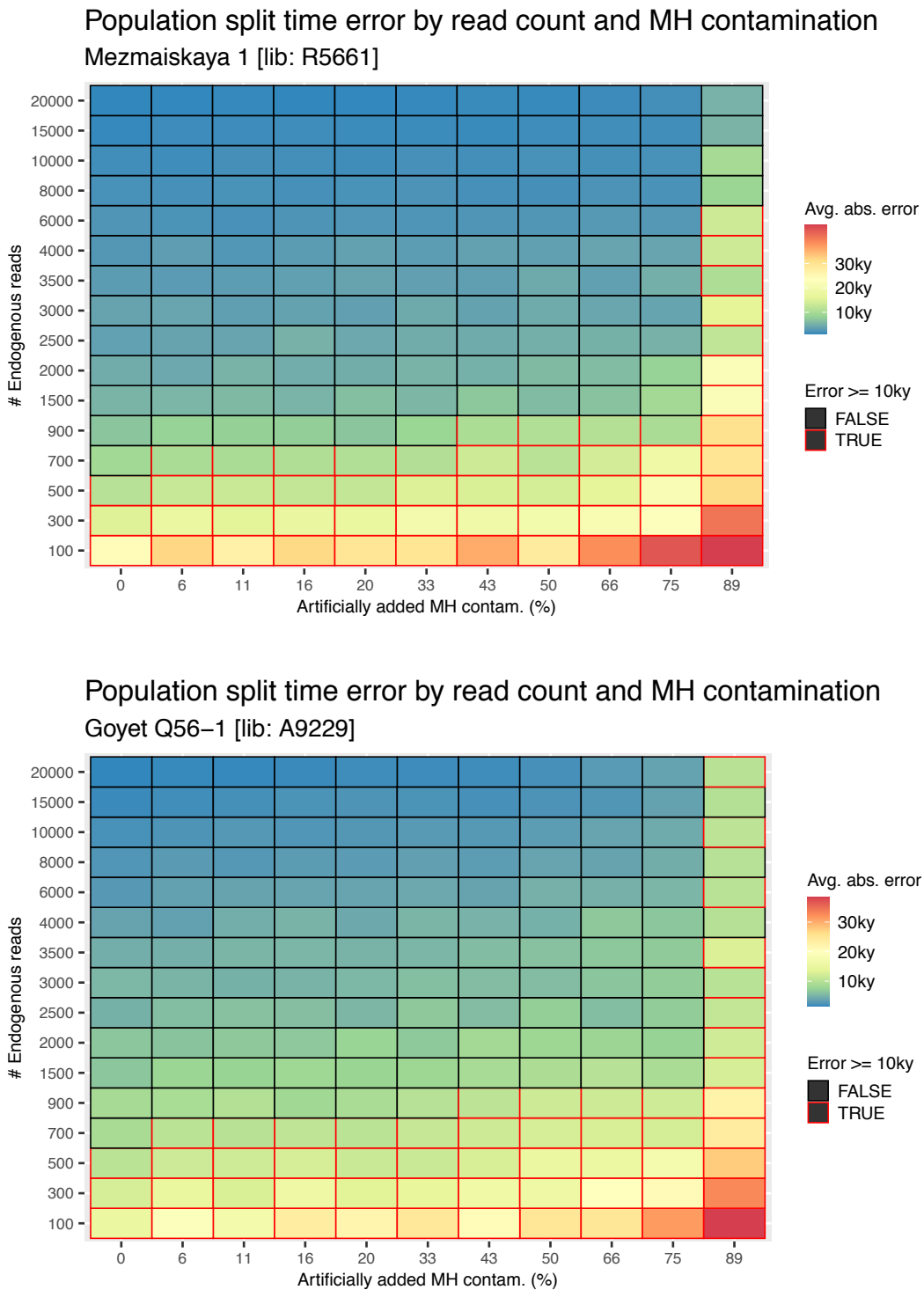

Figure S22 Population split time estimates in down-sampled data, with artificial modern human contamination

Average absolute error in MLE population split time estimates with down-sampled skeletal data and artificially added modern human contamination, for Mezmaiskaya 1 (top) and Goyet Q56-1 (bottom).

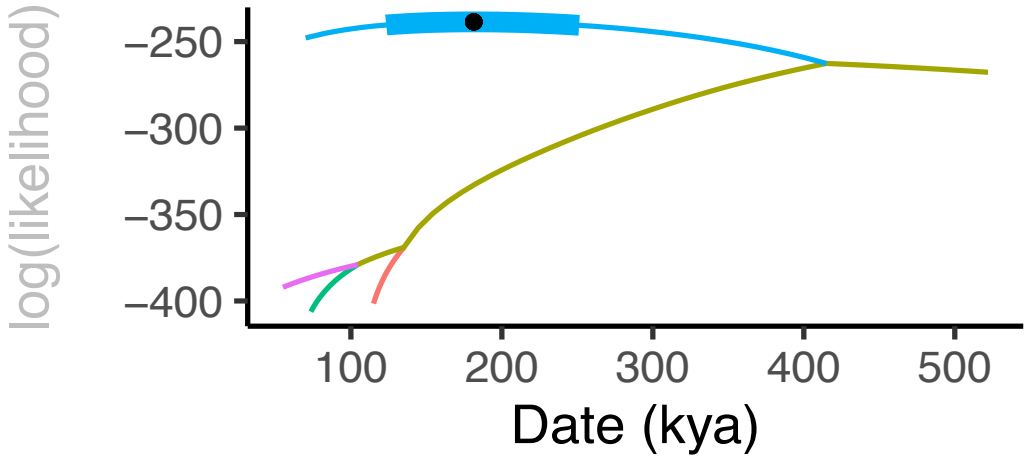

Figure S23 MLE population split time (black point) and likelihood surface for sediment sample De-E15, with Denisovan mtDNA. Thicker line shows 95% block-bootstrap confidence interval, with 100 blocks.

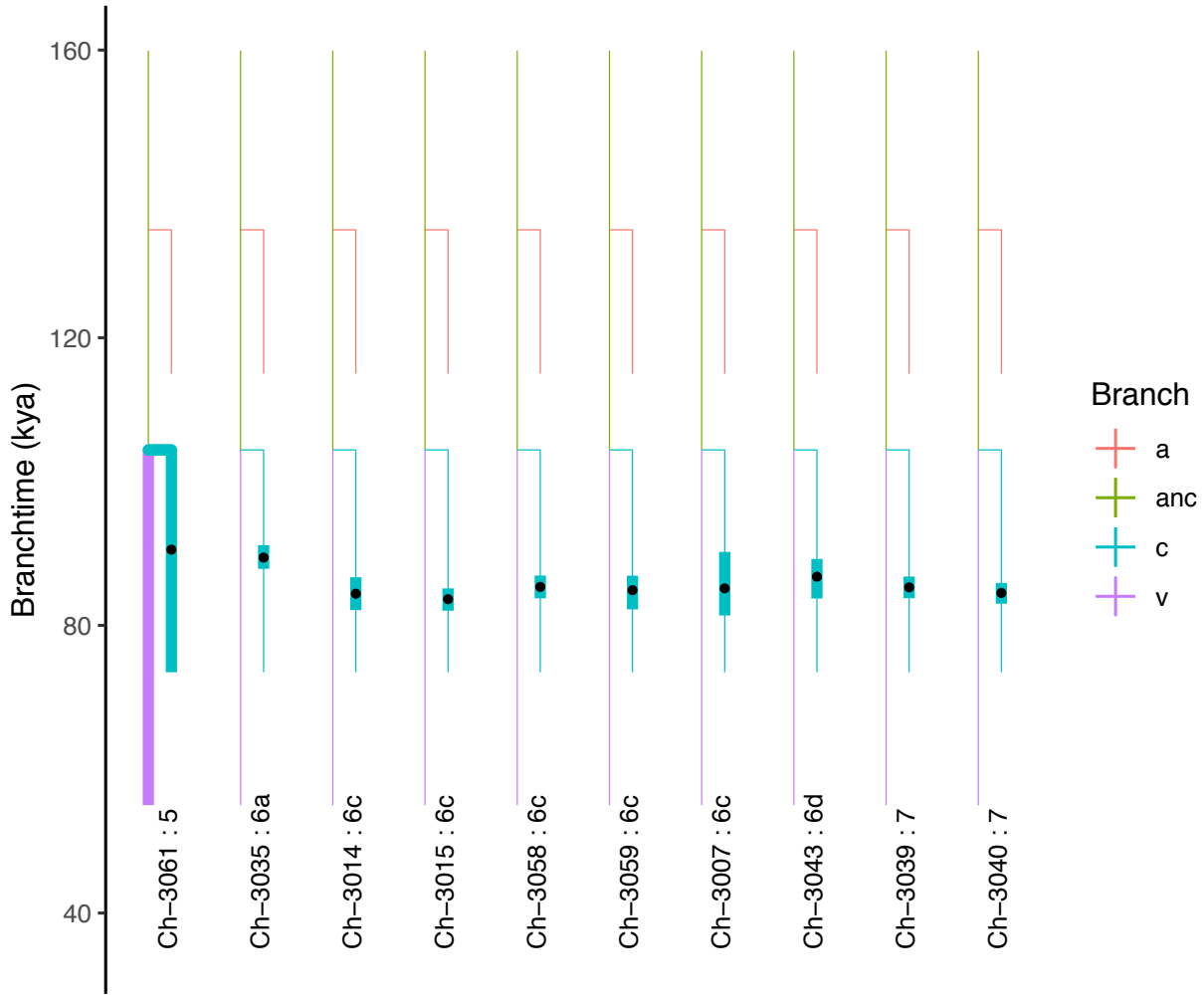

Figure S24 MLE population split times (black points) and 95% block-bootstrap confidence intervals (thick lines) for ten sediment samples from Chagyrskaya Cave.

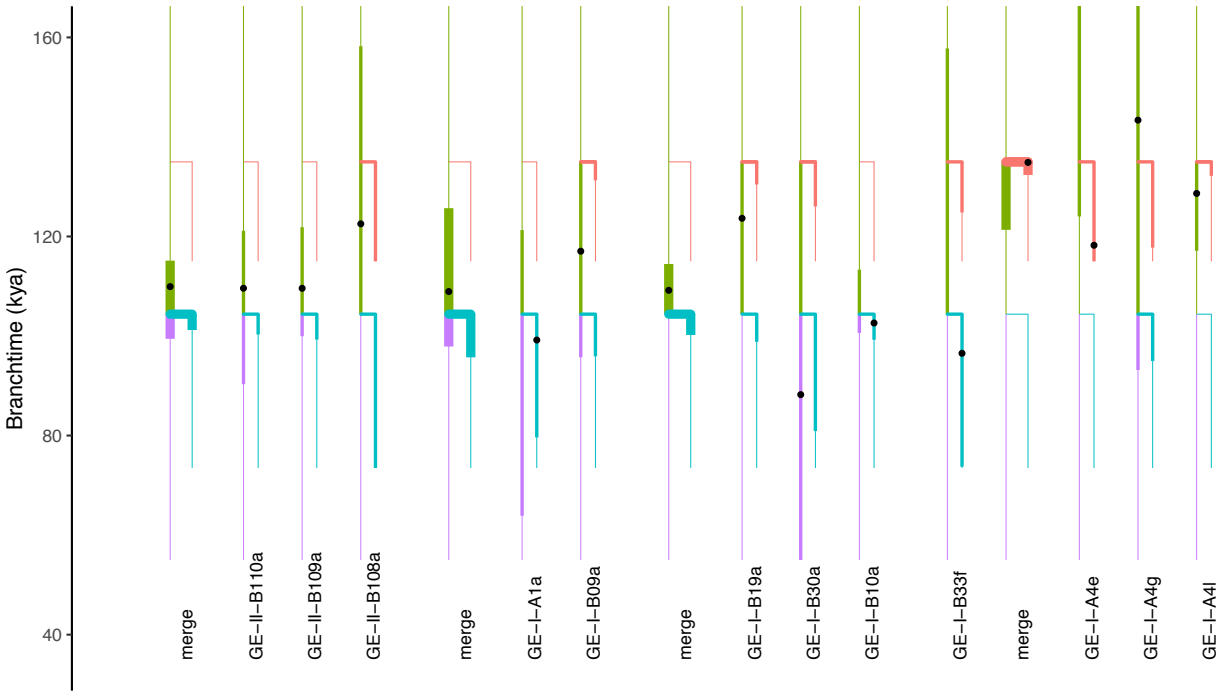

Figure S25 MLE population split times (black points) and 95% block-bootstrap confidence intervals (thick lines) using only deaminated fragments, for sediment samples presented in Figure 5A.

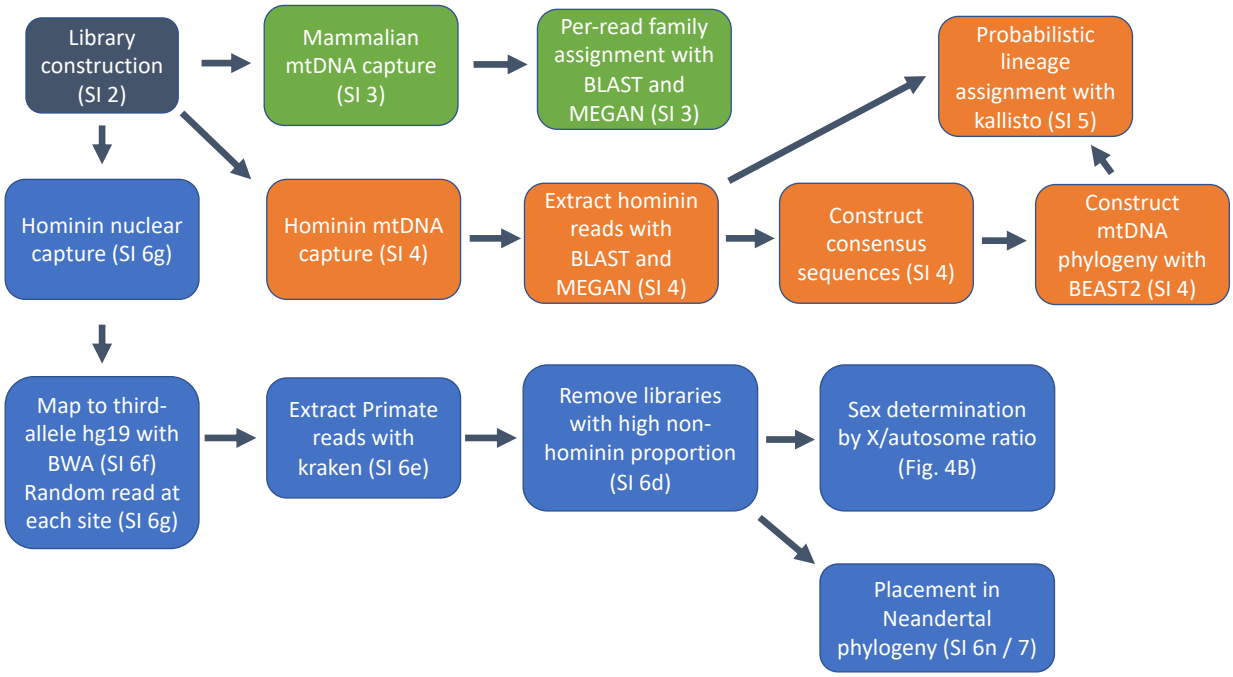

Figure S26 Analysis flow-chart for mitochondrial and nuclear DNA.

Table S1.

Chronological framework of the Galería de las Estatuas site.

Pit	Level	Method	Sample	Age (cal BP unless otherwise stated)[a]	Lab/field Label	Reference
GE-I	Capping flowstone	AMS-Ultrafiltration	Charcoal	7841-7674	OxA-25074	(*56*)
	Capping flowstone (base)	U-Th series	Speleothem	13,689 ± 387	Ilargi-f	(*56*)
	LU-1	AMS-Standard	Bone (indet)	>45,000 (uncal)	Beta-247628 (A-168)	(*11*)
	LU-1	AMS-Ultrafiltration	Long bone (indet)	52,040[b]-43,242	OxA-21523 (GE-191)	(*11*)
	LU-1	Single-grain OSL	Sediment	80,000 ± 5,000	GE16-2	(*10*)
	LU-2	AMS-Standard	Bone (indet)	>45,000 (uncal)	Beta-247626 (A-101)	(*11*)
	LU-2	AMS-Ultrafiltration	Tooth (*Equus*)	>45,600 (uncal)	OxA-21524 (GE-175)	(*11*)
	LU-2 (upper)	Single-grain OSL	Sediment	83,000 ± 5,000	GE16-1	(*10*)
	LU-2 (lower)	Single-grain OSL	Sediment	113,000 ± 8,000	GE16-3	(*10*)
	LU-3	AMS-Standard	Long bone (indet)	>45,000 (uncal)	Beta-247627 (A-129)	(*11*)
	LU-3	AMS-Ultrafiltration	Tooth (*E. hydruntinus*)	54,596[b]-43,952	OxA-21525 (GE-189)	(*11*)
	LU-3	Single-grain OSL	Sediment	107,000 ± 8,000	GE16-4	(*10*)
	LU-4	Single-grain OSL	Sediment	112,000 ± 7,000	GE16-5	(*10*)
GE-II	Capping flowstone (base)	U-Th series	Speleothem	53,774 ± 3,447	-	This study, Table S2
	LU-1b	AMS-Ultrafiltration	Long bone (indet)	54,770[b]-44,128	OxA-24563 (GE-773)	(*11*)
	LU-1	Single-grain OSL	Sediment	70,000 ± 5,000	GE16-6	(*10*)
	LU-2	AMS-Ultrafiltration	Long bone (indet)	>46,300 (uncal)	OxA-24564 (E-022)	(*11*)
	LU-2	Single-grain OSL	Sediment	79,000 ± 5,000	GE16-7	(*10*)

[a] Radiocarbon dates have been calibrated (2 σ) using Oxcal v. 4.4. software (*57*, *58*) and the Intcal120 calibration curve (*59*).

[b] Date may extend out of range

Table S2.

U/Th dating results of the base of the speleothem covering the detrital sequence of GE-II using Thermal Ionization Mass Spectrometer (TIMS) at the Xi'an Jiaotong University following the methodology from (*60*). The error is 2δ.

Sample	^{238}U (ppb)	^{232}Th (ppt)	^{230}Th/^{232}Th (atomic x 10^{-6})	δ^{234}U* (measured)	^{230}Th/^{238}U (activity)
GE-II'18 base continued	41.6 ± 0.0	7,312 ± 146	42 ± 1	80.6 ± 1.8	0.452 ± 0.004
	^{230}Th Age (yr) (uncorrected)	**^{230}Th Age (yr) (corrected)**	**^{230}Th Age (yr BP)** (uncorrected)**	**$\delta^{234}U_{Initial}$** (corrected)**	**^{230}Th Age (yr BP)*** (corrected)**
	58,616 ± 701	53,842 ± 3,447	53,842 ± 3,447	94±2	53,774 ± 3,447

U decay constants: λ_{238} = 1.55125x10^{-10} (*61*) and λ_{234} = 2.82206x10^{-6} (*60*). Th decay constant: λ_{230} = 9.1705x10^{-6} (*60*).

*δ^{234}U = ([^{234}U/^{238}U]activity – 1) x 1000.

** $\delta^{234}U_{initial}$ was calculated based on ^{230}Th age (T), i.e., $\delta^{234}U_{initial} = \delta^{234}U_{measured}$ x $e^{\lambda 234 x T}$.

Corrected ^{230}Th ages assume the initial ^{230}Th/^{232}Th atomic ratio of 4.4 ± 2.2 x10^{-6}. Those are the values for a material at secular equilibrium, with the bulk earth ^{232}Th/^{238}U value of 3.8. The errors are arbitrarily assumed to be 50%.

***BP stands for "Before Present" where the "Present" is defined as the year 1950 CE (Common Era).

Table S3:

Mitochondrial DNA consensus calls obtained from the 10 libraries with the highest number of unique hominid mtDNA fragments. Libraries that may contain mtDNA sequences from a single hominin individual are shaded in grey.

								Complete mtDNA		Protein-coding regions		
Library ID	Sub-sample (lysate) ID	Site	Placement in stratigraphy	Reference genome used for mapping	Unique hominid mtDNA fragments	Av. frag. size [bp]	Av. mtDNA coverage [fold]	Failed calls, low coverage (< 5-fold)	Failed calls, low support (≤ 75%)	Failed calls, low coverage (< 5-fold)	Failed calls, low support (≤ 75%)	Failed calls, low support, after manual editting
A16045	GE-I-B10a	Est.	Pit I, layer 3	Vindija 33.19	91,873	47.2	261.8	136	6	0	1	0
D5276[a]	De-M14.3a	Den.	Main chamb., layer 14.3	Vindija 33.19	78,611	56.4	267.7	70	1	0	0	0
A20281	GE-I-A4l	Est.	Pit I, layer 4	HST	26,216	45.0	71.2	323	5	15	1	1
A16112	GE-II-B110a	Est.	Pit II, layer 2	Vindija 33.19	20,094	49.1	59.6	362	11	19	3	1
A15858	Ch-3015a	Chag.	Layer 6c	Vindija 33.19	12,948	52.1	40.7	546	7	88	2	2
A16044	GE-I-B09a	Est.	Pit I, layer 2	Vindija 33.19	11,865	45.2	32.4	630	25	51	11	8
A15857	Ch-3014a	Chag.	Layer 6c	Vindija 33.19	11,816	52.0	37.1	703	4	173	3	3
A15919	Ch-3058a	Chag.	Layer 6c	Vindija 33.19	11,165	52.2	35.2	557	11	141	4	3
A16111	GE-II-B109a	Est.	Pit II, layer 2	Vindija 33.19	9,274	47.7	26.7	882	16	155	6	3
A16073	GE-I-B32a	Est.	Pit I, layer 3-4	Vindija 33.19	7,870	47.3	22.5	1,059	15	271	8	5
A15850	Ch-3007a	Chag.	Layer 6c	Vindija 33.19	7,682	52.0	24.1	1,382	7	477	2	1
A20287	GE-I-B09a	Est.	Pit I, layer 2	Vindija 33.19	6,568	45.2	17.9	1,351	23	378	10	5
A11423	GE-I-A4g	Est.	Pit I, layer 4	HST	6,386	45.3	17.5	1,465	53	497	27	24
A16046	GE-I-B11a	Est.	Pit I, layer 3	Vindija 33.19	6,330	45.0	17.2	1,784	32	590	12	9
A15905	Ch-3050a	Chag.	Layer 6c	Vindija 33.19	6,240	54.4	20.5	831	14	243	7	7

Est. = Galería de las Estatuas; Chag. = Chagyrskaya Cave; Den. = Denisova Cave; HST = Hohlenstein Stadl Neandertal

[a] Sequences for this library were published in (*2*)

Table S4:

The marginal log likelihoods for the mtDNA coding region generated from testing different clock and tree models with a path sampling approach.

Clock Model	Tree Model	Marginal log likelihood
Strict	Constant	-27528.2616
Strict	Bayesian Skyline	-27543.9264
Relaxed Log Normal	Constant	-27524.8209
Relaxed Log Normal	Bayesian Skyline	-27540.0119

Table S5:

Tip dates and divergence times (in years) reported from the Tracer program from BEAST2 using a strict clock and constant population size for the protein coding region.

Specimen	Mean	95% HPD lower	95% HPD upper	ESS
Denisova2	193,710	122,560	264,630	964
Denisova3	73,714	41,596	99,999	781
Denisova4	79,872	38,404	112,980	578
Denisova8	154,360	78,488	228,580	1,133
A16045 (Estatuas, pit 1 layer 3)	106,840	59,765	154,260	1,251
A16112 (Estatuas, pit 2 layer 2)	107,770	60,455	154,600	1,270
A20281 (Estatuas, pit 1 layer 4)	136,150	75,095	199,590	784
D5276 (Denisova Cave, Main chamber layer 14.3)	127,560	85,136	171,380	1,141
A15850 (Chagyrskaya, layer 6c)	90,097	54,986	126,590	629
Altai Neandertal	140,680	94,450	190,080	1,023
Chagyrskaya08	85,294	49,627	122,190	659
Denisova11	114,790	84,607	146,390	802
Denisova15	135,680	87,158	185,120	1,047
El Sidron	66,593	41,387	93,015	532
Goyet Q305-7	40,372	30,335	46,830	242
Goyet Q374a-1	40,342	30,178	46,686	268
HST	135,550	72,083	197,500	809
Mezmaiskaya 1	97,127	50,174	144,650	1,528
Okladnikov2	109,480	76,708	142,650	1,122
Scladina	125,380	74,762	176,670	1,107
Vindija 33.17	53,799	38,135	67,120	311
Vindija 33.19	45,231	32,353	55,984	268
Vindija 33.25	45,660	31,107	59,104	271
Sima de los Huesos	347,600	219,120	474,750	529
TMRCA Denisovans + Sima	673,450	580,570	768,500	782
TMRCA Humans	177,260	146,650	211,210	24,240
TMRCA Neandertals	317,030	266,080	366,510	1,318

Table S6.

Probability of observing a derived allele in a sediment sample which diverges from the Vindija lineage 73.5kya and 104.4kya (top and bottom rows), given that the site is heterozygous in Vindija and ancestral in the other three archaic individuals (0 = homozygous ancestral, 1 = heterozygous, 2 = homozygous derived).

Vind. 33.19	Chag. 8	Altai	Denisovan	Branch	Branch-time	Number of SNPs	p(sed = 1)
1	0	0	0	Vindija	73.5kya	7854549	0.19812952
1	0	0	0	Vindija	104.4kya	7852841	0.11649236

Table S7.

Previously published population split estimates from seven Neandertal individuals, using two methods, along with a summary of our MLE results. Full MLE results in Table S9.

Sample	F(A|Vindija 33.19)	Coal. split (A-V split = 137ky)	MLE Pop. split time (A-V split = 135ky)
Mezmaiskaya 2	70.0 [67.4-74.5]	81.3 [79.8-82.8]	78.37 [69.03-86.26]
Les Cottés Z4-1514	70.0 [67.9-72.4]	76.8 [75.6-78.1]	78.16 [74.00-82.88]
Goyet Q56-1	59.9 [57.8-61.9]	55.3 [52.9-57.8]	69.04 [64.94-72.60]
Spy 94a	62.7 [59.1-64.8]	62.2 [59.4-64.8]	72.86 [67.57-78.26]
Mezmaiskaya 1	98.7 [94.5-102.9]	97.2 [95.6-98.8]	99.88 [97.45-101.29]
	F(A|Vindija 33.19)	**Coal. split (A-V split = 130ky)**	**MLE Pop. split time (A-V split = 135ky)**
HST	101.1 [80.2-122.7]	123.7 [119.3-127.8]	127.99 [120.86-133.70]
Scladina I- 4A	100 [66.4-152.7]	123.3 [114.2-130.0+]	134.83 [114.74-155.88]

Table S8.

Previously published modern human contamination estimates.

Sample	Previously published modern human contamination estimates	Publication - Method
Mezmaiskaya 2	0-1.1%	Hajdinjak 2018 (*25*) – qpAdm
Les Cottés Z4-1514	0-1.1%	Hajdinjak 2018 (*25*) – qpAdm
Goyet Q56-1	0-1.1%	Hajdinjak 2018 (*25*) – qpAdm
Spy 94a	3.9-4.2%	Hajdinjak 2018 (*25*) – qpAdm
Mezmaiskaya 1	2.9-3.2%	Hajdinjak 2018 (*25*) – qpAdm
HST	22.1- 23.8%	Peyrégne 2019 (*19*) – human derived alleles
Scladina I- 4A	63.0-66.7%	Peyrégne 2019 (*19*) – human derived alleles

Table S9.

Population split estimates from seven Neandertal individuals, using MLE method (details in Table S14).

Sample	Target sites	MLE Pop. split time (A-V split = 135ky)	Branches	Modern Human Contam.	Dataset
Mezmaiskaya 2	primary sediment array	78.37 [69.03-86.26]	V	0.6%	downsampled; 10636 SNPs
Les Cottés Z4-1514	primary sediment array	78.16 [74.00-82.88]	V	0.8%	downsampled; 25591 SNPs
Goyet Q56-1	primary sediment array	69.04 [64.94-72.60]	V	0.7%	downsampled; 52409 SNPs
Spy 94a	primary sediment array	72.86 [67.57-78.26]	V	4.2%	downsampled; 21807 SNPs
Mezmaiskaya 1	primary sediment array	99.88 [97.45-101.29]	V, C	3.0%	downsampled; 65454 SNPs
Mezmaiskaya 1	unrestricted	100.35 [97.19-101.17]	V, C	3.0%	downsampled; 162680 SNPs
HST	primary sediment array	127.99 [120.86-133.70]	V-C ancestor, A	36.8%	full
Scladina I- 4A	primary sediment array	134.83 [114.74-155.88]	V-C ancestor, A, V-C-A ancestor	78.6%	full

Table S10

Detailed information on each sample collected, and all libraries constructed from those samples, along with negative controls. For each library we include a summary of the analysis of human mtDNA, including support for various hominin groups based on diagnostic positions, as described in SI 4. Significant support for a particular group (binomial 95% confidence interval >10%) is indicated with ^. Excel spreadsheet, available online.

Table S11

Faunal mtDNA summary for an initial screening of nine sediment samples from Galería de las Estatuas, along with five negative controls. Excel spreadsheet, available online.

Table S12

Summary of nuclear captures for sediment libraries and negative controls. In addition, shotgun data for several previously published skeletal samples, processed in the same manner as the sediment samples. Some libraries were captured multiple times, or on different probesets. Merged data given in Table S13. Columns described in SI 6g. Excel spreadsheet, available online.

Table S13

Merged summary of nuclear captures from Table S12. Columns described in SI 6g. Excel spreadsheet, available online.

Table S14

Summary of branch-time analysis for sediment and skeletal samples. Details given in SI 6n. Excel spreadsheet, available online.